Charge Mixing Model and Robust Tracking Control for Mechatronic Engines

A DISSERTATION
SUBMITTED TO THE FACULTY OF THE GRADUATE SCHOOL
OF THE UNIVERSITY OF MINNESOTA
BY

Yongsoon Yoon

IN PARTIAL FULFILLMENT OF THE REQUIREMENTS
FOR THE DEGREE OF
Doctor of Philosophy

Prof. Zongxuan Sun

Oct, 2015

Acknowledgements

Thanks to all.

Dedication

To my beloved wife, Hwa Jung Cha and daughter, Susie Yoon.

Abstract

The growing demand for sustainable technology in the automotive industry has led to vibrant research on mechatronic engines. The mechatronic engine replaces and integrates existing mechanical devices with advanced electronics to increase flexibility of engine control. The flexible engine control is to achieve optimal performance in regards to exhaust emissions and fuel efficiency. This thesis, in particular, concerns modeling, analysis, and tracking control of an electrohydraulic camless engine valve actuator for flexible gas flow control. The thesis consists of three main chapters.

In the first chapter, a control-oriented charge mixing model is developed to analyze the effect of variable valve actuation on mixing of fresh charge and residual gas, referred to as *charge mixing*. The complex charge mixing is simplified by the enthalpy transfer between two control volumes: the mixed and unmixed zones. Then, thermodynamic interaction between two zones depending on variable valve actuation is modeled. The model is validated through engine simulations and optical engine tests. Further simulation studies are conducted to investigate the effect of different valve actuation strategies.

In the second chapter, nonlinear frequency domain models of an electrohydraulic actuator are developed for spectral analysis and system identification. Both analytic and experimental approaches are presented. The analytic frequency domain model is derived from physical dynamics using Volterra series representation of a nonlinear system. Spectral analysis with the analytic model helps to uncover the critical nonlinear features of the electrohydraulic actuator in frequency domain. The experimental frequency domain model is identified from frequency response. With the assumption of the block-oriented model structures, the models are parametrized and the associated parameters are estimated based on spectral analysis.

In the third chapter, internal model principle-based robust tracking control of an electrohydraulic actuator is presented to achieve nonstationary valve motion of a camless engine. As in many reciprocating machines, reference valve motion of an internal combustion engine is defined as a periodic signal in rotational angle domain of the

engine. However, the reference valve motion is aperiodic in time domain, because rotational speed of the engine varies with time. Such motion is referred to as *nonstationary motion* whose frequency contents vary with time. Regarding a nonstationary reference signal modeled by a time varying exosystem, the high-order time varying internal model is proposed and its effectiveness is demonstrated by implementation on the prototype electrohydraulic camless engine valve actuator.

Contents

List of Tables

List of Figures

Chapter 1

Introduction

This thesis focuses on a charge mixing model and robust tracking control for mechatronic internal combustion engines. Over the past several decades, advanced electronics such as sensors, actuators, microcomputers, and controls has significantly contributed to the great progress of mechatronic internal combustion engines. They are expected to satisfy increasingly stringent regulations on fuel economy and exhaust emissions for motor vehicles. However, mass production of the mechatronic internal combustion engines is impeded by fundamental challenges in modeling, analysis, and controls. In this thesis, these challenges are addressed to realize the benefits of mechatronic internal combustion engines.

1.1 Technical Motivation

This section reviews high standards of fuel economy and exhaust emissions for passenger vehicles motivating the development of advanced internal combustion engines. Mechatronic engines and the main interest of this thesis, an electrohydraulic camless engine valve actuation system, are briefly introduced as an alternative of existing conventional internal combustion engines.

1.1.1 High Standards for Motor Vehicles

As shown in Fig. 1.1, the transportation sector is the second largest source, more than one third, of the U.S. carbon dioxide emissions in 2013. Specifically, the motor vehicles

including the light, medium, and heavy duty vehicles are the major sources and they are responsible for over 80 percent of the transportation sector carbon dioxide emissions. Consequently, automotive manufacturers and suppliers are consistently demanded to produce motor vehicles which consume less fuel and produce less exhaust emissions under the slogan "Sustainable Technologies".

The U.S. federal government has regulated fuel economy and exhaust emissions for decades. Fig. 1.2 (a) shows the corporate average fuel economy (CAFE) standards of light duty vehicles and trucks from 1978 to 2025. As can be seen, the standard has been getting increasingly more stringent since 1978. And since 2010, the standard has increased much faster than ever. Fig. 1.2 (b) shows Tier 3 emission standards with the federal test procedure (FTP) finalized in 2014 for combination of nonmethane organic gas (NMOG) and nitrogen oxide (NOx). The standard in 2016 indicates Tier 2 emission standard. Until 2025, considerable reduction of NMOG and NOx should be achieved as 0.03 g/mi.

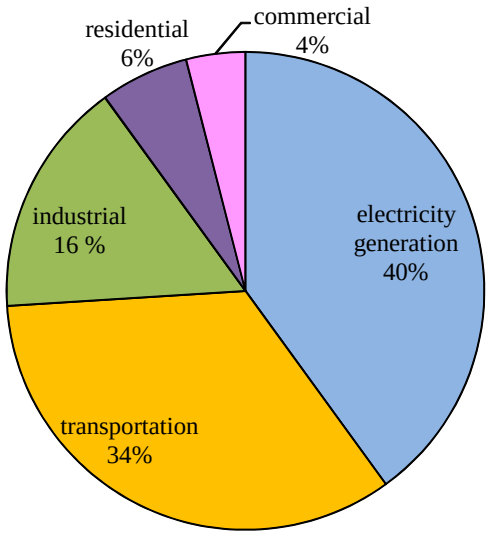

(a)

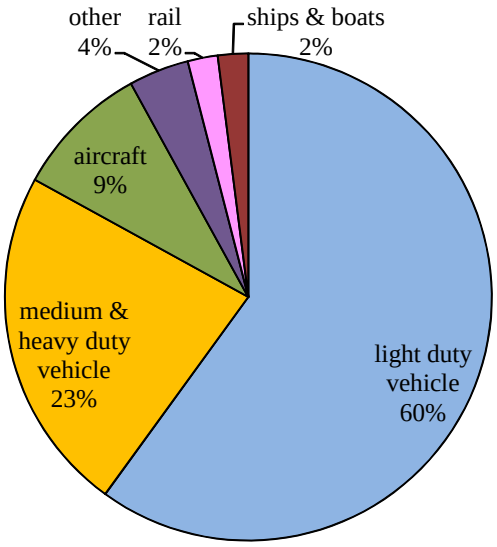

(b)

Figure 1.1: 2013 U.S. CO_2 emissions (a) by sector and (b) by source [1]: one third of 2013 U.S. CO_2 emissions is from the transportation sector, and over 80 % of 2013 U.S. transportation sector CO_2 emissions is from passenger vehicles.

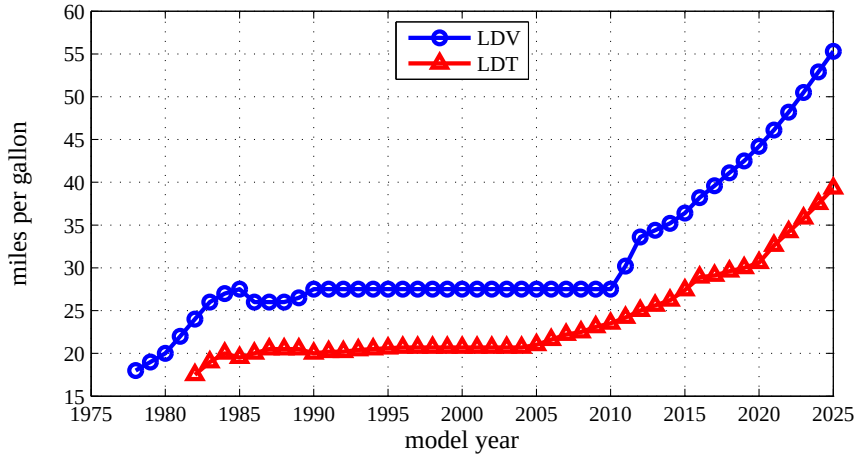

(a)

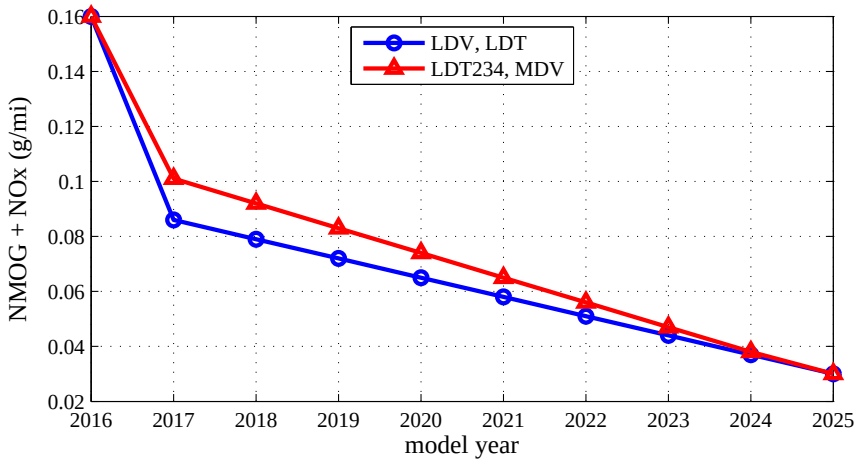

(b)

Figure 1.2: U.S. standards of fuel economy and exhaust emissions for passenger vehicles: (a) fuel economy standard from MY1978-2025 [2, 3], (b) Tier 3 fleet average NMOG + NOx emission standards [4].

1.1.2 Mechatronic Engines

Vibrant research on mechatronic engines is motivated by meeting stringent regulations on fuel economy and exhaust emissions. By replacing and integrating existing mechanical devices with advanced electronics, the mechatronic engine offers high flexibility of engine controls, thereby optimality, efficiency, and functionality of internal

combustion engines can be achieved [5, 6, 7]. Components of the mechatronic engine can be categorized into two main parts with respect to controlled variables: 1) fuel management systems, 2) air management systems.

Fuel Management Systems

Since replacing carburetors during 1980s, the electronic fuel injector (EFI) has played a central role for fuel delivery to an internal combustion engine. It uses high pressure to atomize the fuel through a small nozzle. In the early stage, closed-loop fuel injection control is developed by using an oxygen sensor which measures oxygen concentration of exhaust gas [8]. Recently, more advanced fuel injection systems are developed to improve fuel economy and emissions performance such as direct injection (DI), injection rate shaping control, and common rail direct injection (CRDI) [9, 10, 11].

Air Management Systems

Air management systems control air flow rate into an intake manifold or a combustion chamber. A conventional throttle valve mechanically linked to an accelerator pedal is replaced by an electronic throttle control (ETC) system for active flow control into an intake manifold [12]. It enables consistent and smooth combustion even under severe transient cases. In addition, it facilitates the integration of advanced functionality such as cruise control, traction control, and stability control [13, 14].

A variable valve actuation system enables active flow control into a combustion chamber [15]. This system, which employs independent valve actuators, enables fully flexible air management. Such a variable valve actuation system facilitates advanced control functions such as throttleless load control, and internal exhaust gas recirculation [16, 17]. An internal combustion engine with such capability is referred to as *a camless engine*. Depending on power source, variable valve actuation systems can be categorized into three: electromechanical, electrohydraulic, and electropneumatic valve actuators [18, 19, 20]. Fig. 1.3 (a)-(c) depict schematics of the conventional cam valve actuator, the electromechanical valve actuator, and the electrohydraulic valve actuator, respectively. A cam-based valve actuation system uses an eccentric cam to produce smooth reciprocating valve motion. Electromechanical and electrohydraulic valve actuation systems use magnetic and hydraulic forces to actuate engine valves.

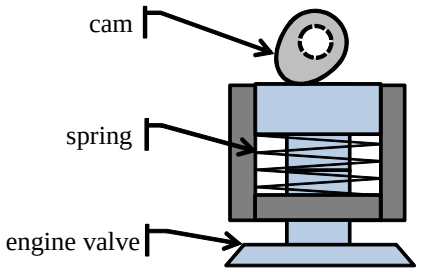

(a)

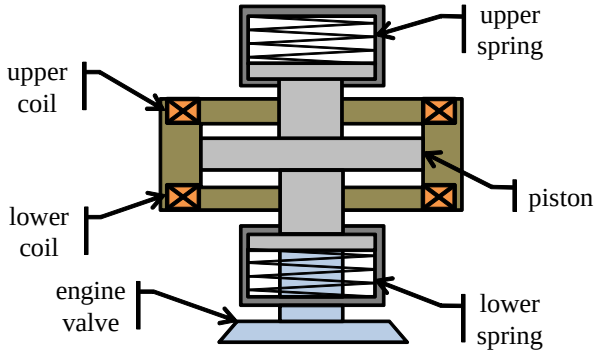

(b)

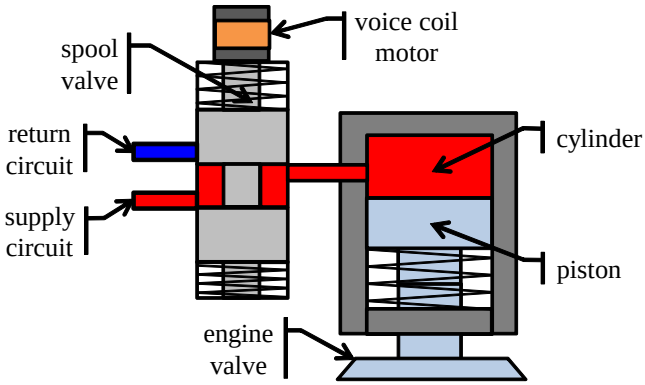

(c)

Figure 1.3: Valve actuation systems: (a) cam valve actuator, (b) electromechanical valva actuator, (c) electrohydraulic valve actuator.

1.1.3 Electrohydraulic Camless Engine Valve Actuator

Particularly, this thesis focuses on modeling, analysis, and tracking control for an electrohydraulic camless engine valve actuator. Electrohydraulic actuators have been employed in a wide range of industrial applications thanks to their great advantages such as high power density, large force capacity, and fast response over other power transmission methods. However, inherent nonlinear dynamic features have complicated its practical use as a precise actuator. Therefore, the electrohydraulic actuators have been actively studied for decades. This thesis consists of three chapters to address the technical challenges associated with the electrohydraulic camless engine valve actuator: 1) charge mixing model, 2) frequency domain model, 3) robust tracking control.

1.2 Challenges and Objective

This section presents technical challenges of an electrohydraulic camless engine valve actuator to emphasize significance of the thesis, then research objective will follow.

1.2.1 Charge Mixing Model

Control-oriented Charge Mixing Model

Fig. 1.4 describes charge mixing process during an intake stroke. Actual charge mixing is chaotic due to turbulence. Previous experimental research revealed that insufficient mixing may cause considerable variation of exhaust gas temperature and composition. Charge mixing turns out to strongly depend on variable valve actuation. Therefore, charge mixing should be taken into account for planing variable valve actuation. Without knowledge of how valve actuation affects charge mixing, reference valve motion can only be searched experimentally at huge expense.

Measurement equipment to observe charge mixing occurring in a cylinder is limited because of high pressure and temperature. Instead, simulations using computational fluid dynamics (CFD) software have been conducted to study charge mixing, especially for homogeneous charge compression ignition engines with fully flexible valve actuation [21, 22, 23, 24]. Unfortunately, CFD models are not suitable for the use of real time control, since solving CFD suffers from extremely heavy computational cost.

This thesis aims at developing a control-oriented charge mixing model with variable valve actuation through simplification of charge mixing process, while capturing its critical physics. Computational cost should be low enough for real time application, but the model must have an acceptable level of agreement with actual process.

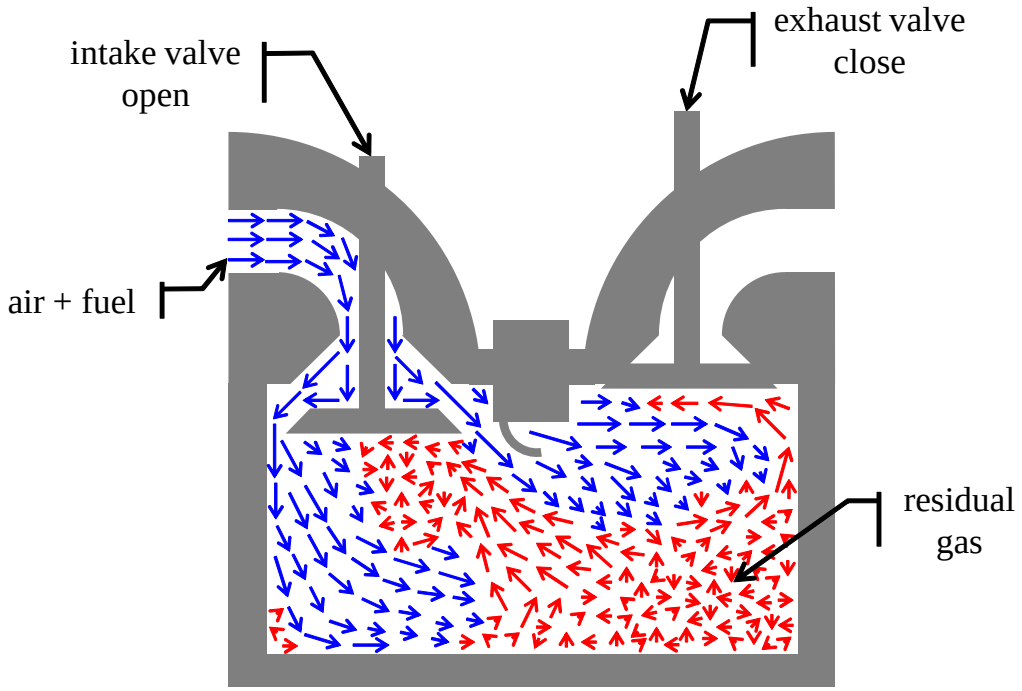

Figure 1.4: Description of charge mixing during an intake stroke: fresh charge (blue), residual gas (red), and a longer arrow means a faster flow.

Analysis for IR images of Optical Engine

In this thesis, an infrared (IR) optical engine shown in Fig. 1.5 is used to to validate the developed charge mixing model. Fig. 1.6 shows the actual IR images taken at the different rotational angles. An IR optical engine has both intrinsic and extrinsic challenges for validation of the charge mixing model.

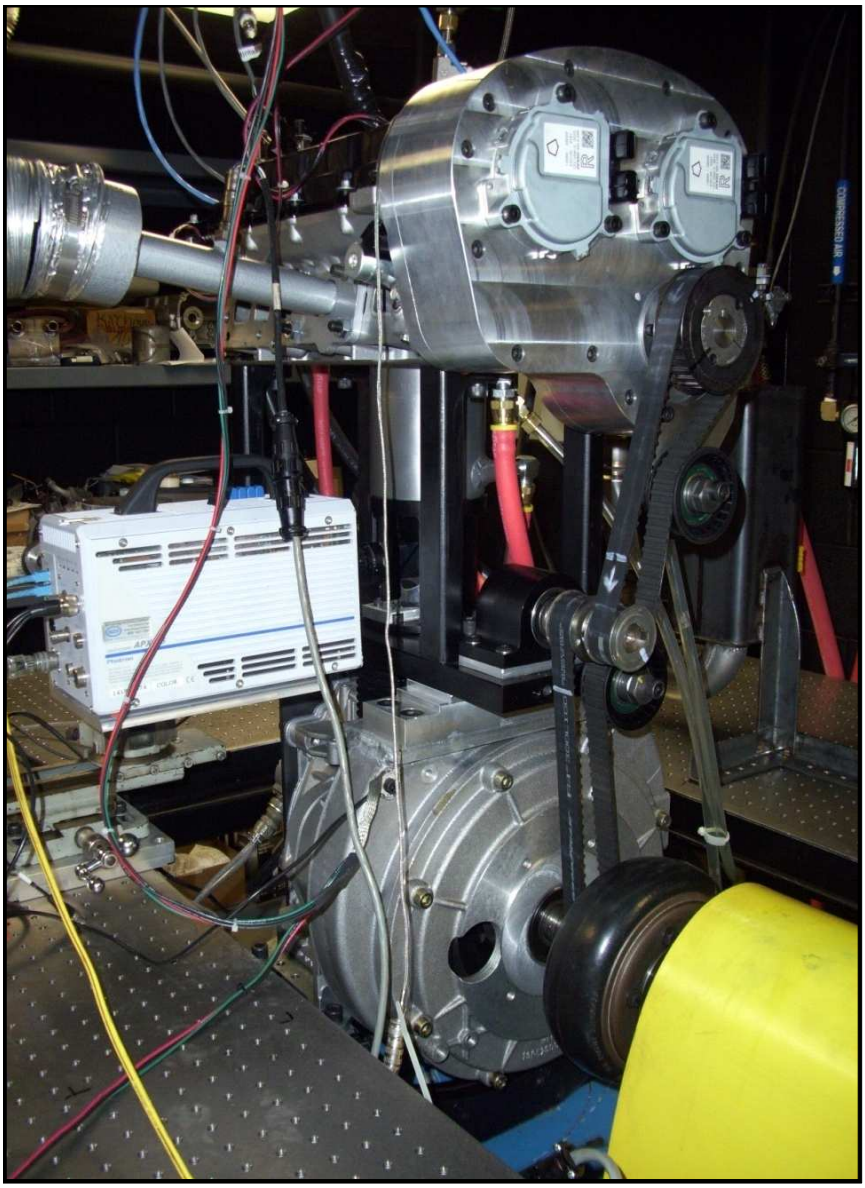

Figure 1.5: Experimental setting of the optical engine.

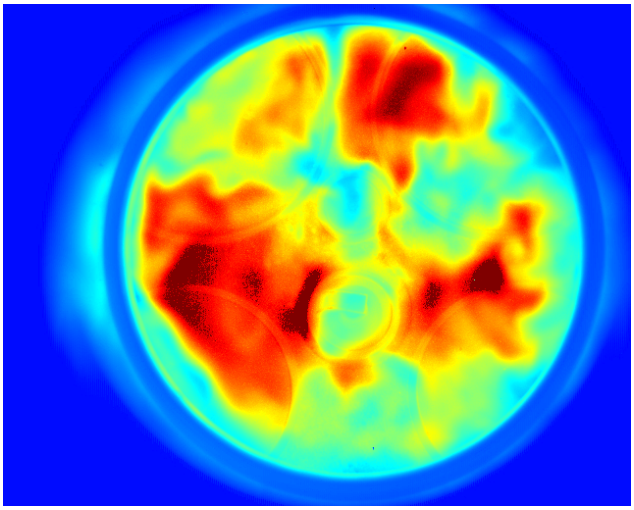

(a)

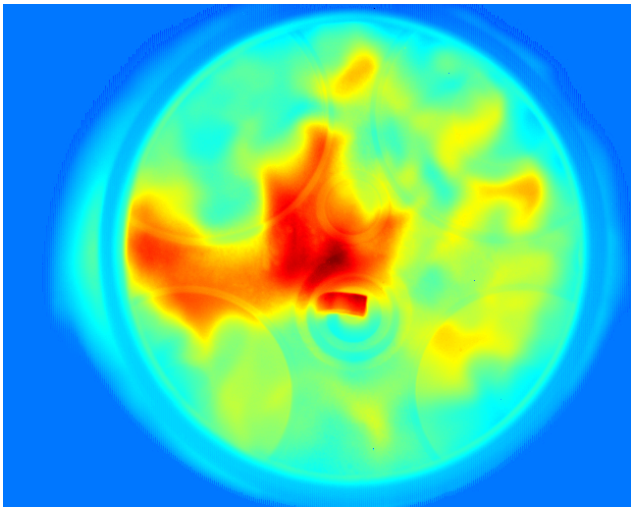

(b)

Figure 1.6: Infrared images of an optical engine taken at (a) 30 (deg) and (b) 50 (deg) after top dead center (TDC) in crank angle degree. The circle indicates the optical window.

Pixels of an IR image have intensity meaning digitized radiation energy of gas. Radiation energy is proportional to the fourth power of surface temperature, and to emissivity of an object [25]. If emissivity of an object is very low, radiation energy will be low. Unfortunately, emissivity of gas associated with combustion is very low except for soot [26]. An IR image includes inevitable anisotropic noises interrupting image interpretation. And if tiny portion of residual gas is contained by fresh charge, which means being mixed, it appears as a small isolated region. Thus, an appropriate image filter should be used to filter out undesired noises and to remove any isolated pixels, while minimizing distortion of structural information of charge mixing, for example a boundary where cold fresh charge meets hot residual gas [27].

Optical engines have been used for ignition diagnosis of a compression ignition (CI) engine and a spark ignition (SI) engine [28, 29]. Ignition happens in a similar place, for example, compression ignition around a direct injector, and spark ignition around a spark plug. On the other hand, charge mixing is very chaotic. Charge mixing occurs throughout the combustion chamber volume. However, the optical window (a circle in Fig. 1.6) is approximately an half of the engine bore (i.e. radius of a combustion chamber). It means that only a quarter of the chamber volume can be observed. Therefore, model validation is limited to a qualitative approach. The proposed charge mixing model uses two zones according to a mixing level of fresh charge with residual gas. Therefore, an IR image should be segmented into two zones for model validation. However, due to chaos, it is challenging to divide an image.

Qualitative graphical analysis will be pursued for charge mixing model validation. Soot with high emissivity will be used for graphical analysis to interpret IR images, and a proper filter will be designed for image post-process. Then, an image segmentation technique will be applied to extract qualitative thermodynamic properties of two zones. Then, validity of the charge mixing model will be shown through comparison between the model and IR images.

1.2.2 Frequency Domain Model

Spectral Analysis of Electrohydraulic Actuators

This thesis concerns the camless engine valve actuation system using an electrohydraulic actuator shown in Fig. 1.7. Due to the ease of linear analysis, the linear models of electrohydraulic actuators were developed. A beauty of the linear model lies in spectral analysis using frequency response functions (i.e. linear transfer function in frequency domain). However, since an electrohydraulic actuator includes nonlinear dynamics, the linear model cannot capture all the critical features.

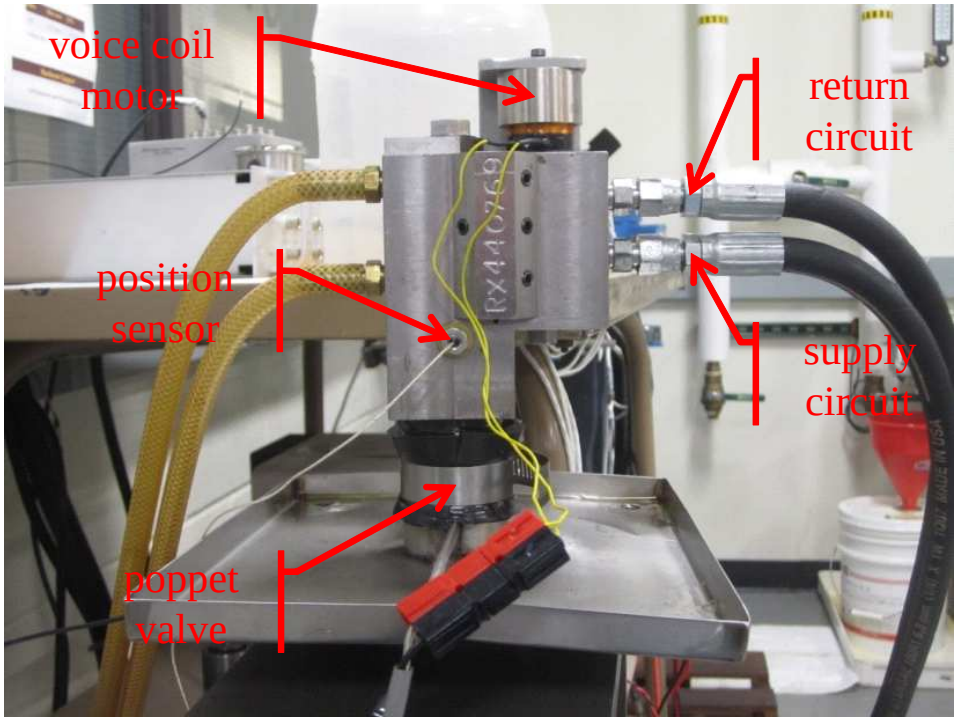

Figure 1.7: Prototype of an electrohydraulic camless engine valve actuator.

As a quasi-linearization method, describing functions are employed. However, it cannot retain nonlinear dynamic features in frequency domain, such as intermodulation, and harmonics as observed in Fig. 1.8 [30, 31]. It shows the output time traces and Fourier transforms when inputs of different frequencies are applied. As can be seen, the output possesses more frequency contents than those of input, which means the input

energy is transferred to other frequency contents.

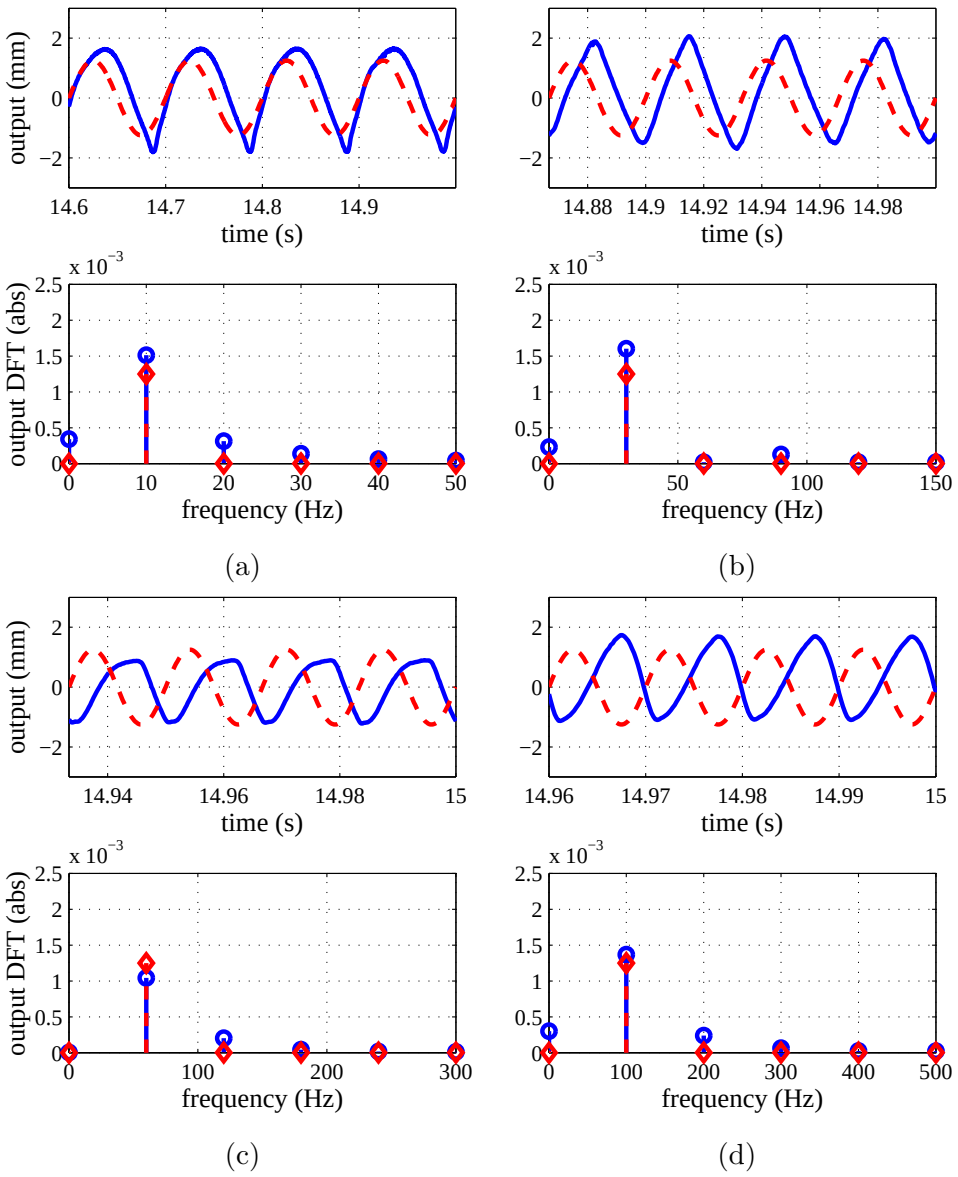

Figure 1.8: Nonlinear dynamic features of the electrohydraulic actuator in frequency domain: the sinusoidal input signal of (a) 10 Hz, (b) 30 Hz, (c) 60 Hz, (d) 100 Hz frequency. output time trace (upper), and output discrete Fourier transform (lower). Output has more frequency contents than that of input.

The nonlinear models were developed to retain the essential nonlinear factors such as the orifice flow through a spool valve and the friction force, such as stiction and Coulomb friction. These nonlinearities were taken into account for modeling, parameter estimation, and nonlinear control design [32, 33, 34, 35]. In general, such an accurate nonlinear model is expensive, and if its uncertainties are critical, the control performance is affected adversely. And a critical drawback of a nonlinear system is the absence of universal analysis tool.

This chapter aims at developing a frequency domain model of an electrohydraulic actuator for the purpose of spectral analysis. The model is explicitly derived from physical dynamics of the electrohydraulic actuator using Volterra series representation. It will help to uncover the frequency domain nonlinear features shown in Fig. 1.8. The ultimate objective of spectral analysis using a frequency domain model is to extend the fruitfulness of spectral analysis such as system identification and control design of a linear system to a nonlinear electrohydraulic actuator.

Nonlinear System Identification

Frequently, physical systems without prior information or little may be encountered in many engineering applications. In this case, an experimental frequency domain model can be developed to retain critical features found from frequency response. Nonlinear system identification in frequency domain was studied in [36, 37, 38], but they are time-consuming and require a lot of test results with different input amplitudes.

Motivated by the previous studies, an efficient technique for nonlinear system identification in frequency domain will be proposed to develop an experimental nonlinear frequency domain model of an electrohydraulic actuator. The technique should be numerically stable and robust.

1.2.3 Robust Tracking Control

Nonlinear Dynamic Behaviors of Valve Actuators

A precise physical model is expensive in general. Frequently, it is not available due to the limited access for measurements. For the camless engine valve actuator, the number of available sensors is limited due to the small space. Thus, it is hard to estimate the

physical model parameters precisely. In this case, an experimental model is preferred to a physical one. Robust tracking control design with a nonlinear experimental model is harder than a linear case [39], since a nonlinear model possesses more complicated dynamic features than a linear model.

In this thesis, frequency domain interpretation of internal model principle is adopted for robust tracking control of a nonlinear system. Through frequency domain analysis of a nonlinear feedback system, robust tracking control is investigated in terms of internal model principle.

Nonstationary Engine Valve Motion

For many reciprocating machines, events and corresponding control actions are defined in position domain. For an internal combustion engine, the events are associated with four strokes: intake, compression, expansion, exhaust as shown in Fig. 1.9. Corresponding control actions are defined in crank angle domain such as Fig. 1.10. Therefore, although reference valve motion is periodic in crank angle domain, it becomes aperiodic in time domain, because engine position changes with engine speed. Such motion is referred to as *nonstationary motion* of which frequency contents vary with time. Fig. 1.11 illustrates such a case with a linearly increasing engine speed. Tracking such a nonstationary signal is challenging, but it is applicable to a range of reciprocating machines.

This chapter is motivated by two control schemes: the high-order time invariant internal model for robust stationary tracking control of a nonlinear system [40, 41]; the time varying internal model for robust nonstationary tracking control of a linear system [42, 43, 44, 45]. By combining two control schemes, the high-order time varying internal model will be designed for robust nonstationary tracking control of a nonlinear system based on internal model principle.

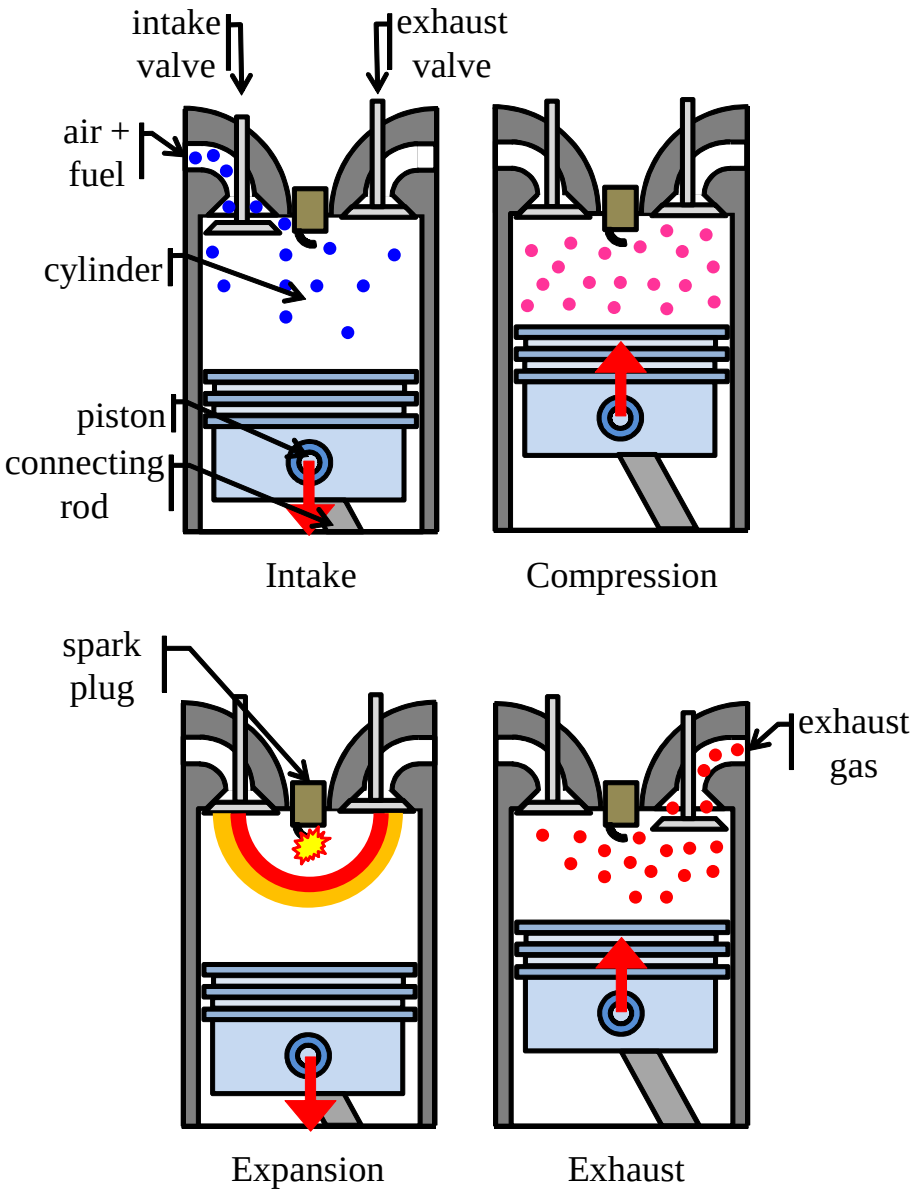

Figure 1.9: Four strokes of a spark ignition (SI) internal combustion engine: 1)intake - fresh charge inflows, 2)compression - prepare combustion, 3)expansion - combustion, 4)exhaust - exhaust gas expels.

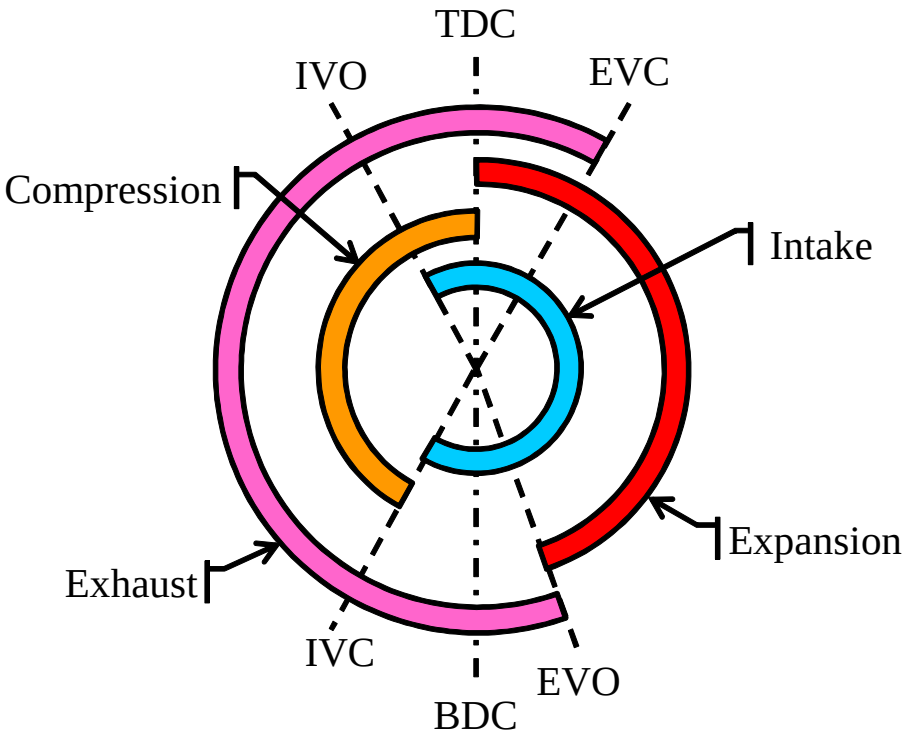

Figure 1.10: Valve timing diagram in rotational angle domain: intake valve open (IVO), intake valve close (IVC), exhaust vavel open (EVO), exhaust valve close (EVC), top dead center (TDC), and bottom dead center (BDC).

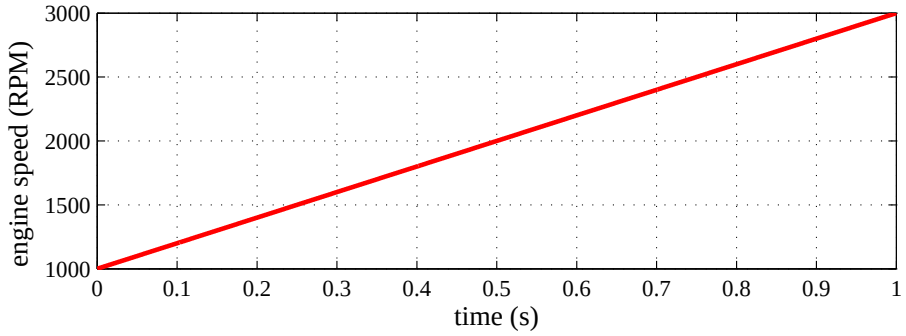

(a)

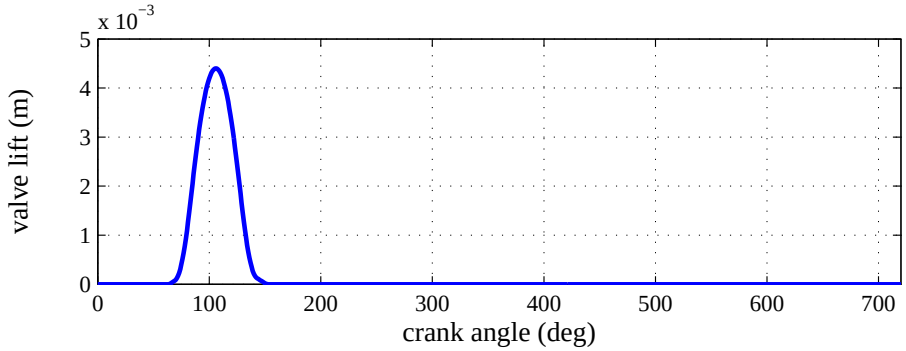

(b)

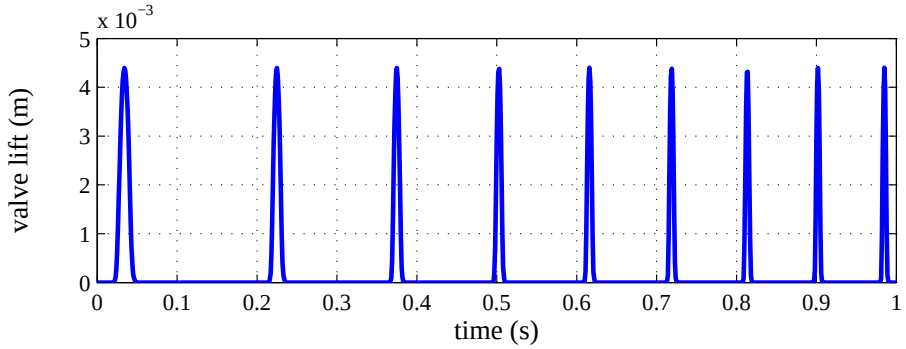

(c)

Figure 1.11: Nonstationary valve motion depending engine speed: (a) linearly increasing engine speed, and the corresponding valve lift (b) during a cycle, (c) during a time.

1.3 Research Overview

This section presents research overview by chapter. Main tasks conducted in each chapter are briefly introduced. Then, connection between chapters will follow.

1.3.1 Control-oriented Two-zone Charge Mixing Model

Model Development

The physical model is developed with the two-zone definition to represent the charge mixing process between fresh charge and residual gas depending on variable valve actuation for the purpose of active engine valve control.

Model Validation

The model is validated through the reliable engine simulator and the optical engine. The infrared images taken from the optical engine are segmented into two zones, and analyzed to estimate their thermodynamic properties. Through comparison with these estimates, the developed model is validated.

Simulation Study

Comparative simulation studies are carried out with different valve actuation schemes: 1) intake valve timing shift, 2) exhaust valve timing shift, 3) asynchronous intake valve timing, to study their effects on the charge mixing.

1.3.2 Frequency Domain Model of An Electrohydraulic Actuator

Analytic Frequency Domain Model

The analytic frequency domain model is derived from the physical dynamics of the electrohydraulic actuator. Then, spectral analysis is conducted to analyze the nonlinear dynamic features of the electrohydraulic actuator in frequency domain.

Experimental Frequency Domain Model

Without prior information of the actuator, the experimental model is estimated from frequency response. For a model structure, the block-oriented nonlinear systems are considered including the Wiener and Hammerstein models. Based on spectral analysis, the model parameters are estimated by applying the (iterative) linear least squares methods.

1.3.3 Robust Tracking Control of An Electrohydraulic Valve Actuator

Stationary Reference Tracking

First, based on frequency domain analysis of a nonlinear feedback system, the stationary reference tracking control is designed in terms of internal model principle for a nonlinear actuator. To achieve robust tracking performance, the high-order time invariant internal model is designed, and the effectiveness is demonstrated.

Nonstationary Reference Tracking

Motivated by the stationary case, the high-order time varying internal model is designed based on time-frequency analysis to achieve nonstationary reference tracking control for a nonlinear actuator. Similarly, its effectiveness in robust tracking performance is illustrated.

1.3.4 Connection between Chapters

The control-oriented charge mixing model developed in the first chapter enables model-based reference motion planning so that the desired charge mixing can be achieved through the electrohydraulic camless engine valve actuator. The second chapter focuses on system identification and analysis in frequency domain for the electrohydraulic actuator. The identified frequency domain model and frequency domain analysis reveal its critical dynamic features. Finally, the robust tracking control is designed based on frequency domain analysis of a nonlinear feedback system to follow the reference motion. Implementation of the electrohydraulic camless engine valve actuator needs successful reference planning, modeling, analysis, and robust tracking control of the actuator

addressed in this thesis.

1.4 Expected Contributions

1.4.1 Control-oriented Two-zone Charge Mixing Model

Simplified Charge Mixing Process

Compared to the one-zone and the multi-zone models, the proposed two-zone charge mixing model is promising for describing a complicated turbulent fluid flow during a charge mixing process in an effective manner. Specifically, the proposed model is of great significance on valve motion planning for realization of advanced combustion such as homogeneous charge compression ignition (HCCI) employing substantial amount of hot residual gas for auto-ignition control.

Graphical Analysis for Infrared Images of Optical Engines

With the proposed methodology for graphical analysis, utilization of optical engines to investigate dynamic features of internal combustion engines, such as a charge mixing process, considerably increases. The infrared image taken during the charge mixing process is very chaotic due to a turbulent flow. But, by applying the K-means segmentation technique, the chaotic image can be clustered into several zones. Then, analysis of the finite zone-based model is available from the images.

1.4.2 Frequency Domain Models of An Electrohydraulic Actuator

Spectral Analysis of Electrohydraulic Actuators

Benefits of spectral analysis are achieved for nonlinear electrohydraulic actuators. The electrohydraulic actuator possesses inherent nonlinear dynamic features which result from an orifice flow through a flow control valve and friction forces exerting on a piston and a spool. Through spectral analysis, such nonlinear behaviors can be analyzed efficiently in frequency domain. In addition, spectral analysis reveals great importance on control design and system identification of nonlinear systems.

Nonlinear System Identification in Frequency Domain

The proposed nonlinear system identification has applicability to a range of complex systems of which prior information is limited or not available, for example, mechatronic systems, chemical process, and biological systems. The proposed identification method is numerically stable and robust because it employs well-established (iterative) linear squares methods. In addition, compared to existing methods, the proposed identification method is cheap computationally and experimentally.

1.4.3 Robust Tracking Control of An Electrohydraulic Valve Actuator

Nonstationary Reference Tracking for Nonlinear Systems

The proposed tracking control with a high-order time varying internal model has a range of applications, to be specific, reciprocating machines. Typically, reference signals for the reciprocating machines are defined in position domain, not in time domain, such as reference valve motion of internal combustion engines which is defined in rotational angle domain. The proposed design method turns out to show improved tracking performance even with nonlinear system uncertainties.

1.5 Thesis Organization

The rest of the thesis consists of three main chapters: 1) Control-oriented two-zone charge mixing model, 2) Frequency domain model of an electrohydraulic actuator, 3) Robust tracking control of an electrohydraulic valve actuator.

Chapter 2 The mixing between fresh charge and residual gas is modeled as thermodynamic interaction between two control volumes: the mixed- and the unmixed zone. The GT-power engine simulator and the optical engine are used for model validation. The infrared images are taken from an optical engine, and they are segmented into two zones according to the intensity of image pixels. The thermodynamic properties of two-zone model reveal a good match with the estimates from the images. Through further simulation studies, performance of different valve actuation schemes are investigated and compared.

Chapter 3 Frequency domain models of an electrohydraulic actuator are developed for spectral analysis. Two different methods are presented. An analytic frequency domain model is derived from physical dynamics of the electrohydraulic actuator. This model exhibits the critical nonlinear features of the actuator in frequency domain. An experimental frequency domain model is estimated with the assumption of block-oriented system structures. Even though prior information about the actuator is not available, model parameters are estimated from spectral analysis.

Chapter 4 Robust tracking control of an electrohydraulic valve actuator is presented by applying internal model principle for nonlinear systems. The main focus is to design an internal model to track reference signals whose dynamics is available. Motivated from tracking control for stationary reference signals of which frequency contents are fixed, a high-order time varying internal model is proposed for nonstationary reference tracking. Effectiveness of the proposed internal model design is demonstrated by implementing it on the electrohydraulic camless engine valve actuator.

Chapter 2

Control-oriented Two-zone Charge Mixing Model

In this chapter, a control-oriented two-zone charge mixing model is developed to analyze the effect of variable valve actuation on mixing of fresh charge (air + fuel) and residual gas. With the definitions of two control volumes, the charge mixing model is developed by employing thermodynamic interaction between these two control volumes. The model is validated through the professional engine simulation software and the optical engine. Further simulation studies are conducted to compare different strategies for engine valve actuation in terms of charge mixing. The results of this chapter are reported in [46, 47, 48].

2.1 Introduction

2.1.1 Background

Over the past couple of decades, advanced combustion technologies have been extensively investigated to reduce harmful pollution and improve fuel economy of internal combustion engines (ICEs) [49, 50]. In this perspective, a homogeneous charge compression ignition (HCCI) engine has drawn keen attention as one of the most competitive alternatives. It has been shown that an HCCI engine produces much less nitrogen oxide and soot emissions while improving fuel economy [51]. Fig. 2.1 shows ignition types of

different engines. As can be seen, a compression ignition (CI) engine and a spark ignition (SI) engine employ direct ignition initiators such as an injector and a spark plug. On the other hand, an HCCI engine does not use any explicit initiator. Instead, HCCI is achieved by controlled auto-ignition occurring at multiple spots at a time, when a homogeneous mixture reaches its ignition conditions by compression.

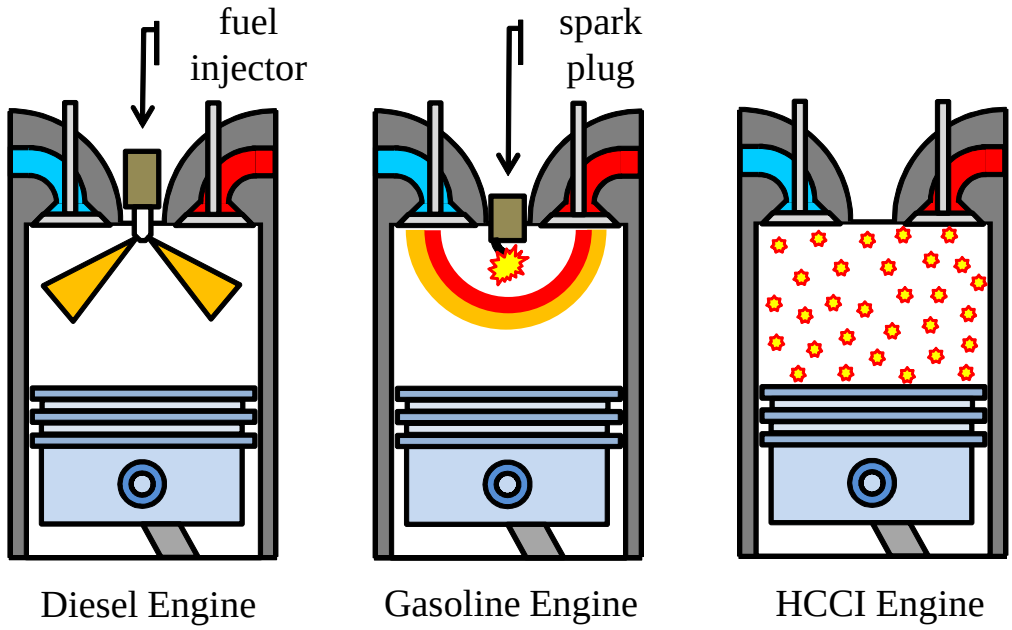

Figure 2.1: Different ignition types: compression ignition (diesel engine), spark ignition (gasoline engine), homogeneous charge compression ignition (HCCI engine).

However, auto-ignition is difficult to control due to the absence of a direct initiator. And the operational range of an HCCI engine is restricted. It is constrained at low load by lean combustion limit and at high load by in-cylinder peak pressure restriction. Variable valve actuation (VVA) turns out to be effective for resolving such challenges. VVA provides fine control over temperature and pressure of a mixture by manipulation of effective compression ratio [52] and amount of hot residual gas retained [53]. Quantitative regulation of hot residual gas reveals great potential for temperature control of the mixture for auto-ignition. In particular, VVA with negative valve overlap (NVO) turns out to be a strong candidate for HCCI combustion control, since NVO strategy

enables effective control of the amount of residual gas to be trapped [23, 54]. However, not all of residual gas trapped affects active reactant. Therefore, appropriate charge mixing model between fresh charge and residual gas is essential for HCCI combustion control and extension of its available range.

Most charge mixing modeling works are based on the assumption of a lumped system. The mean value HCCI engine model is developed in continuous time domain for the control purpose [55]. The cycle-to-cycle based models were also developed [56, 57]. Especially, [57] employed a mass fraction of gas species included in fresh charge and residual gas to predict peak pressure and start of combustion. These approaches commonly assume that thermodynamic properties of in-cylinder gas are uniform without regard of charge mixing.

Actual flow behavior in a cylinder during an intake stroke is extremely chaotic due to turbulence. The turbulence is triggered by a intake flow which comes through intake valves. Thus, thermofluidic characteristics in a cylinder is not uniform at all throughout the cylinder volume. But, turbulence enables mixing of fresh charge and residual gas in a cylinder. It means that mixing of fresh charge and residual gas is strongly influenced by valve timings. The multi-zone model for HCCI is investigated in the framework of computational fluid dynamics [21, 22] to simulate charge mixing and its effect on combustion. Unfortunately, such a model is not suitable for the use of real-time control because it requires extremely heavy computational load. Therefore, it is desired to develop a model with logical and plausible assumptions for simplification, but it still should retain significant physical features for model-based control design. Such a model allows model-based variable valve planning in real-time to facilitate stable HCCI in a broader working range.

As a compromise between the single-zone and multi-zone models, two-zone HCCI models are proposed [58, 59]. However, since the mass transfer between the mixed- and unmixed zone is predetermined with respect to a positive valve overlap strategy in [58], it is not applicable to any other variable valve actuation strategies. Reference [59] assumed the cylindrical shapes of two zones which actually rarely happen. Preliminary results of a modeling work by the author have been reported in [46, 47] and the final results are given in [48].

In the proposed two-zone charge mixing model, the cylinder volume is segmented

into the unmixed- and mixed zones. The unmixed zone includes residual gas only. This zone serves as a temporary repository of hot residual gas which plays a role of the heat source. Whereas, in the mixed zone, it is assumed that fresh charge and some portion of residual gas, expelled from the unmixed zone, are mixed homogeneously. Mass transfer from the unmixed zone to the mixed zone is driven by a fluidic impingement on the unmixed zone. Mass transfer between two zones represents mixing of fresh charge and residual gas in the cylinder.

To validate and calibrate the developed model, optical engine tests were performed with an IR camera. And GT-power simulation is carried out to further assist the model validation. Since an optical engine enables direct access inside a combustion chamber, it is broadly used in ICEs researches, particularly for diagnostic applications such as detection of fuel spray injection and combustion flame propagation [60, 61]. In this research, mean temperature of two zones is estimated from an IR images. Image post-process is done to filter out inevitable noise and to extract features of interest. After post-process, the IR image is segmented into two zones using the K-means cluster technique. Then, the mean temperature of each zone is estimated and compared with the model temperature.

2.1.2 Problem Formulation

The first target of this chapter is to characterize the effect of variable valve actuation on charge mixing model as shown in Fig. 2.2. The model input is the valve timing, lift, and duration (i.e. variable valve actuation), and the model output is the thermodynamic properties of two zones. Experimental condition is regarded as the external input. From the model output, charge mixing can be interpreted.

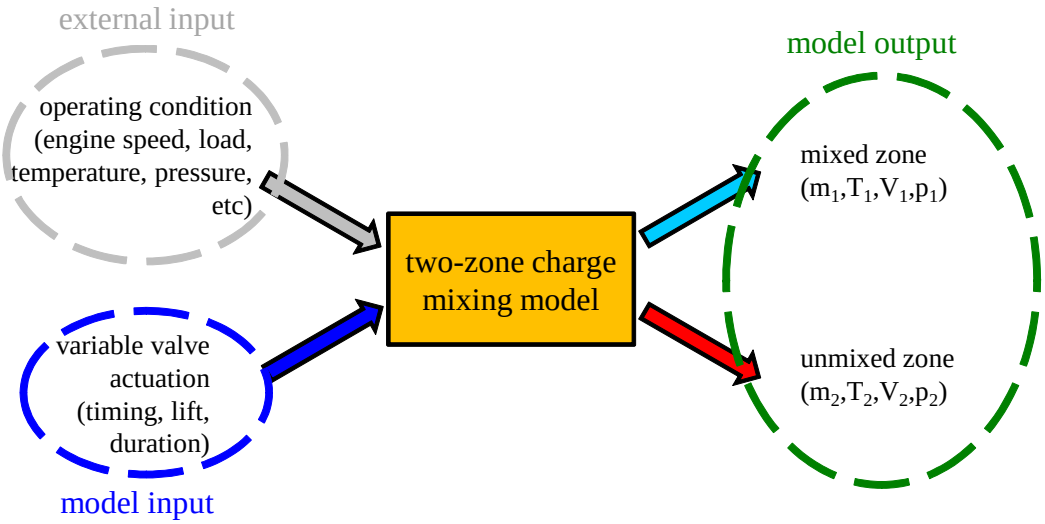

Figure 2.2: Control-oriented two-zone charge mixing model: model input (variable valve actuation), model output (thermodynamics properties of two zones), external input (operating condition).

The next target is validate the model through a systematic graphical analysis of the infrared optical engine. From IR images, thermodynamic properties of two-zones should be extracted. But, in order to achieve that, first the images should be divided into two zones appropriately to represent the mixed- and unmixed zones.

2.1.3 Outline

This chapter is organized as follows: In Sec. 2.2, based on the model definition, a charge mixing model is derived by associating mass transfer between these zones. Then, Sec. 2.3 presents model validation methodologies using an engine simulator and an optical engine. In Sec. 2.4, comparative simulation studies are conducted to investigate the effect of different variable valve actuation on charge mixing. Conclusion of this chapter is drawn in Sec. 2.5.

2.2 Model Development

2.2.1 Model Definition

Fig. 2.3 depicts the charge mixing process with two control volumes: the unmixed- and mixed zones. The fictitious divider (solid green line) is visualized for clear separation between two zones.

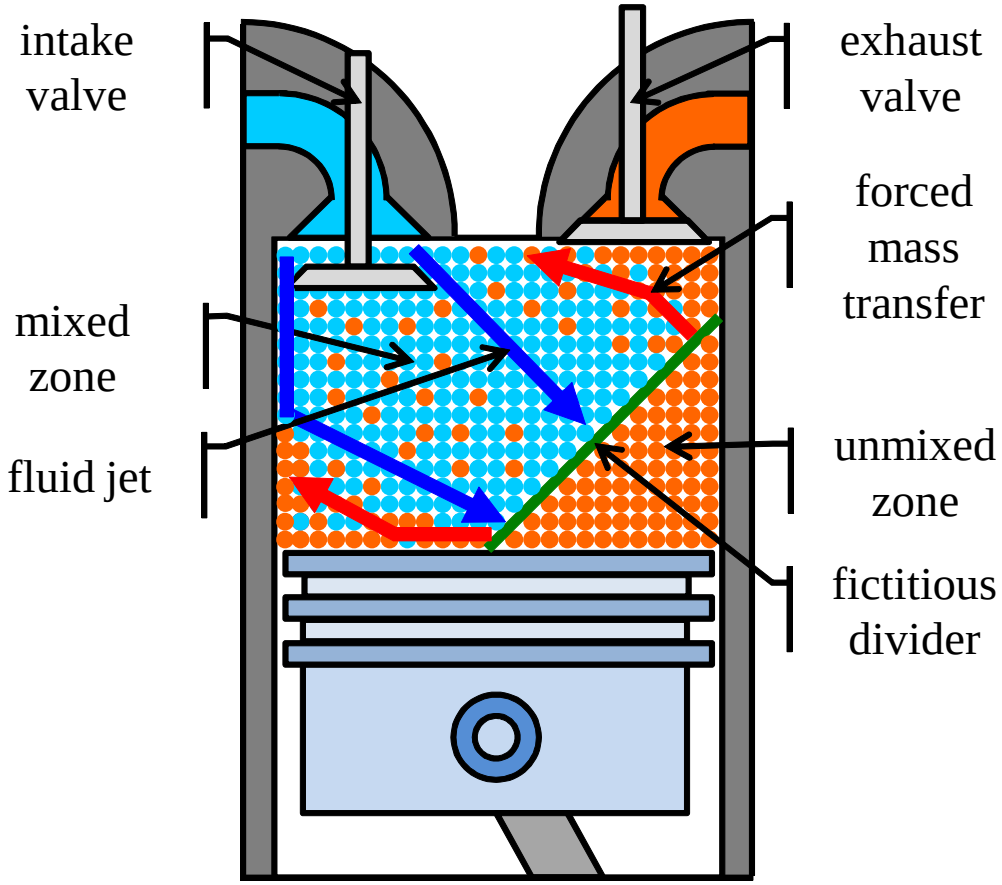

Figure 2.3: Description of the two-zone charge mixing model: a mixture of fresh charge (light blue circles) and residual gas (orange circles) in the mixed zone, residual (orange circles) gas only in the unmixed zone; a fictitious divider between them (solid green line).

Unmixed Zone

The unmixed zone is filled with a portion of residual gas which is retained combustion products of a previous engine cycle by early close of exhaust valves. This burned gas is assumed not to be blended with fresh charge at all. Although this gas remains inert for combustion of a current engine cycle, it plays a significant role as a temporary storage of heat source.

Mixed Zone

The mixed zone is composed of a mixture of fresh charge (fresh air plus fuel) which enters a cylinder in a current engine cycle and some residual gas which is transferred from the unmixed zone. During the charge mixing process, significant heat is transferred from the hot residual gas to the fresh charge and it helps the fresh charge reach the ignition condition. This heat transfer is assumed to occur in the mixed zone only through effective collision, not in the fictitious divider. In other words, charge mixing is realized by the mass transfer from the unmixed zone to the mixed zone (red arrows in Fig. 2.3) which is forced by fluid jets of intake flow acting on the fictitious divider (blue arrows in Fig. 2.3). The fluid jets of intake flow is controlled by active valve motion.

With these assumptions, the effect of valve motion on the charge mixing can be modeled efficiently, while critical physics is still captured. All working fluids are assumed to be an ideal gas. This study concerns the charge mixing during an intake stroke only, though the charge mixing continues until a compression stroke due to inertial fluidic motion. This is because the fluid jet during the intake stroke is the most powerful so that the resultant charge mixing is the most significant.

2.2.2 Model Derivation

Mean properties of the cylinder volume system depending on the engine valve operation are presented, first [62, 63]. Then, those of the mixed- and the unmixed zone are derived. The symbols $m_{(\cdot)}$, $T_{(\cdot)}$, $V_{(\cdot)}$, and $p_{(\cdot)}$ indicate the mass, temperature, volume, and pressure. The subscripts "cyl", "1", and "2" indicate the cylinder volume, the mixed zone, and the unmixed zone, respectively. And the subscripts "im", "em", "IV", and"EV" mean the intake manifold, the exhaust manifold, the intake valve, and the

exhaust valve. respectively. The time derivative is represented by the upper dot.

Cylinder Volume System

From geometry of a single cylinder engine shown in Fig. 2.4, the position and the velocity of the piston pin are given by

$$s(t) = (l+a) - \left(\sqrt{l^2 - a^2 \sin^2 \theta(t)} + a \cos \theta(t) \right) \tag{2.1}$$

$$\dot{s}(t) = \dot{\theta}(t) \left(a \sin \theta(t) + \frac{a^2 \sin \theta(t) \cos \theta(t)}{\sqrt{l^2 - a^2 \sin^2 \theta(t)}} \right), \tag{2.2}$$

where a and l indicate the crank radius and the connecting rod length. $\theta(t)$ means the engine position in crank angle domain.

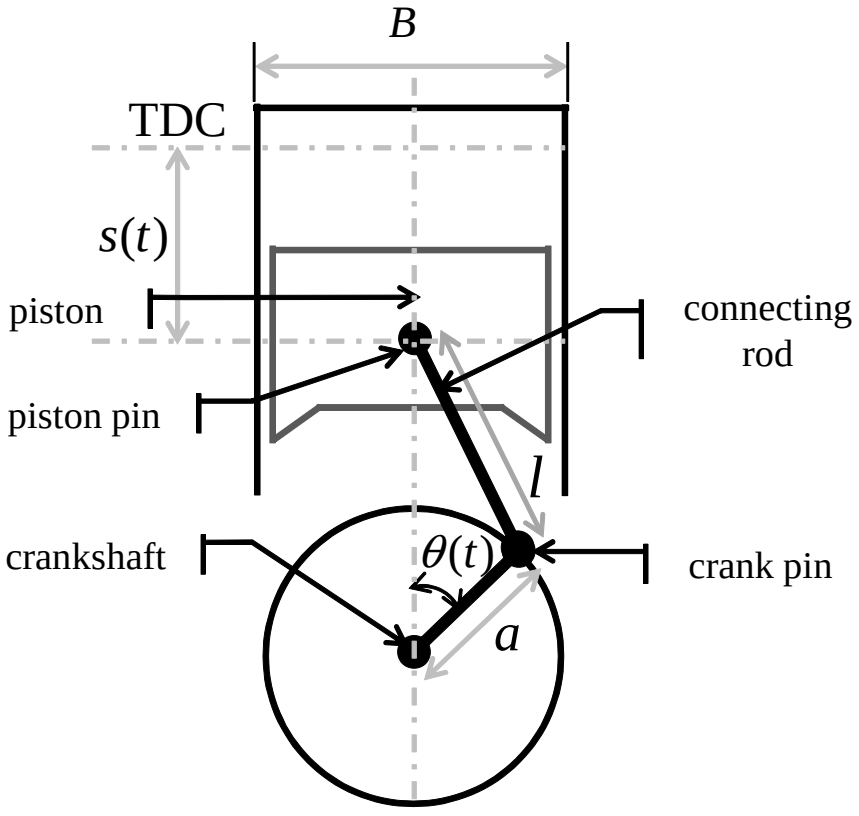

Figure 2.4: Geometry of a single cylinder engine

The cylinder volume and its rate are given by

$$V_{\mathrm{cyl}}(t) = V_{\mathrm{d}}\left(\frac{1}{r_{\mathrm{c}}-1}+\frac{s(t)}{2a}\right) \tag{2.3}$$

$$\dot{V}_{\mathrm{cyl}}(t) = \frac{V_{\mathrm{d}}}{2a}\dot{s}(t), \tag{2.4}$$

where V_{d} is the displacement volume swept by the piston while it moves between the top dead center (TDC) and the bottom dead center (BDC). r_{c} is the compression ratio of the engine.

Applying the mass and energy conservation law, and the ideal gas law to the cylinder volume system yields the following thermodynamic equations of the cylinder volume system

$$\dot{m}_{\mathrm{cyl}}(t) = \dot{m}_{\mathrm{v}}(t) \tag{2.5}$$

$$\begin{aligned}\dot{T}_{\mathrm{cyl}}(t) &= \frac{\gamma-1}{m_{\mathrm{cyl}}(t)R}\left(-p_{\mathrm{cyl}}(t)\dot{V}_{\mathrm{cyl}}(t)+\dot{Q}_{\mathrm{cyl}}(t)\right)\\ &+ \begin{cases}\dfrac{\dot{m}_{\mathrm{v}}(t)}{m_{\mathrm{cyl}}(t)}\left(\gamma T_{\mathrm{im}}-T_{\mathrm{cyl}}(t)\right) & , \text{ if inflow through IV}\\ \dfrac{\dot{m}_{\mathrm{v}}(t)}{m_{\mathrm{cyl}}(t)}\left(\gamma T_{\mathrm{em}}-T_{\mathrm{cyl}}(t)\right) & , \text{ if inflow through EV}\\ \dfrac{\dot{m}_{\mathrm{v}}(t)}{m_{\mathrm{cyl}}(t)}\left(\gamma-1\right)T_{\mathrm{cyl}}(t) & , \text{ if outflow}\end{cases}\end{aligned} \tag{2.6}$$

$$\dot{p}_{\mathrm{cyl}}(t) = \frac{1}{V_{\mathrm{cyl}}(t)}\left(\dot{m}_{\mathrm{cyl}}(t)RT_{\mathrm{cyl}}(t)+m_{\mathrm{cyl}}(t)R\dot{T}_{\mathrm{cyl}}(t)-p_{\mathrm{cyl}}(t)\dot{V}_{\mathrm{cyl}}(t)\right), \tag{2.7}$$

where $\dot{m}_{\mathrm{v}}(t)$ is the valve flow rate. And, γ and R are the heat capacity ratio and specific gas constant. $\dot{Q}_{\mathrm{cyl}}(t)$ means the heat transfer rate from/to the cylinder wall given by

$$\dot{Q}_{\mathrm{cyl}}(t) = -h_{\mathrm{cyl}}(t)A_{\mathrm{cyl}}(t)\left(T_{\mathrm{cyl}}(t)-T_{\mathrm{wall}}\right), \tag{2.8}$$

where T_{wall} is the cylinder wall temperature, and $A_{\mathrm{cyl}}(t)$ is the contact area with the cylinder wall. The heat transfer coefficient $h_{\mathrm{cyl}}(t)$ is determined by Woschni's correlation with the scalable factor α depending on engine geometry such as [62, 63]

$$h_{\mathrm{cyl}}(t) = \alpha\, L^{-0.2}\, p_{\mathrm{cyl}}(t)^{\,0.8}\, T_{\mathrm{cyl}}(t)^{-0.55}\omega(t)^{0.8}, \tag{2.9}$$

where L and ω are the characteristics length and velocity of the engine.

Valve Flow Rate

The valve flow rate and the flow velocity are given by

$$\dot{m}_{\mathrm{v}}(t) = \frac{C_{\mathrm{d}} A_{\mathrm{c}}(t)}{\sqrt{RT_{\mathrm{up}}}} p_{\mathrm{up}} \Phi\left(r_{\mathrm{p}}(t)\right) \tag{2.10}$$

$$v_{\mathrm{v}}(t) = C_{\mathrm{d}} \sqrt{RT_{\mathrm{up}}} \Phi\left(r_{\mathrm{p}}(t)\right), \tag{2.11}$$

where C_{d} is the discharge coefficient, and $A_{\mathrm{c}}(t)$ is the curtain area of the valve determined by the valve lift. The subscript "up" means an upper stream. Flow direction is determined in accordance with pressure gradient through the valve. In this paper, the positive valve flow means the inflow into the cylinder volume, and the negative valve flow is vice versa. $\Phi\left(r_p(t)\right)$ is given by

$$\Phi\left(r_{\mathrm{p}}(t)\right) = \begin{cases} r_{\mathrm{p}}(t)^{\frac{1}{\gamma}} \sqrt{\dfrac{2\gamma}{\gamma-1}\left(1 - r_{\mathrm{p}}(t)^{\frac{\gamma-1}{\gamma}}\right)} & , \text{ if } r_{\mathrm{p}}(t) > \left(\dfrac{2}{\gamma+1}\right)^{\frac{\gamma}{\gamma-1}} \\ \sqrt{\gamma \left(\dfrac{2}{\gamma+1}\right)^{\frac{\gamma+1}{\gamma-1}}} & , \text{ if } r_{\mathrm{p}}(t) \leq \left(\dfrac{2}{\gamma+1}\right)^{\frac{\gamma}{\gamma-1}} \end{cases} \tag{2.12}$$

where r_{p} is the pressure ratio of an upper stream and a down stream.

It is mentioned that the fluid jet generated by strong inflow is the essential driving force for charge mixing and consequentially turbulence induced by the jet provokes pressure imbalance [64, 65]. From the energy conservation law of a fresh charge in motion, when the fluid jet hits the fictitious divider, its impact pressure is given by

$$p_{\mathrm{jet}}(t) = \frac{p_{\mathrm{im}} v_{\mathrm{v}}(t)^2}{2RT_{\mathrm{im}}} \tag{2.13}$$

During the intake stroke, since $p_{\mathrm{cyl}}(t)$ is close to p_{im}, the ratio of $p_{\mathrm{jet}}(t)$ and $p_{\mathrm{cyl}}(t)$ is approximated by $C_{\mathrm{d}}^2 \Phi\left(r_{\mathrm{p}}(t)\right)^2/2$ which means $p_{\mathrm{jet}}(t)$ is much smaller than $p_{\mathrm{cyl}}(t)$. Thus, the pressure imbalance is nearly negligible compared to the mean cylinder pressure, although it is critical for charge mixing. Therefore, the pressure of cylinder volume is assumed to be uniform without spatial difference.

Mixed Zone

The mixed zone has two inlets during inflow and one outlet during outflow. During the outflow from the cylinder to the manifold (intake or exhaust), the escape rate from each zone is assumed to be determined according to its mass fraction. By applying the mass and energy conservation law, and the ideal gas law to the mixed zone, the following thermodynamic equations are yielded

$$\dot{m}_1(t) = \begin{cases} \dot{m}_{\mathrm{v}}(t) + \dot{m}_{\mathrm{t}}(t) & , \quad \text{if inflow} \\ \dot{m}_{\mathrm{cyl}}(t) \times \dfrac{m_1(t)}{m_{\mathrm{cyl}}(t)} & , \quad \text{if outflow} \end{cases} \tag{2.14}$$

$$\frac{d}{dt}\left(m_1(t)c_{\mathrm{v}}T_1(t)\right) = -p_{\mathrm{cyl}}(t)\dot{V}_1(t) + \dot{Q}_1(t) \tag{2.15}$$

$$+ \begin{cases} \dot{m}_{\mathrm{v}}(t)c_{\mathrm{p}}T_{\mathrm{im}} + \dot{m}_{\mathrm{t}}(t)c_{\mathrm{p}}T_2(t) & , \quad \text{if IV inflow} \\ \dot{m}_{\mathrm{v}}(t)c_{\mathrm{p}}T_{\mathrm{em}} + \dot{m}_{\mathrm{t}}(t)c_{\mathrm{p}}T_2(t) & , \quad \text{if EV inflow} \\ \dot{m}_1(t)c_{\mathrm{p}}T_1(t) & , \quad \text{if outflow} \end{cases}$$

$$-p_{\mathrm{cyl}}(t)\dot{V}_1(t) + m_1(t)R\dot{T}_1(t) = \dot{p}_{\mathrm{cyl}}(t)V_1(t) - \dot{m}_1(t)RT_1(t) \tag{2.16}$$

$\dot{m}_{\mathrm{t}}(t)$ is the mass transfer rate from the unmixed zone. c_{v} and c_{p} are the specific heat capacity at iso-choric, and iso-baric process. The heat transfer rate from/to the cylinder wall for the mixed zone is given by

$$\dot{Q}_1 = -h_1 A_1 \left(T_1(t) - T_{\mathrm{wall}}\right), \tag{2.17}$$

where h_1 and A_1 are defined for the mixed zone similarly with the cylinder volume system, and their calculation is presented in the following.

Unmixed Zone

The unmixed zone has one outlet. The unmixed zone consistently shrinks until it fades away completely. Similarly, thermodynamic equations for the unmixed zone are given by

$$\dot{m}_2(t) = \begin{cases} -\dot{m}_{\mathrm{t}}(t) & , \quad \text{if inflow} \\ \dot{m}_{\mathrm{cyl}}(t) \times \dfrac{m_2(t)}{m_{\mathrm{cyl}}(t)} & , \quad \text{if outflow} \end{cases} \tag{2.18}$$

$$\frac{d}{dt}\left(m_2(t)c_{\mathrm{v}}T_2(t)\right) = -p_{\mathrm{cyl}}(t)\dot{V}_2(t) + \dot{Q}_2(t) + \dot{m}_2(t)c_{\mathrm{p}}T_2(t) \tag{2.19}$$

$$-p_{\mathrm{cyl}}(t)\dot{V}_2(t) + m_2(t)R\dot{T}_2(t) = \dot{p}_{\mathrm{cyl}}(t)V_2(t) - \dot{m}_2(t)RT_2(t) \tag{2.20}$$

The heat transfer rate for the unmixed zone is determined similarly.

$$\dot{Q}_2(t) = -h_2 A_2 \left(T_2(t) - T_{\text{wall}}\right) \tag{2.21}$$

For (2.17) and (2.21), the following assignment rule is used:

$$h_1 A_1 = \frac{m_1(t)}{m_{\text{cyl}}(t)} h_{\text{cyl}} A_{\text{cyl}} \tag{2.22}$$

$$h_2 A_2 = \frac{m_2(t)}{m_{\text{cyl}}(t)} h_{\text{cyl}} A_{\text{cyl}} \tag{2.23}$$

It is noted that the multiplication of the heat transfer coefficient and the contact area can be determined only, not individual values. It is because the contact area cannot be determined due to complex shapes of zones.

Mass Transfer Between Two Zones

The two-zone charge mixing model is indeterminate because of unknown mass transfer rate between two zones $\dot{m}_{\text{t}}$. It is reminded that residual gas in the unmixed zone is transferred to the mixed zone by impact pressure exerting on the fictitious divider while keeping pressure of both zones identical (or nearly similar). It means that the compression work by a fluid jet is consumed by enthalpy outflow, in other words, $p_{\text{jet}}(t)\dot{V}_{\text{t}}(t) = \dot{m}_{\text{t}}(t) c_{\text{p}} T_2(t)$. $\dot{V}_{\text{t}}(t)$ is approximated by $\dot{V}_{\text{v}}(t) = \dot{m}_{\text{v}}(t)/\rho_{\text{im}}$. Finally, the mass transfer rate between two zones is determined with the constant mixing parameter (η) such as

$$\dot{m}_{\text{t}}(t) = \eta \frac{\gamma - 1}{\gamma} \frac{\dot{m}_{\text{v}}(t) v_{\text{v}}(t)^2}{2RT_2(t)} \tag{2.24}$$

From (2.24), the mass transfer rate between two zones is proportional to the kinetic energy rate of intake flow, i.e. the fluid jet. The mixing parameter η is used to represent the engine geometry-dependent effect on the turbulence.

Two-zone Charge Mixing Model

By combining thermodynamics of the cylinder volume system, the mixed zone, and the unmixed zone, the two-zone charge mixing model can be written by

$$\Sigma(t) X(t) = \Pi(t) \tag{2.25}$$

$\Sigma(t)$, $X(t)$, and $\Pi(t)$ are given by

$$\Sigma(t) = \begin{bmatrix} m_1(t)c_{\mathrm{v}} & 0 & p_{\mathrm{cyl}}(t) & 0 \\ 0 & m_2(t)c_{\mathrm{v}} & 0 & p_{\mathrm{cyl}}(t) \\ m_1(t)R & 0 & -p_{\mathrm{cyl}}(t) & 0 \\ 0 & m_2(t)R & 0 & -p_{\mathrm{cyl}}(t) \end{bmatrix} \tag{2.26}$$

$$X(t) = \begin{bmatrix} \dot{T}_1(t) & \dot{T}_2(t) & \dot{V}_1(t) & \dot{V}_2(t) \end{bmatrix}^T \tag{2.27}$$

$$\Pi(t) = \begin{cases} \begin{bmatrix} -\dot{m}_1(t)c_{\mathrm{v}}T_1(t) - \dot{m}_2(t)c_{\mathrm{p}}T_2(t) + \dot{m}_{\mathrm{v}}(t)c_{\mathrm{p}}T_{\mathrm{im}} - \dot{Q}_1(t) \\ \dot{m}_2(t)RT_2(t) - \dot{Q}_2(t) \\ -\dot{m}_1(t)RT_1(t) + \dot{p}_{\mathrm{cyl}}(t)V_1(t) \\ -\dot{m}_2(t)RT_2(t) + \dot{p}_{\mathrm{cyl}}(t)V_2(t) \end{bmatrix}, & \text{if IV inflow} \\ \begin{bmatrix} -\dot{m}_1(t)c_vT_1(t) - \dot{m}_2(t)c_pT_2(t) + \dot{m}_{\mathrm{v}}(t)c_{\mathrm{p}}T_{\mathrm{em}} - \dot{Q}_1(t) \\ \dot{m}_2(t)RT_2(t) - \dot{Q}_2(t) \\ -\dot{m}_1(t)RT_1(t) + \dot{p}_{\mathrm{cyl}}(t)V_1(t) \\ -\dot{m}_2(t)RT_2(t) + \dot{p}_{\mathrm{cyl}}(t)V_2(t) \end{bmatrix}, & \text{if EV inflow} \\ \begin{bmatrix} \dot{m}_1(t)RT_1(t) - \dot{m}_2(t)c_{\mathrm{p}}T_2(t) - \dot{Q}_1(t) \\ \dot{m}_2(t)RT_2(t) - \dot{Q}_2(t) \\ -\dot{m}_1(t)RT_1(t) + \dot{p}_{\mathrm{cyl}}(t)V_1(t) \\ -\dot{m}_2(t)RT_2(t) + \dot{p}_{\mathrm{cyl}}(t)V_2(t) \end{bmatrix}, & \text{if outflow} \end{cases} \tag{2.28}$$

It is noted that the variables of the cylinder volume system are treated as the exogenous signals of the two-zone charge mixing model.

2.3 Model Validation

In this section, a GT-power simulator and an optical engine are used for calibration of global parameters of the cylinder volume system and a local parameter of two zones,

respectively. Since the proposed two-zone charge mixing model is defined during an intake stroke only, and it does not require any specific combustion, the optical engine and the GT-power simulator are run with spark ignition (SI) for a consistent use of residual gas under stable combustion.

2.3.1 GT-Power Simulation

The GT-power simulator is run to track the optical engine measurements such as indicated mean effect pressure (IMEP), air fuel ratio (AFR), P_{cyl}, and fuel mass. The global parameters are calibrated so that the Matlab simulink model follows the GT-power simulator model. It is noted that the GT-power simulator is used to generate mean temperature which is not available in the optical engine. The global parameters include the heat transfer coefficient α used in (2.9), and the discharge coefficient C_{d} for intake and exhaust valves used in (2.10) and (2.11).

The engine runs at steady speed of 1500 RPM. The compression ratio is 9.8 and the displacement volume is 0.499 liter. AFR is kept at the stoichiometric raio, and the indoline is used as the fuel for optical engine tests. Experimental conditions are shown in Table. 2.1. The valve timing of EVO, EVC, IVO, and IVC are -168, -20, 32, and 180 in crank angle degree (CAD) with respect to the TDC) position during the intake stroke. Zero indicates TDC position during the intake stroke. The calibrated values of C_{d} and α are 0.85 and 2.00, respectively. Fig. 2.5 shows the valve profile used and mean value comparisons of pressure, temperature, and mass for the in-cylinder gas. With calibrated parameters, acceptable levels of agreement are achieved.

Table 2.1: Experimental conditions of optical engine tests

Valve Diameter (mm)		Single Cylinder Engine (mm)		
intake	exhaust	B	l	d_{win}
34	30	86	146	58
Pressure (bar)		Temperature (K)		
intake	exhaust	intake	exhaust	wall
0.55	0.85	300	800	400

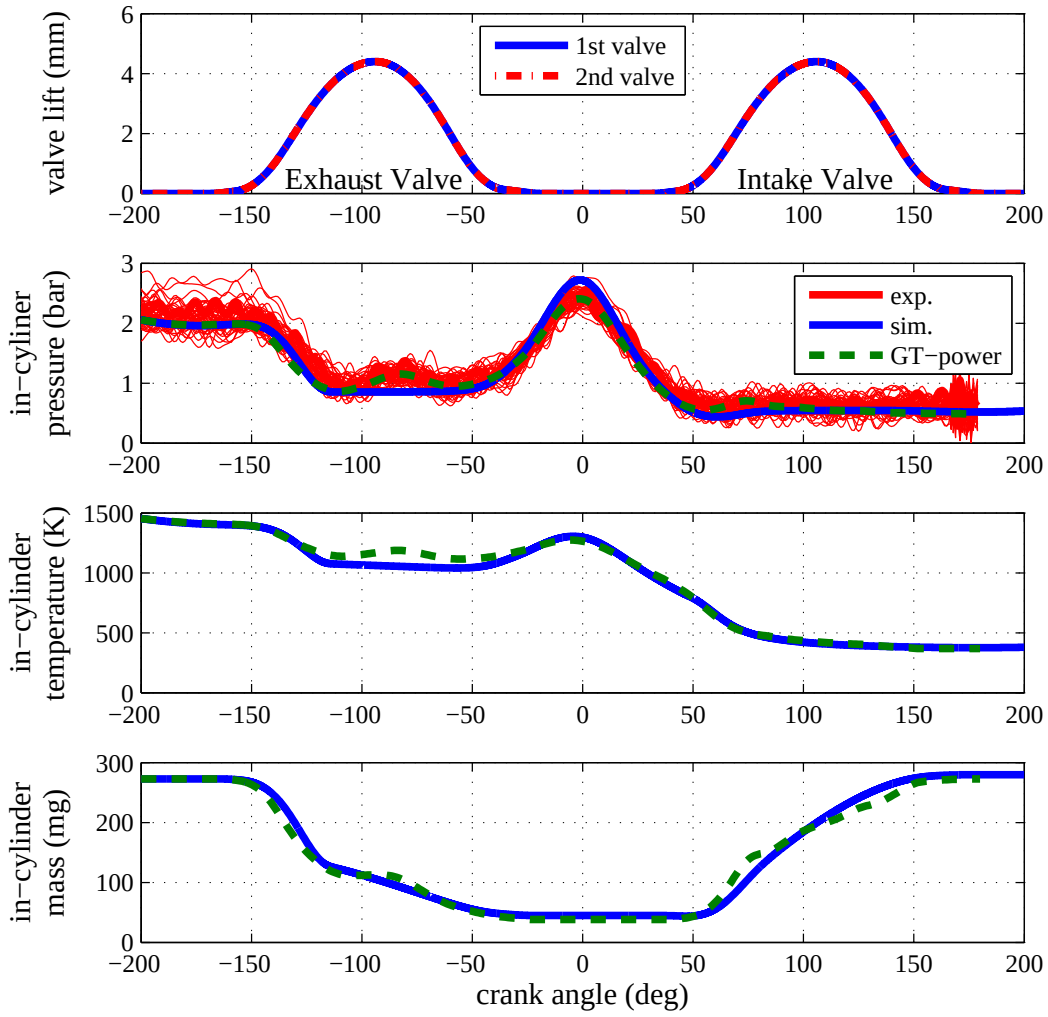

Figure 2.5: Cylinder volume system parameter calibration: first row - valve profile used, second row - in-cylinder pressure (p_{cyl}), third row - in-cylinder temperature (T_{cyl}), fourth row - in-cylinder mass (m_{cyl}).

With the calibrated global parameters, further comparative simulations are conducted with different local parameters η used in (2.24) to investigate its effect on two zones. Fig. 2.6 shows comparison results. The mixing degree is defined as the mass ratio of transferred residual gas to the mixed zone at IVC and total retained residual gas at IVO. With the given valve actuation, the mixed zone is generated after 40 CAD

because of a back flow in the beginning of IVO. From Fig. 2.6, it is found that the mixing degree does not affect temperature of the unmixed zone. However, temperature of the mixed zone is obviously influenced by the mixing degree. This dependence of the mixed zone is utilized for calibration of *eta* with the optical engine.

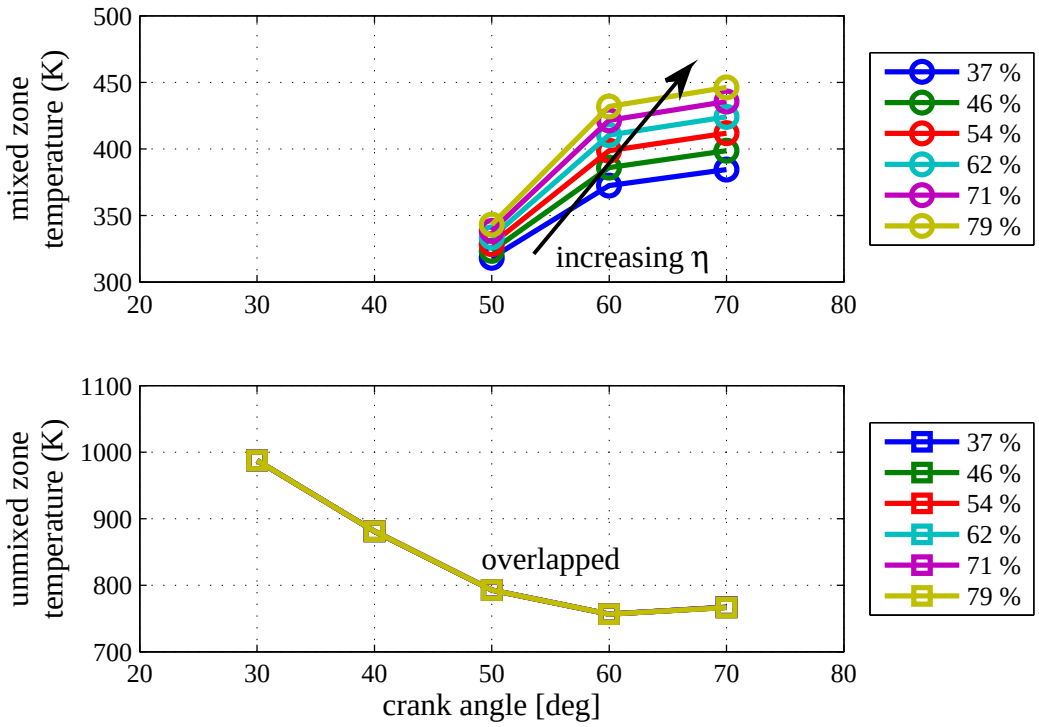

Figure 2.6: Zonal temperature according to mixing degrees, $m_t(\theta_{IVC})/m_2(\theta_{IVO})$: temperature of the mixed (top) and unmixed (bottom) zone.

2.3.2 Optical Engine Test

The proposed model presents thermodynamic interaction between the mixed and unmixed zones, in terms of mass transfer between them. Unfortunately, there are no available sensors other than pressure transducers that are capable of measuring in-cylinder properties because of high pressure and temperature in a cylinder. Due to such restriction, an optical engine has drawn attention for ICE research, since it allows direct optical access to the inside of a cylinder so that significant features like fuel spray

injection and combustion flame propagation can be captured by images. In this research, an IR camera was used to estimate the mean temperature of two zones during the intake stroke. Then, the mixing parameter η is calibrated using the estimated temperature. Thereby, suitability of the proposed model is evaluated.

Optical Engine Setup

The schematic setting of the optical engine is shown in Fig. 2.7. Radiant emittance from gas in the cylinder passes through the optical window which is mounted on the Bowditch style piston. Because the diameter of the optical window is smaller than the engine bore, only some portion of gas in the cylinder can be observed. After passing through the window, the radiation is reflected from the mirror, then reaches the detector. At 30, 40, 50, 60, and 70 CAD, images are taken ten times in consecutive cycles to see chaotic variation.

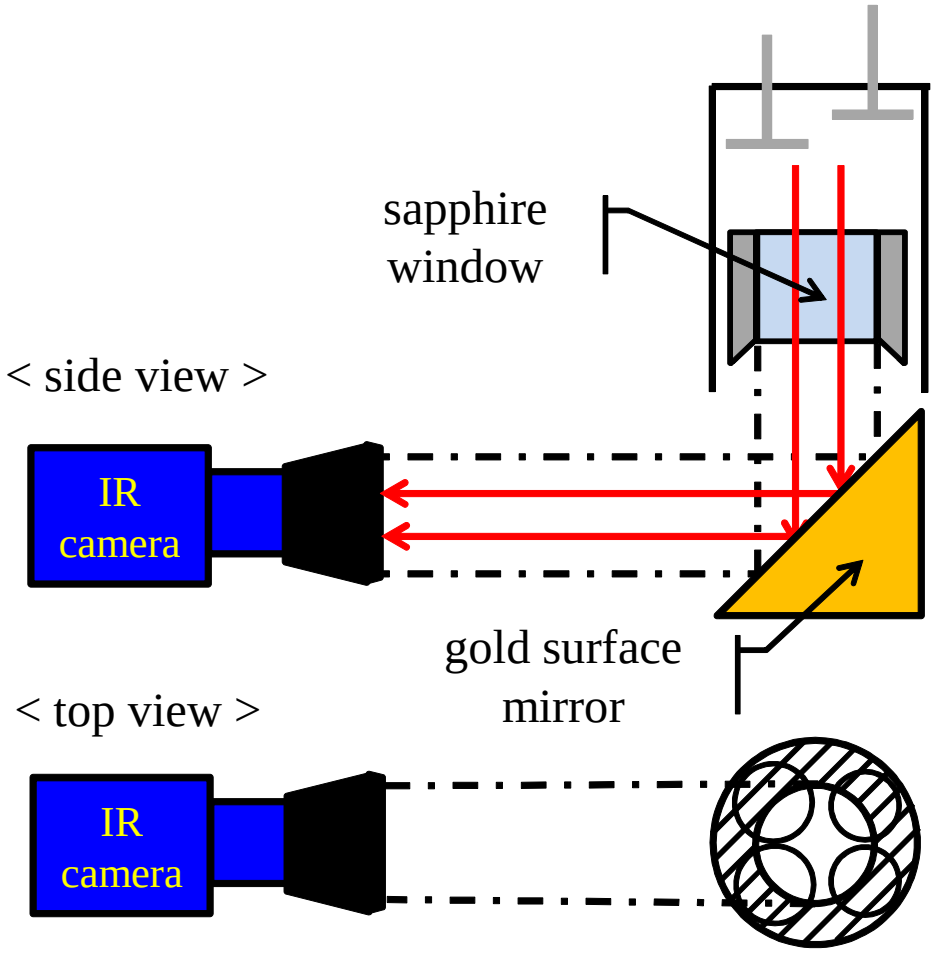

Figure 2.7: Principle of the optical engine.

Radiation Energy

Detailed theoretical background of radiation transfer can be found in [25]. Evert material of which surface temperature is over zero degree Kelvin emits radiation from its surface. For a blackbody, spectral radiant emittance from its surface is determined with Plank law as a function of wave length (k) and surface temperature (T). A real object of identical surface temperature emits less radiation than an ideal blackbody, and their ratio is defined as emissivity. In contrast with a solid surface, a majority of gases features nonuniform spectral distribution of emissivity. And most gases turn out

to have extremely small emissivity. Thus instead of gas, soot which is one of combustion products is generally employed for an optical engine test to estimate the combustion temperature, because it has much higher emissivity than gas. There have been many efforts to estimate soot emissivity for optical engine research [60, 61].

If all radiant emittance from the object in the cylinder reaches the detector without any loss, the measured image output (i.e. intensity) is determined as

$$U = \int_{\lambda_1}^{\lambda_2} \kappa(\lambda)\epsilon(\lambda)E_{\mathrm{b}}(\lambda, T)d\lambda \tag{2.29}$$

where κ is the normalized productivity of the detector which converts from the incident radiation to the actual image output. [λ_1, λ_2] are the measurable spectral range of the IR camera. It is noted that the image output mainly depends on the surface temperature and emissivity of an object.

Image Process

The median filter is applied in order to filter out undesired noise sufficiently without unnecessary distortion of structural features [27]. Besides noise suppression, the filter gets rid of isolated pixels in the mixed zone. If tiny portion of the residual gas is mixed with fresh charge, it appears as a small isolated region having high intensity. By applying median filter, such an isolated region could be included in the mixed zone.

After filtering, pixels outside the optical window are excluded because pixels showing intensity of in-cylinder gas are concerned for zone identification from IR images. And the pixels where the spark plug locates are ruled out either. As presented, soot is used for temperature estimation. Soot is likely to be accumulated on the spark plug and cylinder head. Because temperature of the spark plug remains high, excessively high image output around the spark plug is found. Therefore, pixels except these area are used for image segmentation.

To partition the images into two zones, the K-means cluster method is employed [66]. This technique partitions pixels into K clusters to minimize the predetermined cost function given by

$$J_{\mathrm{i,j}}^{(\mathrm{k})} = \beta|U_{\mathrm{i}} - \bar{U}_{\mathrm{j}}^{(\mathrm{k})}|^2 + (1-\beta)||P_{\mathrm{i}} - \bar{P}_{\mathrm{j}}^{(\mathrm{k})}|| \tag{2.30}$$

where, $U_{\mathrm{i}} \in \mathbb{R}$, $P_{\mathrm{i}} \in \mathbb{R}^2$, $\bar{U}_{\mathrm{j}}^{(\mathrm{k})} \in \mathbb{R}$, and $\bar{P}_{\mathrm{j}}^{(\mathrm{k})} \in \mathbb{R}^2$. The following describes the iterative algorithm of the optimal k-means cluster method.

K-means cluster iterative algorithm

1) determine initial values of $\bar{U}_{\mathrm{j}}^{(0)}$, $\bar{P}_{\mathrm{j}}^{(0)}$ for $\forall$ j_{th} cluster.

2) for the i_{th} cell, find the j_{th} cluster to minimize (2.30), then assign the i_{th} pixel to the j_{th} cluster.

3) update mean values of new clusters: $\bar{U}_{\mathrm{j}}^{(\mathrm{k}+1)}$, $\bar{P}_{\mathrm{j}}^{(\mathrm{k}+1)}$

4) go to **2)** until cluster assignment doe not change.

Although this algorithm solves the local solution, an initial value turns out to be nearly insensitive to optimal image segmentation through numerical examination, if the solutions (the mean image output and pixel location of clusters) are constrained to integers.

It is found that soot distribution is rather nonuniform even in the unmixed zone (see the raw image measured at 40 CAD before the mixed zone appears in Fig. 2.8). Unless such non-uniformity in the unmixed zone is taken account, temperature estimation based on the image segmentation would not be accurate. Two clusters are used for the unmixed zone. After inflow occurs, including one for the mixed zone, three clusters appear in the images. Fig. 2.8 shows one of the raw (left) and segmented (right) images at 40, 50, 60, and 70 CAD. In each plot, the above bigger and the below smaller arcs indicate the intake and exhaust valves, respectively. The red cluster is the area where much soot is concentrated in the unmixed zone. The yellow cluster is the area where sparse soot exists in the unmixed zone. And the light blue cluster represents the mixed zone. The dark blue indicates the excluded area for image segmentation. It is noted that all images are scaled using the discontinuous color map. The optimal mean intensity for each cluster ($\bar{U}_{\mathrm{j}}$, the final iteration number is omitted for convenience.) will be used for mean temperature estimation of each zone.

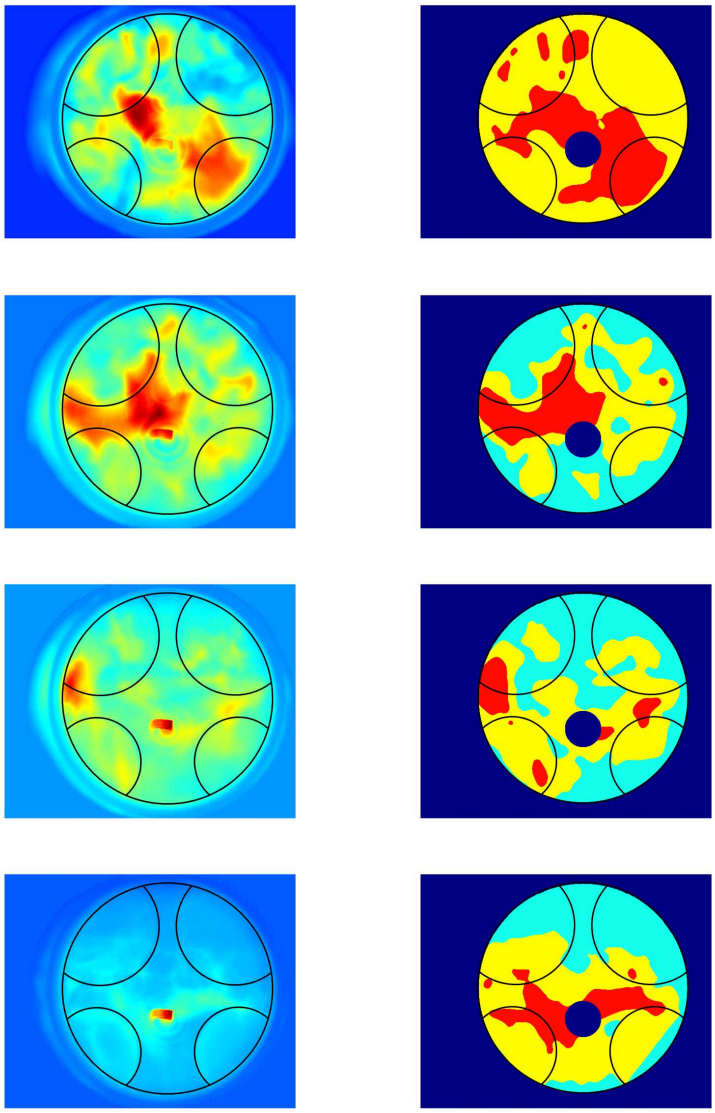

Figure 2.8: Infrared image segmentation: Rows - 40, 50, 60, 70 degree in order, Left - raw images, Right - segmented images. The upper and lower arcs indicate the intake and exhaust valves.

Zonal Temperature Estimation

Since in-cylinder gas has very low emissivity, in other words it is transparent to radiation, the detector observes radiation emitted from the background parts such as

the cylinder head, valve ports, and the spark plug, in addition to gas radiation. Fig. 2.9 depicts the path of radiant emittance from the gas and background parts to the detector. Therefore, radiant overlap on IR images should be taken account. Based on Eq. (2.29) and radiant path shown in Fig. 2.9, the mean intensity of the j_{th} cluster is given by

$$\begin{aligned} \bar{U}_{\mathrm{j}} &= \bar{U}_{\mathrm{gas,j}} + \bar{U}_{\mathrm{bg,j}} \\ \bar{U}_{\mathrm{gas,j}} &= \int_{\lambda_1}^{\lambda_2} \kappa(\lambda)\tau_{\mathrm{amb}}\tau_{\mathrm{win}}\epsilon_{\mathrm{gas,j}}(\lambda)E_{\mathrm{b}}(\lambda, T_{\mathrm{gas,j}})\, d\lambda \\ \bar{U}_{\mathrm{bg,j}} &= \int_{\lambda_1}^{\lambda_2} \kappa(\lambda)\tau_{\mathrm{amb}}\tau_{\mathrm{win}}\tau_{\mathrm{gas,j}}(\lambda)\epsilon_{\mathrm{bg}}E_{\mathrm{b}}(\lambda, T_{\mathrm{bg}})\, d\lambda \end{aligned} \tag{2.31}$$

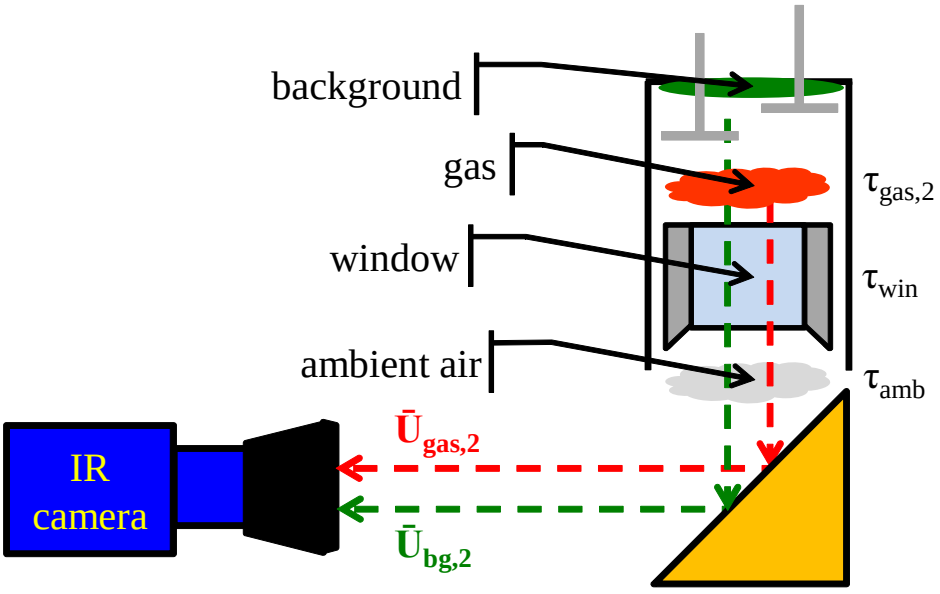

Figure 2.9: Path of radiant emittance: the IR detector receives radiant emittance from background and gas both. Thickness of ambient air changes as a piston moves up or down.

Transmissivity of the ambient gap is variant to crank angle, because optical thickness of the ambient gap varies while the piston head moves down. To compensate a dynamic optical thickness, pixels outside the optical window is used. The intensity of these pixels represents radiation emitted from the piston head. It is supposed to remain nearly constant, because piston temperature is also controlled by engine coolant. However,

the measured mean intensity of these pixels is found to change while the piston head moves downward. To compensate such varying transmissivity, the normalizing factor, $N(\theta)$, is defined to cancel out decreasing transmittance while the piston head moves down. In other words, $\tau_{\mathrm{amb}}(\theta) = \tilde{\tau}_{\mathrm{amb}} \times N(\theta)$ with the constant $\tilde{\tau}_{\mathrm{amb}}$. Therefore, normalized mean values of $\tilde{U}_{\mathrm{j}} = \bar{U}_{\mathrm{j}}/N(\theta)$, $\tilde{U}_{\mathrm{gas,j}} = \bar{U}_{\mathrm{gas,j}}/N(\theta)$, $\tilde{U}_{\mathrm{bg,j}} = \bar{U}_{\mathrm{bg,j}}/N(\theta)$, and $\tilde{U}_{\mathrm{piston}} = \bar{U}_{\mathrm{piston}}/N(\theta)$ are used for temperature estimation. $\tilde{U}_{\mathrm{j}}$ of the j_{th} cluster is shown in Fig. 2.10.

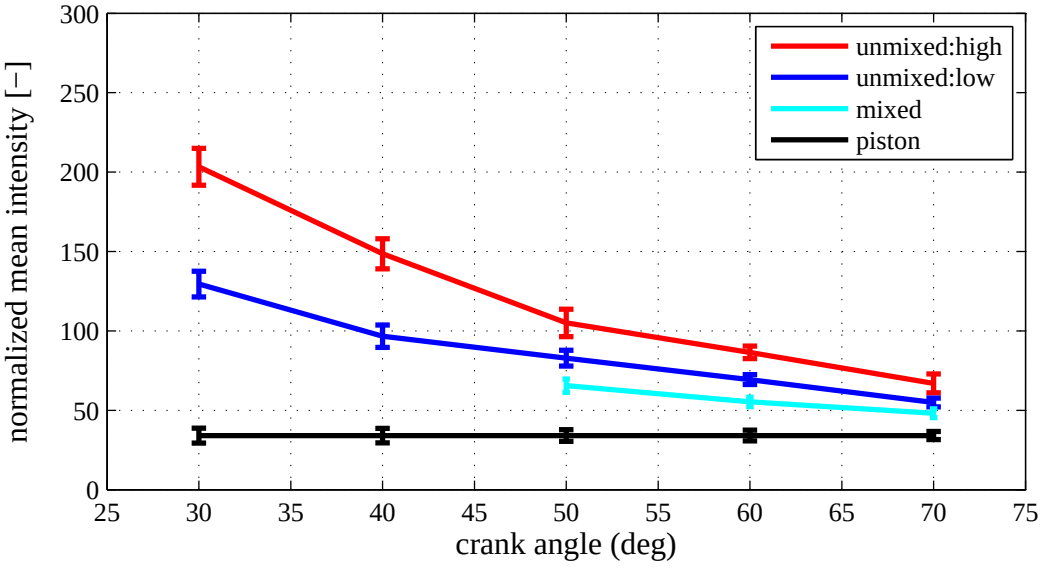

Figure 2.10: Normalized intensity regarding thickness varying ambient air - dense(red) and sparse(blue) soot clusters in the unmixed zone, cluster(light blue) of the mixed zone, piston head(black), i.e. outside of the optical window)

To estimate $T_{\mathrm{gas,j}}$ from $\tilde{U}_{\mathrm{gas,j}}$, $\tilde{U}_{\mathrm{gas,j}}$ should be extracted from $\tilde{U}_{\mathrm{j}}$ in (2.31). κ, $\epsilon_{\mathrm{gas,j}}$, and $\tau_{\mathrm{gas,j}}$ of gas are assumed to be constant for computational simplicity. Constant soot emissivity of 0.5 is selected from the literature [61]. This emissivity corresponds to the soot of combustion gas. The normalized mean intensity of the unmixed zone ($\tilde{U}_{\mathrm{gas},2}$) is nearly identical to $\tilde{U}_2$, because $E_{\mathrm{b}}(\lambda, T_{\mathrm{gas},2})$ is much higher than $E_{\mathrm{b}}(\lambda, T_{\mathrm{bg}})$. It is because temperature of the background parts are controlled at relatively lower temperature by the engine coolant. With assumption of zero reflectivity, $\tau_{\mathrm{gas,j}}$ is equal to $1 - \epsilon_{\mathrm{gas,j}}$, then the normalized mean gas intensity of the mixed zone ($\tilde{U}_{\mathrm{gas},1}$) becomes

the half of $\tilde{U}_1$, since the soot emissivity of the background parts is very high ($\simeq 1$) due to high soot accumulation on these parts.

Relationship between the normalized mean gas intensity ($\tilde{U}_{\text{gas},1}$, $\tilde{U}_{\text{gas},2}$) and mean temperature ($T_{\text{gas},1}$, $T_{\text{gas},2}$) of two zones can be identified by an empirical approximation method, instead of direct employment (2.31). In this paper, the following situ-Plank function is applied [67].

$$T_{\text{gas,j}} = \frac{A_1}{\ln(\frac{A_2}{\tilde{U}_{\text{gas,j}}} + A_3)} \tag{2.32}$$

To identify parameters in (2.32), temperature ($T_{\text{gas},2}$, T_{piston}) and intensity ($\tilde{U}_{\text{gas},2}$, $\tilde{U}_{\text{piston}}$) are used. The mean temperature of the cylinder volume system from GT-power simulation before intake flow begins is used as $T_{\text{gas},2}$. From Sec. 2.3.1, it is reminded that η does not affect the unmixed zone temperature. The piston temperature is assumed to be equal (or almost same) with the cylinder wall temperature of 400 K. With these sample data, the situ-Plank function is identified using nonlinear fitting curve method.

The mixed zone temperature is estimated by applying ($\tilde{U}_{\text{gas},1}$) into (2.32). In Fig. 2.6, mixed zone temperature is simulated with the different mixing parameters (η). To have the best agreement between the model temperature and the estimated temperature of the mixed zone, η is calibrated. With best tuned η of 8, the model and estimated temperature of two zones are shown in Fig. 2.11. A good level of agreements between them are achieved.

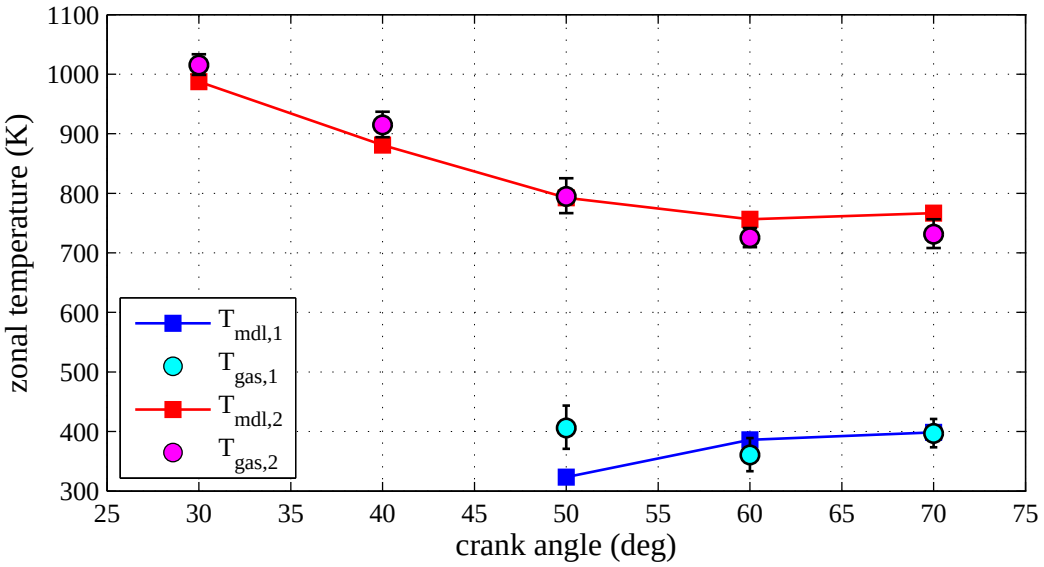

Figure 2.11: Zonal temperature comparison between the model and the estimate: mixed zone model(blue square), mixed zone estimate(light blue circle), unmixed zone model(red square), unmixed zone estimate(magenta circle).

2.4 Simulation Study

With the parameters calibrated (C_{d}, α, η), comparative simulation studies are conducted to investigate the effect of different variable valve actuation schemes on charge mixing.

2.4.1 Intake Valve Timing Shift

The shifting effect of intake valve timing is investigated. There are two intake valves, and they share the identical timings. Intake valve timings with shifting $\pm$ 10 CAD are shown in Fig. 2.12(a). For three cases, same initial conditions of temperature, mass, and pressure at -200 CAD are used. From Fig. 2.12(a) and (b), it is observed that 10 CAD retard of intake valve timing promotes mixing of fresh charge and residual gas. It is due to a strong intake flow of high kinetic energy as phasing of intake valve timing. As a result, fresh charge gets more thermal energy from residual gas. However, since retarding intake valve timing makes unmixed zone temperature reduced, particularly

when substantial residual gas is transferred to the mixed zone (60-100 CAD), the effect of retarding intake valve timing is limited. Also, the intake valve should be closed before BDC or slightly after BDC to avoid loss of intake charge.

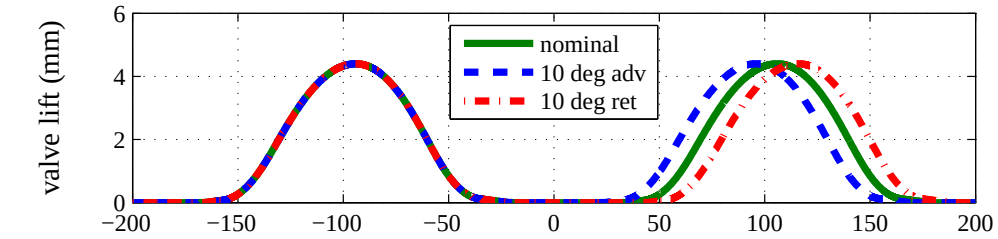

(a)

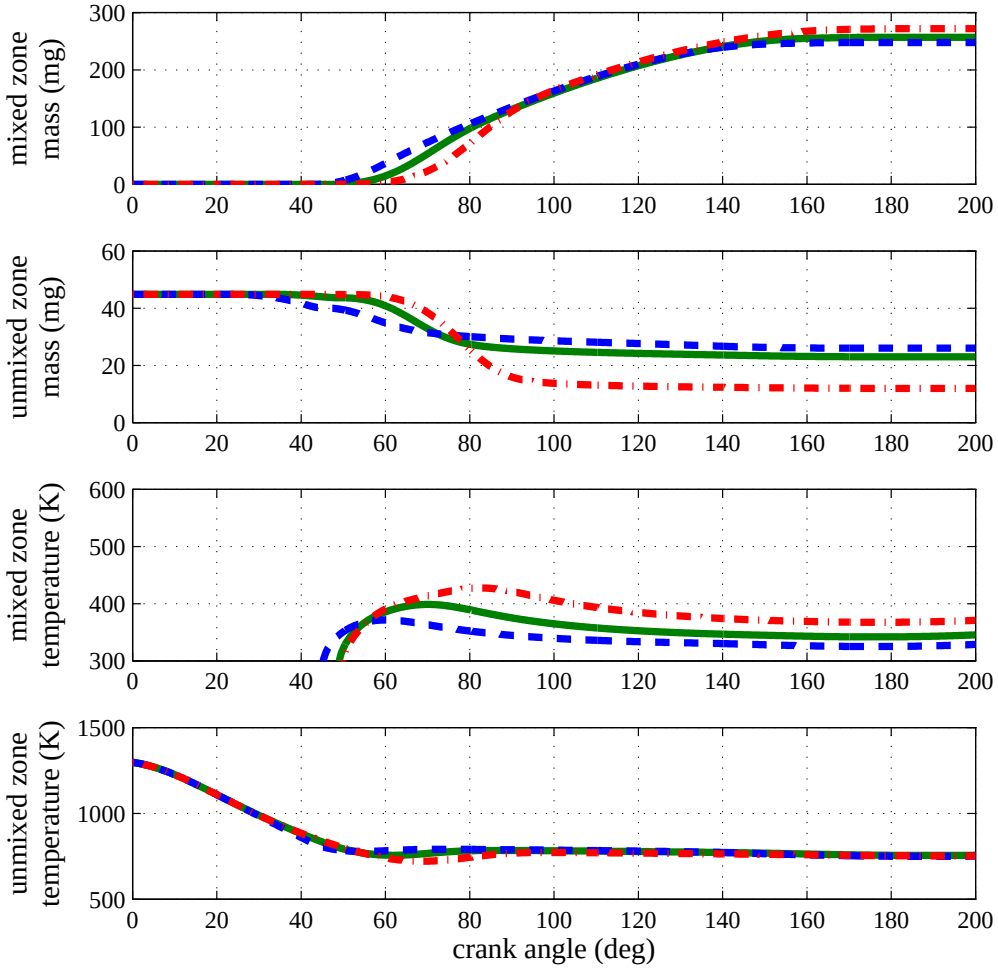

(b)

Figure 2.12: Intake valve timing shift: (a) valve profile (b) zonal mass and temperature. Nominal case(solid green), 10 CAD advance(dashed blue), 10 CAD retard(dashed-and-dotted red).

2.4.2 Exhaust Valve Timing Shift

Similarly, phasing effect of exhaust valve timing on two zones is investigated under identical initial conditions. Exhaust valve timings with phasing of $\pm$ 10 CAD are shown in Fig. 2.12(a). From Fig. 2.12(b) and (c), it is observed that 10 CAD retard of exhaust valve timing enhances mixing of fresh charge and residual gas. It is because the decreased pressure in a cylinder generates strong intake flow of high kinetic energy. However, since mass and temperature of retained residual gas at IVO are reduced by retard of exhaust valve timing, retard angle is limited.

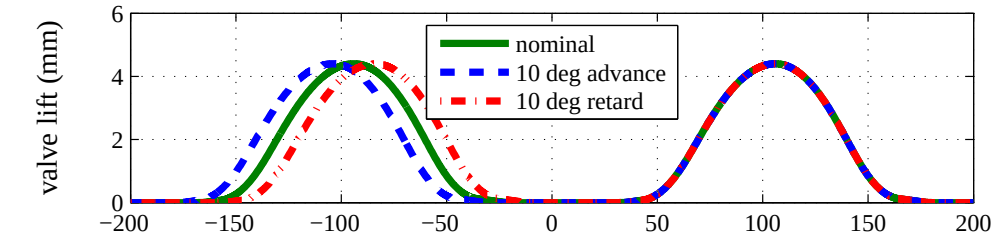

(a)

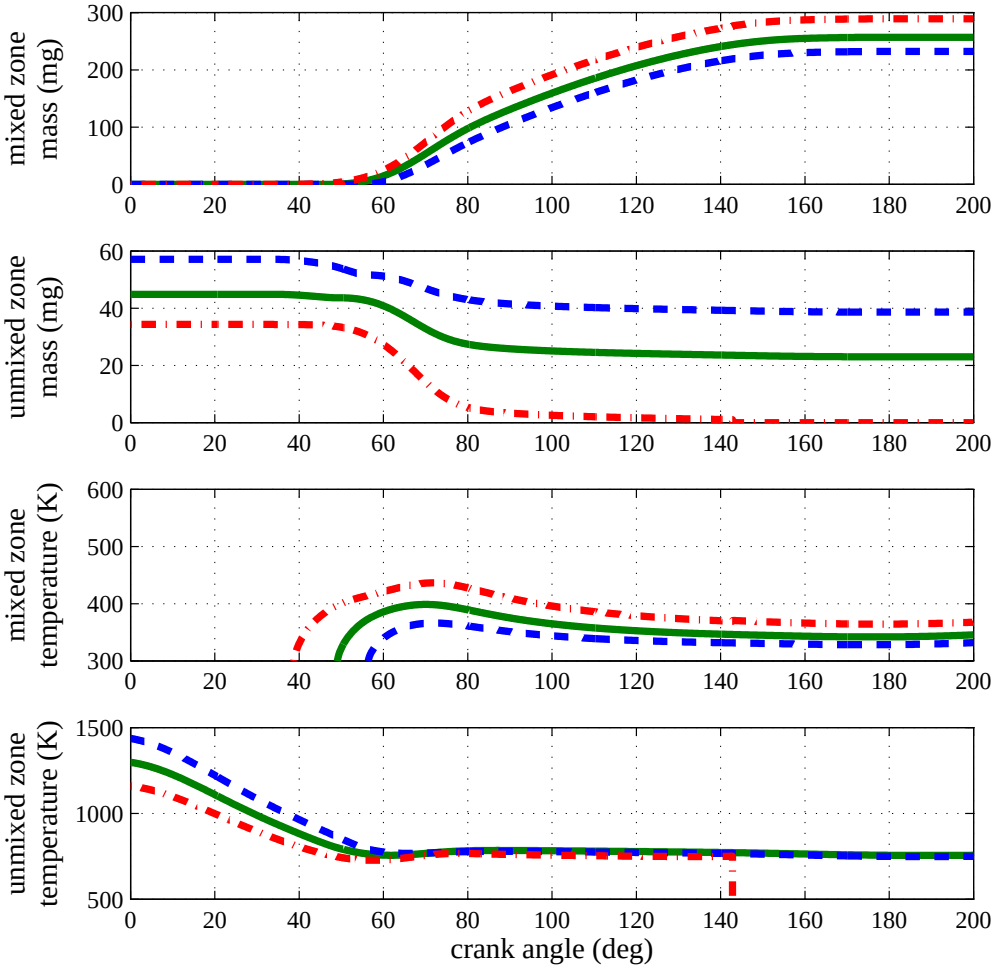

(b)

Figure 2.13: Exhaust valve timing shift: (a)valve profile (b)zonal mass and temperature. Nominal case(solid green), 10 CAD advance(dashed blue), 10 CAD retard(dashed-and-dotted red).

2.4.3 Synchronous vs Asynchronous Intake Valve Timing

In this section, influence of synchronous and asynchronous intake valve timings on two zones is investigated. Study on effect of independent intake valve control [24] motivates this comparative analysis. Fig. 2.14(a) shows the valve timings used. Valve timings for one of two intake valves is shared, but the other is different. With asynchronous intake valve timing, better mixing is achieved (the less mass of the unmixed zone at IVC), as a consequence, fresh charge in the mixed zone gets more thermal energy from the transferred residual gas. In comparison with 10 CAD retard of intake valve timing, asynchronous intake valve timing enables making up for thermal loss due to reduced residual gas temperature by acceleration of charge mixing. Therefore, asynchronous valve strategy is a practical alternative of retarding intake valve timing. Simulation studies reveal significance of the developed model in analyzing the effect of the planned variable valve actuation scheme.

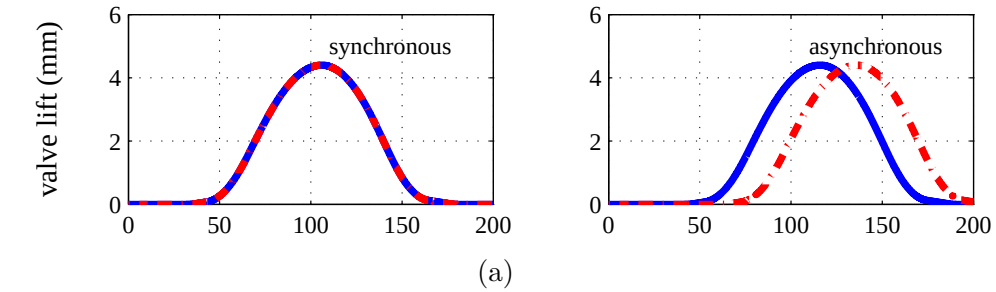

(a)

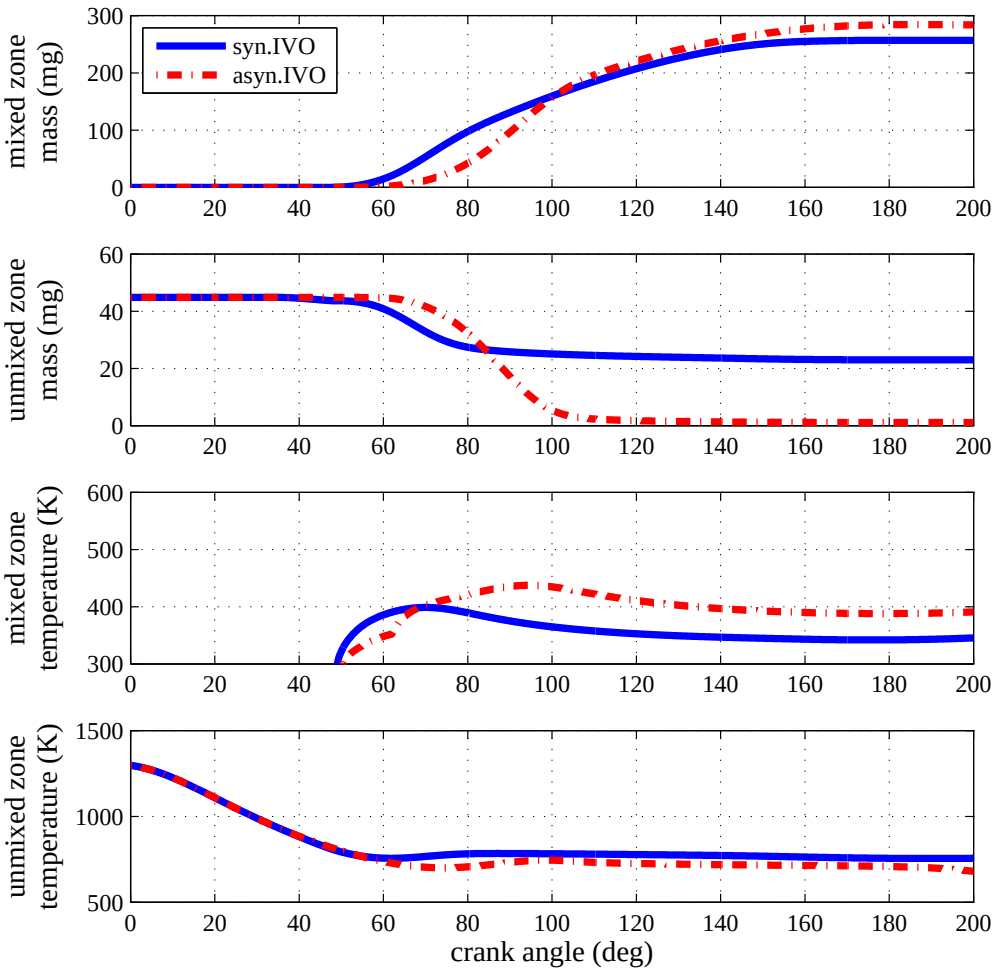

(b)

Figure 2.14: Synchronous vs Asynchronous intake valve timing: (a) synchronous (left) and asynchronous (right) intake valve timings (b) zonal mass and temperature - synchronous (solid blue) and asynchronous (dashed-and-dotted red) valve timings.

2.5 Conclusion

A two-zone charge mixing model is developed to describe interaction between fresh charge and residual gas for the purpose of control design. The cylinder volume is divided into two zones according to mixing degrees. The mixed zone is filled with the fresh charge and the transferred residual gas. The unmixed zone consists of the rest of the residual gas. The model shows a reduced computational burden for the simple description of mixing process while capturing the critical physics. Effectiveness of the developed model is shown through the optical engine test and the GT-power simulation. With the optical engine test, the infrared images are taken to observe the mixing process optically. The images are segmented into two zones according to the mean intensity of pixels by applying the k-means cluster method. Then, the mean temperature of two zones are estimated. From comparison between the model and the estimates, the developed two-zone charge mixing model turns out to be useful for the simple description of complex mixing process. In addition, the model reveals significance in planning the valve actuation schemes from comparative simulation studies.

Chapter 3

Frequency Domain Model of An Electrohydraulic Actuator

In this chapter, a frequency domain model, referred to as a generalized frequency response function (GFRF), of an electrohydraulic actuator is developed. For a linear system, spectral analysis using a frequency response function (FRF), which is a transfer function in frequency domain, offers great insight into system dynamics and controls. The objective of this chapter is to extend such benefits to the nonlinear electrohydraulic actuator. Two different approaches are investigated. First, an analytic frequency domain model is derived from physical dynamics of the electrohydraulic actuator. Second, an experimental frequency domain model is identified from frequency response. Frequency domain models reveal great significance on system analysis and identification. The results of this chapter are reported in [41, 68, 69].

3.1 Introduction

3.1.1 Background

Given the high power density, large force capacity, and mechanical flexibility over other actuation systems, an electrohydraulic actuator has been used in a broad range of applications: construction machinery, agriculture equipment, manufacturing machines, industrial robots, aerospace actuators, and automotive actuators [70, 71, 72, 73, 74,

75]. However, inherent nonlinear dynamic features of the electrohydraulic actuator have complicated its practical use as a precise actuator. Therefore, modeling, analysis and controls of the electrohydraulic actuator have been actively studied over the past decades. Among them, modeling and analysis of the electrohydraulic actuator are main interests of this chapter.

For the purpose of control design, the linear model of the electrohydraulic actuator in the vicinity of the equilibrium was developed while regarding nonlinearities as uncertainties [76, 77, 78, 79]. A beauty of the linear model is spectral analysis using a frequency response function (FRF), since it offers a physical interpretation of a system and a great tool for system identification and control design in frequency domain. However, since the electrohydraulic actuator includes nonlinear dynamics, the linear model cannot capture all the critical features.

As quasi-linearization, the describing function method was employed to develop a transfer function depending on input amplitude [80, 81]. But, it cannot retain frequency interference of a nonlinear system such as harmonics and intermodulation [30, 31]. Such features are shown in Fig. 3.1. Although the single frequency input signal which ranges from 1 to 100 Hz (x-axis in the figure) is applied, much more frequency contents are involved in the output. In the figure, up to five times $(0 - 5\omega)$ of the input frequency (ω) are shown.

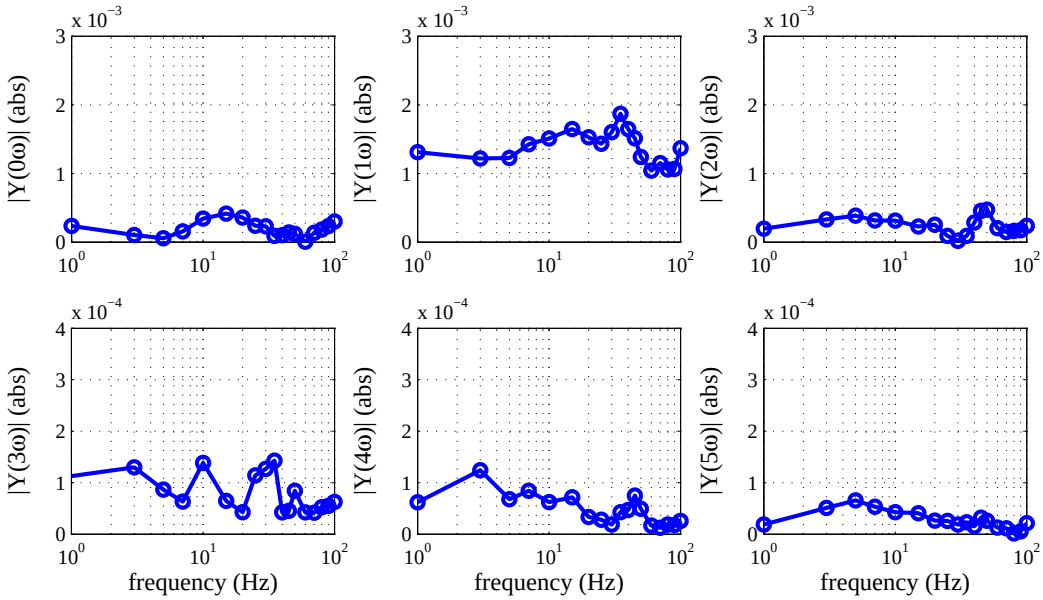

Figure 3.1: Output discrete Fourier transforms (DFT) of single frequency response: the output possesses more frequency contents than the input.

To improve model accuracy, the nonlinear models were used. The essential nonlinear factor is the orifice flow rate which is proportional to the orifice area and the square root of the pressure drop. Another factor is the friction force, such as stiction and Coulomb friction, exerting on the contact surfaces of the spool and the piston. These nonlinearities were taken into account for modeling, parameter estimation and nonlinear control design in [32, 33, 34, 35]. One of the drawbacks of a nonlinear model is the absence of universal analysis tool except numerical simulation using a computational machine. Such a technical difficulty motivates the need of informative spectral analysis for studying dynamic features of a nonlinear system.

For a wide class of nonlinear systems, input/output relationship can be represented by convergent Volterra series. Volterra series is a functional expansion of a nonlinear system with a kernel in time domain. Since theoretical foundations were established [82, 83, 84, 85, 86], Volterra series has been extensively studied for spectral analysis of nonlinear systems [87, 88]. The GFRF is the multivariable Fourier transform of the kernel. Provided the GFRF is available, the output spectrum, i.e. the output Fourier

transform, can be computed analytically. In spite of such utility in spectral analysis, few applications to actual mechanical systems have been made due to its complex derivation [89]. For the purpose of fault detection and parametric identification, Volterra series in time domain was employed to describe the electrohydraulic actuator [90, 91], but spectral analysis using the GFRF has not been given yet.

In this paper, the GFRFs of the electrohydraulic system are derived in two approaches. In the first approach, motivated by [84, 89], the GFRF is analytically derived from physical dynamics of the electrohydraulic actuator. Because of the explicit connection with the physical parameters, the analytic GFRFs are represented by the physical parameters. In the second approach, the GFRFs are experimentally identified with the assumption of block-oriented nonlinear systems including the Wiener- and Hammerstein models. Frequency domain identification of these models has been actively studied for their broad application to complex and undetermined systems [36, 37, 38]. In this chapter, further improvement from the former work by the author [41] is made for efficient and consistent identification of the block-oriented nonlinear systems.

By applying the GFRFs, the output spectrum is analytically computed and analyzed to explore the nonlinear dynamic features of the electrohydraulic actuator in frequency domain. First, spectral analysis with the analytic GFRF reveals that the nonlinear dynamic behavior of the electrohydraulic actuator is dominant near the resonance frequency. And the effect of the input amplitude on the output spectrum is investigated with respect to the working range of state variables. Second, the output spectrum of the electrohydraulic actuator is computed using the experimental GFRFs, and it shows acceptable levels of agreements with the measurements. It turns out that the Wiener model is better suited than the Hammerstein model to describe the given electrohydraulic actuator. In addition, spectral analysis offers a versatile tool for control design of the electrohydraulic system in frequency domain and this will be presented in the next chapter.

3.1.2 Problem Formulation

The problems to be solved are shown in Fig. 3.2. In the analytic approach, physical dynamics in time domain is given. Whereas, in the experimental approach, the Fourier

transforms of input and output are available (computed using input/output measurements). The goal of two approaches is commonly to find the GFRFs which characterize the input/output relationship in frequency domain.

	Given	Goal
analytic approach	$dx(t)/dt=f(x(t),u(t))$ $y(t)=h(x(t),u(t))$	$H_n(j\omega_1,\ldots,j\omega_n)$
experimental approach	$U(j\omega)$, $Y(j\omega)$	

Figure 3.2: Two approaches for frequency domain model derivation: analytic and experimental.

3.1.3 Outline

The rest of the chapter is organized as follows: In Sec. 3.2, mathematical preliminaries for this chapter are briefly introduced. In Sec. 3.3, the analytic frequency domain model is derived from physical dynamics and spectral analysis with the analytic model is conducted. In Sec. 3.4, the experimental frequency domain is identified based on spectral analysis with the assumption of block-oriented nonlinear systems. The concluding remarks are drawn in Sec. 3.5.

3.2 Mathematical Preliminaries

Theoretical background for this chapter is briefly introduced in this section. It includes the generalized frequency response functions (GFRFs), the Kronecker product, and the growing exponential method. They are well documented in [84].

3.2.1 Generalized Frequency Response Function (GFRF)

Input/output representation of a nonlinear system can be described by Volterra series such as

$$y(t) = \sum_{n=1}^{N} y_n(t) \tag{3.1}$$

$$y_n(t) = \int_{-\infty}^{\infty} \cdots \int_{-\infty}^{\infty} h_n(\tau_1, \cdots, \tau_n) \prod_{i=1}^{n} u(t-\tau_i) d\tau_i, \tag{3.2}$$

where $u(t) \in \Re$, $y(t) \in \Re$ and $h_n(\tau_1, \cdots, \tau_n) : \Re^n \to \Re$ are the input, the output and the nth order Volterra kernel, respectively. As can be seen from above multidimensional convolution, the Volterra kernel is the counterpart of the impulse response function for a linear system.

Applying (multivariable) Fourier transform to the output and the Volterra kernel yields the output spectrum and the nth order GFRF:

$$Y_n(\mathrm{j}\omega) = \int_{-\infty}^{\infty} y_n(\tau) \mathrm{e}^{-\mathrm{j}\omega\tau} d\tau \tag{3.3}$$

$$H_n(\mathrm{j}\omega_1, \cdots, \mathrm{j}\omega_n) = \int_{-\infty}^{\infty} \cdots \int_{-\infty}^{\infty} h_n(\tau_1, \cdots, \tau_n) \prod_{i=1}^{n} \mathrm{e}^{-\mathrm{j}\omega_i\tau_i} d\tau_i \tag{3.4}$$

It is noted that symmetric GFRFs of which all permutations are identical are considered only for uniqueness without explicit notice hereafter [84]. Multivariable Fourier transform is the generalization of Fourier transform from single-frequency domain to multi-frequency domain. Similarly, the GFRF is the counterpart of the FRF of a linear system. The output and the nth order Volterra kernel can be rewritten by inverse transform:

$$y_n(t) = \frac{1}{2\pi} \int_{-\infty}^{\infty} Y_n(\mathrm{j}\omega) \mathrm{e}^{\mathrm{j}\omega t} d\omega \tag{3.5}$$

$$h_n(\tau_1, \cdots, \tau_n) = \frac{1}{(2\pi)^n} \int_{-\infty}^{\infty} \cdots \int_{-\infty}^{\infty} H_n(\mathrm{j}\omega_1, \cdots, \mathrm{j}\omega_n) \prod_{i=1}^{n} \mathrm{e}^{\mathrm{j}\omega_i\tau_i} d\omega_i \tag{3.6}$$

Substituting (3.6) into (3.2), then reordering integrals yields

$$y_n(t) = \frac{1}{(2\pi)^n} \int_{-\infty}^{\infty} \cdots \int_{-\infty}^{\infty} H_n(\mathrm{j}\omega_1, \cdots, \mathrm{j}\omega_n) \prod_{i=1}^{n} U(\mathrm{j}\omega_i) \mathrm{e}^{\mathrm{j}\omega_i t} d\omega_i \tag{3.7}$$

$U(\cdot)$ is the input spectrum defined similarly with the output spectrum. Then, by equating (3.5) and (3.7) and by denoting $\omega = \omega_1 + \cdots + \omega_n \geq 0$, the output spectrum can be computed from the input spectrum and the GFRFs such as

$$Y_n(\mathrm{j}\omega) = \frac{1}{(2\pi)^{n-1}} \int\limits_{\omega=\omega_1+\cdots+\omega_n} H_n(\mathrm{j}\omega_1, \cdots, \mathrm{j}\omega_n) U(\mathrm{j}\omega_1) \cdots U(\mathrm{j}\omega_n) d\omega_1 \cdots d\omega_{n-1} \quad (3.8)$$

$$Y(\mathrm{j}\omega) = \sum_{n=1}^{N} Y_n(\mathrm{j}\omega) \quad (3.9)$$

With the single frequency input: $u(t) = A\sin(\omega_\mathrm{o} t + \theta)$, where A is amplitude, ω_o is the frequency and θ is the phase angle, using (3.8) and (3.9), the output spectrum is given by

$$Y_n(\mathrm{j}\omega) = \frac{1}{2^{n-1}} \sum_{\omega_{k_1}+\cdots+\omega_{k_n}=\omega} H_n(\mathrm{j}\omega_{k_1}, \cdots, \mathrm{j}\omega_{k_n}) U(\mathrm{j}\omega_{k_1}) U(\mathrm{j}\omega_{k_2}) \cdots U(\mathrm{j}\omega_{k_n}) \quad (3.10)$$

$$Y(\mathrm{j}\omega) = \sum_{n=1}^{N} Y_n(\mathrm{j}\omega), \quad (3.11)$$

where $\omega_{k_i} \in \{+\omega_\mathrm{o}, -\omega_\mathrm{o}\}$ for $i \in \{1, \cdots, n\}$. $U(-\mathrm{j}\omega_{k_i})$ is a complex conjugate of $U(\mathrm{j}\omega_{k_i})$. Nonnegative ω is the output frequency which is not necessarily same with the input frequency ω_o. It is noted that spectral analysis with steady-state data is available for a stable system in the sense of bounded input and bounded output (BIBO). In other words, the magnitude of the GFRFs should be bounded to yield bounded output spectrum [92].

From (3.10) and (3.11), provided GFRFs and input spectrum of a stable nonlinear system are available, output spectrum can be computed analytically (analytic approach). Or provided input- and output spectrum of a stable nonlinear system are available, GFRFs can be experimentally estimated (experimental approach).

3.2.2 Kronecker Product

For matrices $A \in \Re^{n_a \times m_a}$ and $B \in \Re^{n_b \times m_b}$ whose elements are a_{ij} and b_{ij}, the *Kronecker product* is defined by

$$A \otimes B = \begin{bmatrix} a_{11}B & \cdots & a_{1m_a}B \\ \vdots & \vdots & \vdots \\ a_{n_a1}B & \cdots & a_{n_am_a}B \end{bmatrix} \quad (3.12)$$

Its dimension is $n_a n_b m_a m_b$, and the following equations are satisfied:

$$(A+B)\otimes(C+D) = A\otimes B + A\otimes D + B\otimes C + B\otimes D \tag{3.13}$$

$$(AB)\otimes(CD) = A\otimes CB\otimes D \tag{3.14}$$

It is noted that the Kronecker product has a higher precedence than matrix addition and multiplication.

The Kronecker product is used to represent multivariable Taylor series of a vector function. For example, the multivariable Taylor series of $f(x):\Re^n\to\Re^m$ at the origin is given by

$$f(x) \approx F_0 + F_1 x + F_2 x\otimes x + F_3 x\otimes x + \cdots, \tag{3.15}$$

where a dimension of F_i for $i=1,2,3,\cdots$ is mn^i. For a simple notation, $x^{(i)} = x\otimes\cdots\otimes x$ of i terms will be used.

For a vector, for example $x = [\ x_1\ \ x_2\ \ x_3\ ]$, then

$$x^{(2)} = [\ x_1^2\ \ x_1x_2\ \ x_1x_3\ \ x_2x_1\ \ x_2^2\ \ x_2x_3\ \ x_3x_1\ \ x_3x_2\ \ x_3^2\ ] \tag{3.16}$$

As can be seen from (3.16), though the Kronecker product is redundant, this will be used in the following section for explicit derivation.

3.2.3 Growing Exponential Method

The growing exponential method will be used to compute GFRFs from physical dynamics. Here, a general nonlinear form in the form of

$$\dot{x}(t) = Ax(t) + Dx(t)u(t) + Bu(t) \tag{3.17}$$

$$y(t) = Cx(t) \tag{3.18}$$

is regarded with appropriate dimensions. If up to the second order GFRFs are of interest, let us define the exponential input given by

$$u(t) = \mathrm{e}^{s_1 t} + \mathrm{e}^{s_2 t}, \tag{3.19}$$

for $s_1, s_2 > 0$ and assume that

$$x(t) = G_{1,0}\mathrm{e}^{s_1 t} + G_{0,1}\mathrm{e}^{s_2 t} + G_{1,1}\mathrm{e}^{(s_1+s_2)t} + \cdots \tag{3.20}$$

Substituting (3.19) and (3.20) into (3.17) and (3.18) and equating same exponential gives

$$H_1(s) = C(sI - A)^{-1}B \tag{3.21}$$

$$H_2(s_1, s_2) = C((s_1 + s_2)I - A)^{-1}D((s_1I - A)^{-1} + (s_2I - A)^{-1})B \tag{3.22}$$

In (3.21), s is used instead of s_1 for the simple notation. For uniqueness, the symmetric GFRF is considered only such as $H_{2sym}(s_1, s_2) = \frac{1}{2}C((s_1+s_2)I-A)^{-1}D((s_1I-A)^{-1} + (s_2I-A)^{-1})B$. Replacing s_i with $\mathrm{j}\omega_i$ yields a final form of GFRFs used in this chapter.

3.3 Analytic Nonlinear Frequency Domain Model

3.3.1 GFRFs Derivation

In this section, GFRFs of an electrohydraulic actuator are analytically derived from physical dynamics with the three steps: 1) physical model development, 2) augmentation through Carleman bilinearization, 3) GFRFs derivation by applying the growing exponential method.

Physical Dynamics

Fig. 3.3 depicts the schematics of the electrohydraulic actuator for camless engine valve actuation which is concerned in the thesis. $x_{\mathrm{p}}(t)$, $p_{\mathrm{c}}(t)$ and $x_{\mathrm{s}}(t)$ indicate the piston position, the cylinder pressure and the spool position, respectively. The sign conventions of $x_{\mathrm{p}}(t)$ and $x_{\mathrm{s}}(t)$ are shown in the figure. $q_{\mathrm{c}}(t)$ is the orifice flow rate and $i(t)$ is the solenoid current. p_{s} and p_{r} are the supply and return pressure, respectively. The whole system consists of three main components: hydraulic pump; spool valve; piston. The pump supplies high pressure oil. The spool valve is of a three-way type and it is assumed to be critically centered [77]. The spool is controlled by the voice coil motor and it controls hydraulic flow to actuate the piston. Thereby, the piston operates the poppet valve. This type of structure is quite common in many electrohydraulic applications.

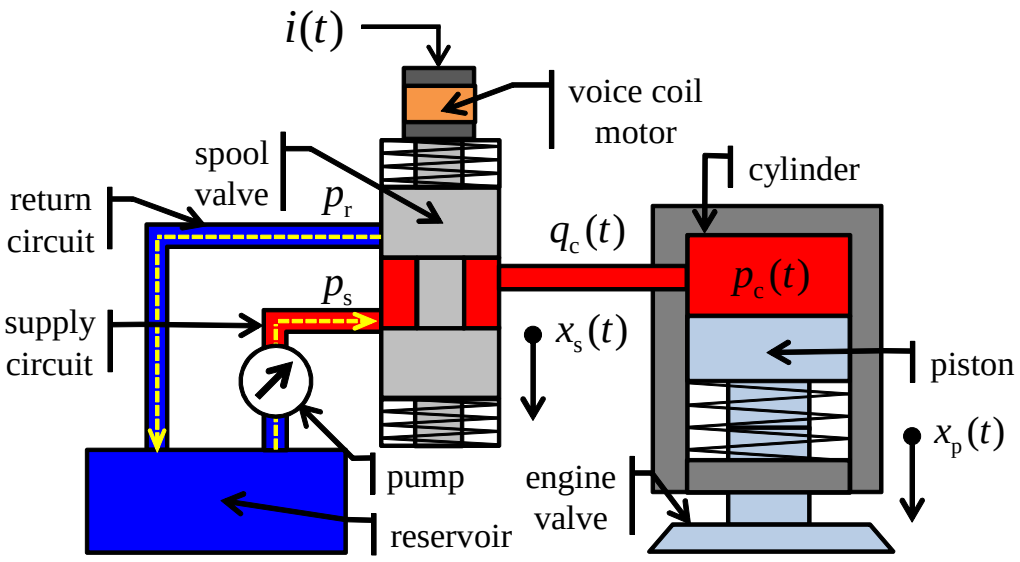

Figure 3.3: Schematics of the electrohydraulic camless engine valve actuator.

Physical dynamics of the electrohydraulic actuator is given by

$$\ddot{x}_{\rm p}(t) = -\frac{k_{\rm p}x_{\rm p}(t)}{m_{\rm p}} - \frac{b_{\rm p}\dot{x}_{\rm p}(t)}{m_{\rm p}} + \frac{A_{\rm c}p_{\rm c}(t)}{m_{\rm p}} - \frac{F_{\rm pre}}{m_{\rm p}} \tag{3.23}$$

$$\dot{p}_{\rm c}(t) = \frac{\beta\left(q_{\rm c}(t) - A_{\rm c}\dot{x}_{\rm p}(t)\right)}{V_{\rm c}(t)} \tag{3.24}$$

$$\ddot{x}_{\rm s}(t) = -\frac{k_{\rm s}}{m_{\rm s}}x_{\rm s}(t) - \frac{b_{\rm s}}{m_{\rm s}}\dot{x}_{\rm s}(t) + \frac{k_{\rm vcm}}{m_{\rm s}}i(t), \tag{3.25}$$

where $k_{\rm p}$, $b_{\rm p}$ and $m_{\rm p}$ denote the spring constant, the viscous damping coefficient and the lumped mass of the piston and the poppet valve. For the spool, $k_{\rm s}$, $b_{\rm s}$ and $m_{\rm s}$ are similarly defined. $A_{\rm c}$ is the cross section area of the hydraulic cylinder. $k_{\rm vcm}$ is the magnetic force sensitivity of the voice coil motor. Since the piston and the poppet valve are not physically connected, the poppet valve is heavily preloaded by the spring ($F_{\rm pre}$) for continuous contact with the piston [79, 93]. β is the bulk modulus of the oil. $V_{\rm c}(t)$ is the cylinder volume and it is assumed to be constant as $V_{\rm co}$ because of a small range of the piston position, that is, $V_{\rm c}(t) = A_{\rm c}x_{\rm p}(t) + V_{\rm co} \approx V_{\rm co}$ [77]. The orifice flow rate is

given by

$$q_{\mathrm{c}}(t) = \begin{cases} C_{\mathrm{d}} W x_{\mathrm{s}}(t) \sqrt{\frac{2}{\rho}(p_{\mathrm{s}} - p_{\mathrm{c}}(t))}, & \text{if } x_{\mathrm{s}}(t) \geq 0 \\ C_{\mathrm{d}} W x_{\mathrm{s}}(t) \sqrt{\frac{2}{\rho}(p_{\mathrm{c}}(t) - p_{\mathrm{r}})}, & \text{if } x_{\mathrm{s}}(t) < 0 \end{cases} \tag{3.26}$$

C_{d} and W are the discharge coefficient and the area gradient of the spool valve. ρ is the oil density. The state, the input and the output of the electrohydraulic actuator are defined by

$$x(t) = [x_{\mathrm{p}}(t),\ \dot{x}_{\mathrm{p}}(t),\ p_{\mathrm{c}}(t),\ x_{\mathrm{s}}(t),\ \dot{x}_{\mathrm{s}}(t)]^T \in \Re^{5\times 1} \tag{3.27}$$

$$u(t) = i(t) \in \Re \tag{3.28}$$

$$y(t) = x_{\mathrm{p}}(t) \in \Re \tag{3.29}$$

Leakage flow and friction force can be nontrivial factors which contribute nonlinear dynamics of the electrohydraulic actuator. However, precise identification of these factors is very expensive. Besides, measurement can be limited due to space limitation. For the purpose of control or fault detection, the observers or the filters were used to estimate these factors [94, 95, 96, 97]. However, in this analytic approach such uncertain factors are not considered. The orifice equation which represents the dominant and intrinsic nonlinear dynamics of the electrohydraulic actuator is the focus of this paper.

For existence of the convergent Volterra series and convenient derivation, the physical dynamics given by (3.23)–(3.26) is revised regarding Volterra theory and the unique feature of the engine valve application.

Variable Shift The deviation from the equilibrium is defined as: $\bar{x}(t) = x(t) - x_{\mathrm{eq}}$. The equilibrium cylinder pressure is determined by the positive equilibrium piston position x_{peq} so that $p_{\mathrm{ceq}} = (k_{\mathrm{p}} x_{\mathrm{peq}} + F_{\mathrm{pre}})/A_{\mathrm{c}}$. Other equilibrium are set to zero. By variable shift, the constant input of F_{pre} is removed for algebraic convenience. The revised dynamics renders a general form of the electrohydraulic actuator as used in [77, 76, 78, 32, 33, 34, 35]

Smoothness For existence of convergent Volterra series, the physical dynamics should be smooth. Therefore, the nonsmooth orifice equation is approximated by the hyper-tangent function such as:

$$\begin{aligned}\bar{q}_{\rm c}(t) &= C_{\rm d}Wx_{\rm s}\left(\sqrt{\frac{2}{\rho}(p_{\rm seq}-\bar{p}_{\rm c}(t))}\left(\frac{1}{2}+\frac{1}{2}\tanh(kx_{\rm s})\right)\right. \\ &+ \left.\sqrt{\frac{2}{\rho}(p_{\rm req}+\bar{p}_{\rm c}(t))}\left(\frac{1}{2}-\frac{1}{2}\tanh(kx_{\rm s})\right)\right), \end{aligned} \tag{3.30}$$

where $p_{\rm seq}=p_{\rm s}-p_{\rm ceq}\geq 0$ and $p_{\rm req}=p_{\rm ceq}-p_{\rm r}\geq 0$. k is the parameter which should be determined appropriately regarding approximation accuracy and the convergent radius.

Stability As presented in Sec. 3.2, the GFRFs should be bounded at all frequencies. However, the magnitude of the first order GFRF derived from (3.23)-(3.25) is infinite at zero frequency (see [77, 76] for the linear transfer function of the electrohydraulic actuator). Therefore, the electrohydraulic actuator is stabilized by the feedback loop as shown in Fig. 3.4 [76]. Then, the solenoid current is $i(t)=k_{\rm st}(r(t)-x_{\rm p}(t))$, where $k_{\rm st}$ is the proportional control.

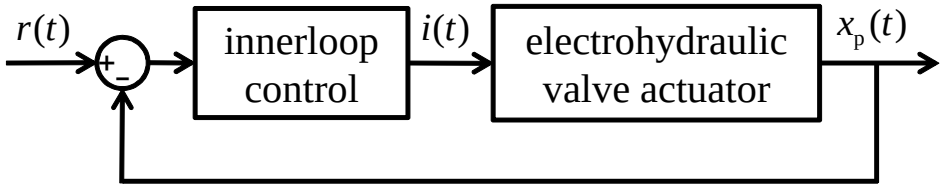

Figure 3.4: Stabilized electrohydraulic valve actuator by innerloop control.

Finally, by setting $r(t)=r_{\rm o}+\bar{r}(t)$ and $r_{\rm o}=x_{\rm peq}$, the dynamic equations of (3.12)-(3.14) are revised as

$$\ddot{\bar{x}}_{\rm p}(t) = -\frac{k_{\rm p}\bar{x}_{\rm p}(t)}{m_{\rm p}}-\frac{b_{\rm p}\dot{\bar{x}}_{\rm p}(t)}{m_{\rm p}}+\frac{A_{\rm c}\bar{p}_{\rm c}(t)}{m_{\rm p}} \tag{3.31}$$

$$\dot{\bar{p}}_{\rm c}(t) = \frac{\beta\left(\bar{q}_{\rm c}(t)-A_{\rm c}\dot{\bar{x}}_{\rm p}(t)\right)}{V_{\rm co}} \tag{3.32}$$

$$\ddot{\bar{x}}_{\rm s}(t) = -\frac{k_{\rm sv}}{m_{\rm s}}\bar{x}_{\rm p}(t)-\frac{k_{\rm s}}{m_{\rm s}}\bar{x}_{\rm s}(t)-\frac{b_{\rm s}}{m_{\rm s}}\dot{\bar{x}}_{\rm s}(t)+\frac{k_{\rm sv}}{m_{\rm s}}\bar{r}(t), \tag{3.33}$$

where $k_{\rm sv} = k_{\rm st}k_{\rm vcm}$. The new system definition is given by

$$x(t) = [\bar{x}_{\rm p}(t),\ \dot{\bar{x}}_{\rm p}(t),\ \bar{p}_{\rm c}(t),\ \bar{x}_{\rm s}(t),\ \dot{\bar{x}}_{\rm s}(t)]^T \in \Re^{5\times 1} \tag{3.34}$$

$$u(t) = \bar{r}(t) \in \Re \tag{3.35}$$

$$y(t) = \bar{x}_{\rm p}(t) \in \Re \tag{3.36}$$

Carleman Bilinearization

Eqs. (3.20)-(3.22) are approximated by multivariable Taylor series at the equilibrium point up to Nth order such as

$$\dot{x}(t) = \sum_{k=1}^{N} A_k x^{(k)}(t) + B_0 u(t) \tag{3.37}$$

$$y(t) = C_1 x(t) \tag{3.38}$$

$x^{(k)}(t)$ is the Kronecker product vector: $x^{(k)}(t) = x(t) \otimes \cdots \otimes x(t)$. A_1, B_0 and C_1 (used for the first order GFRF) are shown below:

$$A_1 = \begin{bmatrix} 0 & 1 & 0 & 0 & 0 \\ -a_{21} & -a_{22} & a_{23} & 0 & 0 \\ 0 & -a_{32} & 0 & a_{34} & 0 \\ 0 & 0 & 0 & 0 & 1 \\ -a_{51} & 0 & 0 & -a_{54} & a_{55} \end{bmatrix}, \quad B_0 = \begin{bmatrix} 0 \\ 0 \\ 0 \\ 0 \\ a_{51} \end{bmatrix}$$

$$C_1 = \begin{bmatrix} 1 & 0 & 0 & 0 & 0 \end{bmatrix}$$

The elements a_{ij} are given below:

$$a_{21} = \frac{k_{\rm p}}{m_{\rm p}}, \quad a_{22} = \frac{b_{\rm p}}{m_{\rm p}}, \quad a_{23} = \frac{A_{\rm c}}{m_{\rm p}}$$

$$a_{32} = \frac{\beta A_{\rm c}}{V_{\rm co}}, \quad a_{34} = \frac{\beta}{V_{\rm co}} C_{\rm d} W \left(\sqrt{\frac{p_{\rm seq}}{2\rho}} + \sqrt{\frac{p_{\rm req}}{2\rho}} \right)$$

$$a_{51} = \frac{k_{\rm vs}}{m_{\rm s}}, \quad a_{54} = \frac{k_{\rm s}}{m_{\rm s}}, \quad a_{55} = \frac{b_{\rm s}}{m_{\rm s}}$$

Nonzero elements of A_k for $k > 1$ is due to the orifice flow rate which is the nonlinear function of the cylinder perssure and the spool position. Matrices A_k for $k > 1$ are omitted for the limited space.

By differentiating the Kronecker product vector $x^{(j)}(t)$, the differential equation of $x^{(j)}(t)$ can be obtained such as

$$\frac{d}{dt}x^{(j)}(t) \;=\; \sum_{k=1}^{N-j+1} A_{j,k}\; x^{(k+j-1)}(t) + B_{j,0}\; x^{(j-1)}u(t), \tag{3.39}$$

where $A_{j,k}$ and $B_{j,0}$ are compuated like:

$$\begin{aligned} A_{j,k} &= A_k \otimes I_n \otimes \cdots \otimes I_n \;+\; I_n \otimes A_k \otimes \cdots \otimes I_n \qquad (3.40)\\ &+ \;\cdots + \; I_n \otimes \cdots \otimes I_n \otimes A_k \\ B_{j,0} &= B_0 \otimes I_n \otimes \cdots \otimes I_n \;+\; I_n \otimes B_0 \otimes \cdots \otimes I_n \qquad (3.41)\\ &+ \;\cdots + \; I_n \otimes \cdots \otimes I_n \otimes B_0 \end{aligned}$$

I_n is the 5×5 identity matrix. For the augmented system

$$x^{\otimes}(t)^T \;=\; \left[\; x^{(1)}(t)^T \quad x^{(2)}(t)^T \quad \cdots \quad x^{(N)}(t)^T \;\right],$$

the dynamics is also augmented in a bilinear form:

$$\begin{aligned} \frac{d}{dt}x^{\otimes}(t) &= Ax^{\otimes}(t) + Dx^{\otimes}(t)u(t) + Bu(t) \qquad (3.42)\\ y(t) &= Cx^{\otimes}(t) \qquad (3.43) \end{aligned}$$

Bilinearization matrices A, B, C and D are given below:

$$A = \begin{bmatrix} A_{1,1} & A_{1,2} & \cdots & A_{1,N} \\ 0 & A_{2,1} & \cdots & A_{2,N-1} \\ 0 & 0 & \cdots & A_{3,N-2} \\ \vdots & \vdots & \ddots & \vdots \\ 0 & 0 & \cdots & A_{N,1} \end{bmatrix} \quad , \quad D = \begin{bmatrix} 0 & 0 & \cdot & 0 & 0 \\ B_{2,0} & 0 & \cdot & 0 & 0 \\ 0 & B_{3,0} & \cdot & 0 & 0 \\ \vdots & \vdots & \ddots & \vdots & \vdots \\ 0 & 0 & \cdots & B_{N,0} & 0 \end{bmatrix}$$

$$B^T = \left[\; B_{1,0}^T \quad 0 \quad 0 \quad \cdots 0 \;\right] \quad , \quad C = \left[\; C_1 \quad 0 \quad \cdots \quad 0 \;\right]$$

Growing Exponential Method

Applying the exponential functions of an input and output into (3.42) and (3.43) and equating same exponential, the analytic GFRFs are yielded by

$$
\begin{aligned}
H_1(\mathrm{j}\omega) &= C(\mathrm{j}\omega I - A)^{-1}B && (3.44)\\
H_2(\mathrm{j}\omega_1, \mathrm{j}\omega_2) &= \frac{1}{2!}\sum_{\pi(\cdot)} C(\mathrm{j}(\omega_1+\omega_2)I - A)^{-1} && (3.45)\\
&\times\ D(\mathrm{j}\omega_1 I - A)^{-1}B\\
H_3(\mathrm{j}\omega_1, \mathrm{j}\omega_2, \mathrm{j}\omega_3) &= \frac{1}{3!}\sum_{\pi(\cdot)} C(\mathrm{j}(\omega_1+\omega_2+\omega_3)I - A)^{-1} && (3.46)\\
&\times\ D(\mathrm{j}(\omega_1+\omega_2)I - A)^{-1}D(\mathrm{j}\omega_1 I - A)^{-1}B\\
&\vdots\\
H_N(\mathrm{j}\omega_1, \cdots, \mathrm{j}\omega_N) &= \frac{1}{N!}\sum_{\pi(\cdot)} C(\mathrm{j}(\omega_1+\cdots+\omega_N)I - A)^{-1} && (3.47)\\
&\times\ D(\mathrm{j}(\omega_1+\cdots+\omega_{N-1})I - A)^{-1}\\
&\times\ \cdots\\
&\times\ D(\mathrm{j}(\omega_1+\omega_2)I - A)^{-1}D(\mathrm{j}\omega_1 I - A)^{-1}B
\end{aligned}
$$

$\sum_{\pi(\cdot)}$ indicates summation of all permutations for symmetricity of the GFRFs. Since the bilinearization matrices A, B, C and D are functions of the physical parameters of the electrohydraulic actuator, the output spectrum can be characterized by the physical parameters.

3.3.2 Spectral Analysis with Analytic Model

With the physical parameters given in Table. 3.1, the analytic GFRFs are computed up to the fourth order. Then, the output spectra are analytically calculated.

Table 3.1: Physical parameters of electrohydraulic valve actuator

symbol	value	unit	symbol	value	unit
m_{p}	0.120	kg	m_{s}	0.025	kg
b_{p}	7.5	N·s/m	b_{s}	15	N·s/m
k_{p}	20e3	N/m	k_{s}	2.5e3	N/m
A_{c}	44.18e-6	m^2	F_{pre}	75	N
V_{co}	0.5e-6	m^3	k_{vcm}	9.79	N/A
β	1200e6	Pa	C_{d}	0.6	[-]
p_{s}	3.5e6	Pa	p_{r}	0.1e6	Pa
W	5e-4	m	ρ	833	$\mathrm{kg/m}^3$

Analytic GFRFs

Fig. 3.5 shows the magnitude of GFRFs up to the third order. From Fig. 3.5 (a), the resonance of the electrohydraulic actuator is found near 25 Hz. In Fig. 3.5 (b), $H_2(\mathrm{j}\omega_1, \mathrm{j}\omega_2)$ has the largest peaks near (25 Hz, -25 Hz) and (-25 Hz, 25 Hz). Therefore, $H_2(\mathrm{j}\omega_1, \mathrm{j}\omega_2)$ has the considerable impact on the zero frequency output spectrum $Y(0)$ at the resonance frequency (see (3.10) and (3.11)). Similarly, Fig. 3.5 (c) shows that $H_3(\mathrm{j}\omega_1, \mathrm{j}\omega_2, \mathrm{j}\omega_3)$ has the largest peaks near (25 Hz, -25 Hz, 25 Hz) and (-25 Hz, 25 Hz, 25 Hz), thus its impact on the fundamental output spectrum $Y(\mathrm{j}\omega)$ is the largest at the resonance frequency.

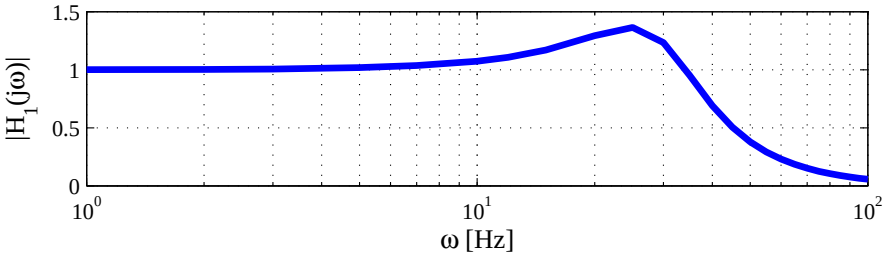

(a)

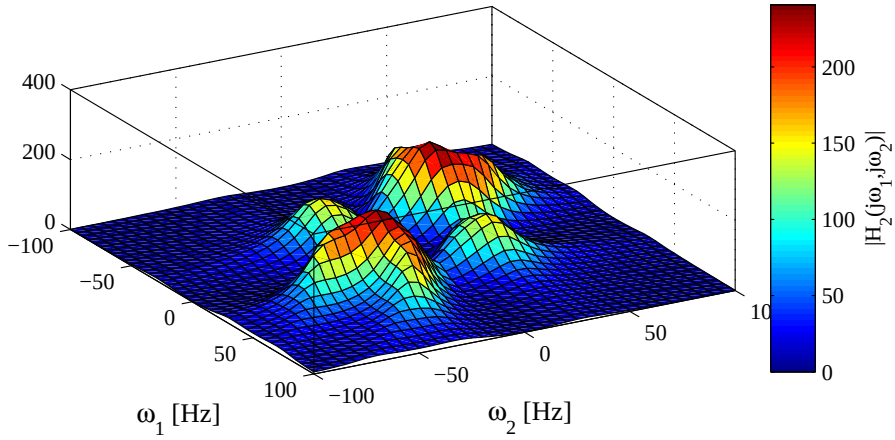

(b)

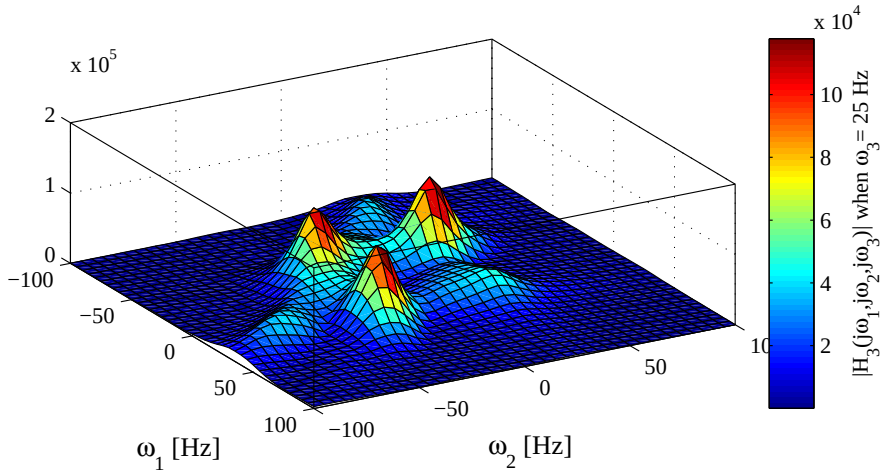

(c)

Figure 3.5: Analytic GFRFs magnitude: (a) first order $H_1(\mathrm{j}\omega)$, (b) second order $H_2(\mathrm{j}\omega_1, \mathrm{j}\omega_2)$, (c) third order $H_3(\mathrm{j}\omega_1, \mathrm{j}\omega_2, \mathrm{j}\omega_3)$

Output Spectrum

The harmonic output spectra up to the four times of the input frequency are computed using the analytic GFRFs. For comparison, simulations are carried out using the physical dynamics given by Eqs. (3.23)-(3.26). The input of $u(t) = A\sin(\omega_k t)$ ($A = 1.25$ mm and $\omega_k \in \{1, 2, \cdots, 100\}$ in Hz) is used. The discrete Fourier transform (DFT) of the simulated output are compared with the computed harmonic output spectra using the analytic GFRFs. Fig. 3.6 shows their good correspondence. As expected from Fig. 3.5 (b), the zero frequency output spectrum has the peak near the resonance frequency. Actually similar peaks are observed at all harmonics. Spectral analysis reveals that the nonlinear behavior of the electrohydraulic actuator is significant near the resonance frequency.

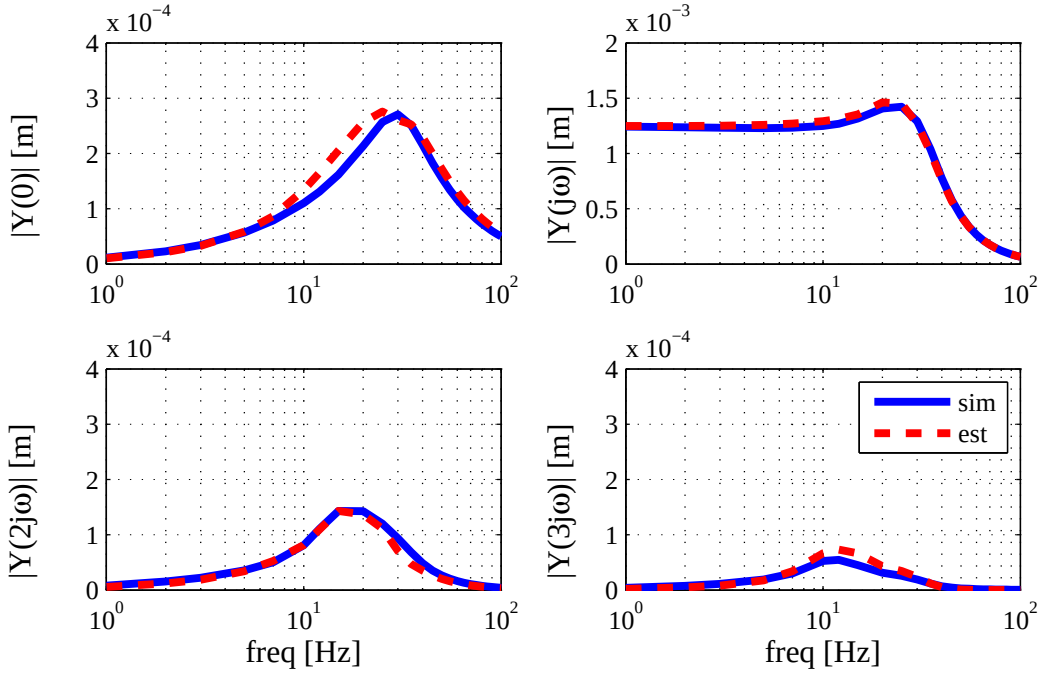

Figure 3.6: Analytic output spectrum: simulation(solid blue), estimate(dashed red).

To analyze the effect of the input amplitude on the output spectrum, the output spectra with different input amplitude are investigated. The normalized fundamental output spectra by the input amplitude are compared in Fig. 3.7. The analytic GFRFs

show good output spectrum computation for all input amplitudes. Near the resonance frequency, the normalized fundamental output spectrum becomes smaller as the input amplitude gets larger. This results from the nonlinear orifice flow rate shown in Fig. 3.8. As the input amplitude increases, the working range of the spool stroke and the cylinder pressure follows the arrows. Consequently, the orifice flow rate grows slowly. This means that the spool valve efficiency gets lower due to the increased nonlinear hydraulic damping as the working range increases. This phenomena is dominant at the resonance frequency where the working range is the largest. And such a nonlinear damping effect can be retained by the given analytic GFRFs. As discussed from Fig. 3.5 (c), the effect of $H_3(\mathrm{j}\omega_1, \mathrm{j}\omega_2, \mathrm{j}\omega_3)$ on the fundamental output spectrum is the strongest near the resonance frequency, but in negative direction.

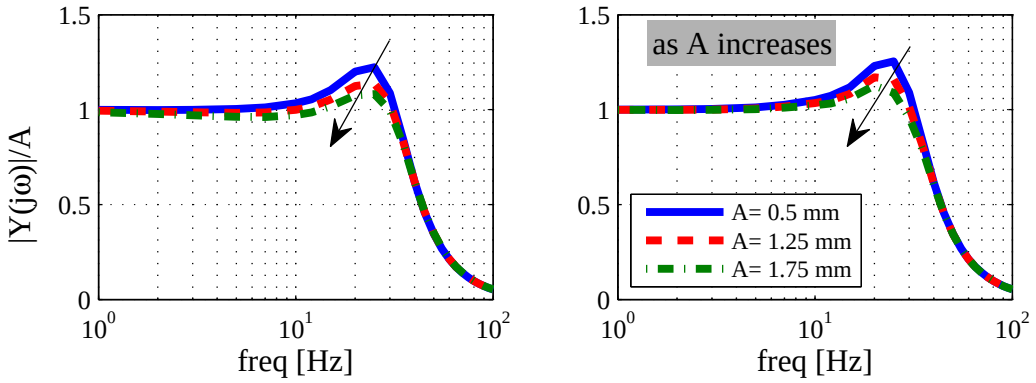

Figure 3.7: Normalized analytic output spectrum by input amplitude at fundamental frequency: simulation(left), model(right). input amplitude 0.50 mm(solid blue), input amplitude 1.25 mm(dashed red), input amplitude 1.75 mm(dashed-and-dotted green).

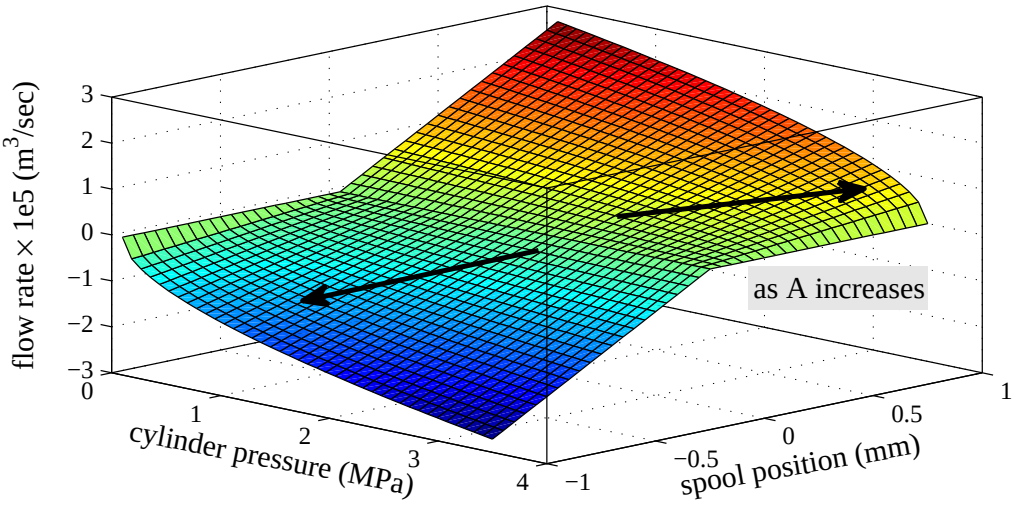

Figure 3.8: Orifice flow rate function depending on spool position and cylinder pressure: spool valve efficiency decreases as the working range increases.

3.4 Experimental Nonlinear Frequency Domain Model

In this section, the experimental GFRFs of the electrohydraulic actuator are identified from frequency response data. As done for the analytic model, first the electrohydraulic actuator is stabilized by the innerloop control. The input/output definition is same with the analytic case: $u(t) = \bar{r}(t)$, $y(t) = \bar{x}_{\mathrm{p}}(t)$. In this thesis, the block-oriented nonlinear models such as the Wiener- and the Hammerstein models are assumed for a structure of the electrohydraulic actuator without a prior knowledge about the system.

3.4.1 Model Structure

The Wiener model has a linear dynamic block which is followed by a nonlinear static block as shown in Fig. 3.9 (a). On the contrary, a static nonlinear block precedes a linear dynamic block in the Hammerstein model like Fig. 3.9 (b). $u(t)$, $x(t)$ and $y(t)$ are the input, the internal state and the output, respectively. System identification of these models are challenging because the internal state is not measurable.

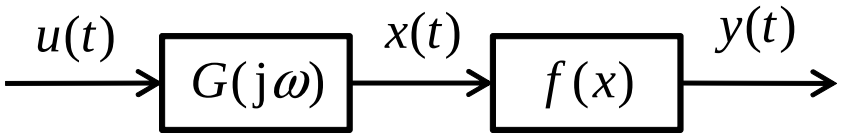

(a)

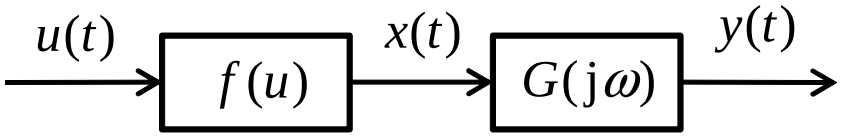

(b)

Figure 3.9: Block-oriented nonlienar systems: (a)Wiener model-linear dynamic block + nonlinear static block, (b)Hammerstein model-nonlinear static block + linear dynamic block.

For both models, the linear dynamic block and the nonlinear static block are assumed to be a stable FRF and a polynomial equation of Nth order and they are given by

$$G(\mathrm{j}\omega) = \frac{B(\mathrm{j}\omega)}{A(\mathrm{j}\omega)} = \frac{b_m(\mathrm{j}\omega)^m + b_{m-1}(\mathrm{j}\omega)^{m-1} \cdots + b_1(\mathrm{j}\omega) + b_0}{(\mathrm{j}\omega)^n + a_{n-1}(\mathrm{j}\omega)^{n-1} + \cdots + a_1(\mathrm{j}\omega) + a_0} \tag{3.48}$$

$$f(x) = c_1 x(t) + c_2 x(t)^2 + \cdots + c_N x(t)^N, \tag{3.49}$$

where $n \geq m$ for causality. $\mathtt{P} = [a_0, \cdots, a_{n-1}; b_0, \cdots, b_m]$ and $\mathtt{Q} = [c_1, \cdots, c_N]$ are the real model parameters of the linear dynamic block and the nonlinear static block, respectively. By applying the growing exponential method, the GFRFs of the Wiener- and the Hammerstein models are given by (in order) [38]

$$H_n(\mathrm{j}\omega_1, \cdots, \mathrm{j}\omega_n) = c_n G(\mathrm{j}\omega_1) \cdots G(\mathrm{j}\omega_n) \tag{3.50}$$

$$H_n(\mathrm{j}\omega_1, \cdots, \mathrm{j}\omega_n) = c_n G(\mathrm{j}\omega_1 + \cdots + \mathrm{j}\omega_n) \tag{3.51}$$

Therefore, parameter estimation of $\mathtt{P}$ and $\mathtt{Q}$ replaces identification of the experimental GFRFs of the electrohydraulic actuator.

3.4.2 Parameter Estimation

Let the electrohydraulic actuator be excited by the input:

$$u(t) = A \sin(\omega_k t + \theta), \qquad k \in \{1, \cdots, q\} \tag{3.52}$$

By substituting (3.50) and (3.51) into (3.10) and (3.11), the harmonic output spectra up to four times of the input frequency can be analytically computed: (3.53)-(3.57) for the Wiener model; (3.58)-(3.62) for the Hammerstein model. Here, the GFRFs up to the fourth order are concerned and other higher order terms are omitted.

$$
\begin{aligned}
Y(0) &= c_2||G(\mathrm{j}\omega_k)||^2||U(\mathrm{j}\omega_k)||^2 + \frac{3c_4}{4}||G(\mathrm{j}\omega_k)||^4||U(\mathrm{j}\omega_k)^2||^4 && (3.53)\\
Y(\mathrm{j}\omega_k) &= c_1 G(\mathrm{j}\omega_k)U(\mathrm{j}\omega_k) + \frac{3c_3}{4}||G(\mathrm{j}\omega_k)||^2 G(\mathrm{j}\omega_k)||U(\mathrm{j}\omega_k)||^2 U(\mathrm{j}\omega_k) && (3.54)\\
Y(2\mathrm{j}\omega_k) &= \frac{c_2}{2}G(\mathrm{j}\omega_k)^2U(\mathrm{j}\omega_k)^2 + \frac{c_4}{2}||G(\mathrm{j}\omega_k)||^2 G(\mathrm{j}\omega_k)^2||U(\mathrm{j}\omega_k)||^2 U(\mathrm{j}\omega_k)^2 && (3.55)\\
Y(3\mathrm{j}\omega_k) &= \frac{c_3}{4}G(\mathrm{j}\omega_k)^3U(\mathrm{j}\omega_k)^3 && (3.56)\\
Y(4\mathrm{j}\omega_k) &= \frac{c_4}{8}G(\mathrm{j}\omega_k)^4U(\mathrm{j}\omega_k)^4 && (3.57)
\end{aligned}
$$

$$
\begin{aligned}
Y(0) &= c_2 G(0)||U(\mathrm{j}\omega_k)||^2 + \frac{3c_4}{4}G(0)||U(\mathrm{j}\omega_k)||^4 && (3.58)\\
Y(\mathrm{j}\omega_k) &= c_1 G(\mathrm{j}\omega_k)U(\mathrm{j}\omega_k) + \frac{3c_3}{4}G(\mathrm{j}\omega_k)||U(\mathrm{j}\omega_k)||^2 U(\mathrm{j}\omega_k) && (3.59)\\
Y(2\mathrm{j}\omega_k) &= \frac{c_2}{2}G(2\mathrm{j}\omega_k)U(\mathrm{j}\omega_k)^2 + \frac{c_4}{2}G(2\mathrm{j}\omega_k)||U(\mathrm{j}\omega_k)||^2 U(\mathrm{j}\omega_k)^2 && (3.60)\\
Y(3\mathrm{j}\omega_k) &= \frac{c_3}{4}G(3\mathrm{j}\omega_k)U(\mathrm{j}\omega_k)^3 && (3.61)\\
Y(4\mathrm{j}\omega_k) &= \frac{c_4}{8}G(4\mathrm{j}\omega_k)U(\mathrm{j}\omega_k)^4 && (3.62)
\end{aligned}
$$

Linear Dynamic Block Estimation

The fundamental output spectra of the two models, (3.54) and (3.59), are rewritten as (in order)

$$
\begin{aligned}
Y(\mathrm{j}\omega_k) &= G(\mathrm{j}\omega_k)U(\mathrm{j}\omega_k)\left(c_1 + \frac{3c_3}{4}||G(\mathrm{j}\omega_k)||^2||U(\mathrm{j}\omega_k)||^2\right) && (3.63)\\
Y(\mathrm{j}\omega_k) &= G(\mathrm{j}\omega_k)U(\mathrm{j}\omega_k)\left(c_1 + \frac{3c_3}{4}||U(\mathrm{j}\omega_k)||^2\right) && (3.64)
\end{aligned}
$$

Since all terms in the brackets are real, the phase angles of the linear dynamic blocks for both models are same and given by

$$
\phi(\omega_k) = \angle Y(\mathrm{j}\omega_k) - \angle U(\mathrm{j}\omega_k) \qquad (3.65)
$$

The linear dynamic block parameter of P cannot be uniquely solved using the phase angle measurements only. Hence, P is additionally constrained with the monic numerator, i.e. $b_m = 1$. However, this constraint is compensated by the nonlinear static block, since any pair of $(\alpha G(\mathrm{j}\omega), f(\cdot)/\alpha)$ shows a same system gain with nonzero α for the Wiener- and the Hammerstein model.

Linear dynamic block identification is faced with finding the optimal P of the nonlinear least squares problem:

$$\arg\min_{\mathtt{P}} \sum_{k=1}^{q} \left(\hat{\phi}(\omega_k) - \phi(\omega_k)\right)^2, \tag{3.66}$$

where $\hat{\phi}(\omega_k)$ is the model phase angle from (3.48) and $\phi(\omega_k)$ is the measured phase angle from (3.65) at frequency ω_k. The above problem can be solved using the iterative Newton-Gauss type algorithm [41, 98]. However, the solution needs a good initial guess as a general nonlinear least squares problem. In this paper, motivated from the pole/zero estimation from the phase angle measurements [99], the efficient iterative linear least squares method is proposed.

Let us define the even- and the odd functions of $G(\mathrm{j}\omega)$:

$$G_{\mathrm{e}}(\mathrm{j}\omega) = \frac{1}{2}\left(G(\mathrm{j}\omega) + G(-\mathrm{j}\omega)\right) = \frac{M(\mathrm{j}\omega)}{A(\mathrm{j}\omega)A(-\mathrm{j}\omega)} \tag{3.67}$$

$$G_{\mathrm{o}}(\mathrm{j}\omega) = \frac{1}{2}\left(G(\mathrm{j}\omega) - G(-\mathrm{j}\omega)\right) = \frac{N(\mathrm{j}\omega)}{A(\mathrm{j}\omega)A(-\mathrm{j}\omega)}, \tag{3.68}$$

where $M(\mathrm{j}\omega)$ and $N(\mathrm{j}\omega)$ are defined below.

$$M(\mathrm{j}\omega) = \frac{A(-\mathrm{j}\omega)B(\mathrm{j}\omega) + A(\mathrm{j}\omega)B(-\mathrm{j}\omega)}{2} \tag{3.69}$$

$$N(\mathrm{j}\omega) = \frac{A(-\mathrm{j}\omega)B(\mathrm{j}\omega) - A(\mathrm{j}\omega)B(-\mathrm{j}\omega)}{2} \tag{3.70}$$

And from (3.69) and (3.70),

$$M(\mathrm{j}\omega) + N(\mathrm{j}\omega) = A(-\mathrm{j}\omega)B(\mathrm{j}\omega) \tag{3.71}$$

$$M(\mathrm{j}\omega) - N(\mathrm{j}\omega) = A(\mathrm{j}\omega)B(-\mathrm{j}\omega) \tag{3.72}$$

Then, the phase angle function of the linear dynamic block is determined by:

$$\tan\phi(\omega) = \frac{G_{\mathrm{o}}(\mathrm{j}\omega)}{\mathrm{j}G_{\mathrm{e}}(\mathrm{j}\omega)} = \frac{N(\mathrm{j}\omega)}{\mathrm{j}M(\mathrm{j}\omega)} \tag{3.73}$$

The new FRF is defined and rewritten from (3.71)–(3.73):

$$T(\mathrm{j}\omega) \;=\; \frac{G(\mathrm{j}\omega)}{G(-\mathrm{j}\omega)} = \frac{A(-\mathrm{j}\omega)B(\mathrm{j}\omega)}{A(\mathrm{j}\omega)B(-\mathrm{j}\omega)} \;=\; \frac{1+\mathrm{j}\tan\phi(\omega)}{1-\mathrm{j}\tan\phi(\omega)} \tag{3.74}$$

The poles of $T(\mathrm{j}\omega)$ are the poles and negative zeros of $G(\mathrm{j}\omega)$. Similarly, the zeros of $T(\mathrm{j}\omega)$ are the zeros and negative poles of $G(\mathrm{j}\omega)$. The magnitude of $T(\mathrm{j}\omega)$ is uniformly one. If $G(\mathrm{j}\omega)$ is estimable from the phase angle measurement, $T(\mathrm{j}\omega)$ can be estimated either. Therefore, linear dynamic block identification is replaced by solving the following optimal problem:

$$\arg\min_{\mathtt{P}} \sum_{k=1}^{q} \qquad ||\hat{T}(\mathrm{j}\omega_k) - T(\mathrm{j}\omega_k)||^2, \tag{3.75}$$

where $\hat{T}(\mathrm{j}\omega_k)$ is the complex function of the linear dynamic block parameter `P` and $T(\mathrm{j}\omega_k)$ is the measurement at each frequency ω_k. $T(\mathrm{j}\omega)$ is identified using the iterative linear least squares method (SK-iteration) [98]. Then, by appropriate assignment of the poles and zeros of $T(\mathrm{j}\omega)$, the linear dynamic block parameter `P` is estimated. In this paper, the minimum phase and stable linear dynamic block is assumed. It is worth noting that the Wiener- and the Hammerstein models share the common linear dynamic block.

Nonlinear Static Block Estimation

Provided the linear dynamic block is identified, the nonlinear static blocks can be identified for both models. Since the harmonic output spectra are linear in the nonlinear static block parameter `Q`, (3.53)-(3.57) (Wiener model) and (3.58)-(3.62) (Hammerstein model) can be rewritten in matrix forms:

$$\Pi(\omega_k) \;=\; \Xi_W(\omega_k)X_W \tag{3.76}$$

$$\Pi(\omega_k) \;=\; \Xi_H(\omega_k)X_H, \tag{3.77}$$

where $\Pi(\omega_k) = [Y(0), Y(\mathrm{j}\omega_k), Y(2\mathrm{j}\omega_k), Y(3\mathrm{j}\omega_k), Y(4\mathrm{j}\omega_k)]^T \in \mathbb{C}^{5\times 1}$ is the complex vector of the measured harmonic output spectra and $X = [c_1,\ c_2,\ c_3,\ c_4]^T \in \Re^{4\times 1}$ is the real vector of `Q` to be estimated. $\Xi(\omega_k) \in \mathbb{C}^{5\times 4}$ is the complex regressor matrix determined appropriately from (3.53)-(3.57) and (3.58)-(3.62), respectively. The subscripts "W" and "H" represent the Wiener- and the Hammerstein models.

Nonlinear static block identification is finding the optimal $\mathtt{Q}$ minimizing the cost function given by

$$\arg\min_{\mathtt{Q}} \sum_{k=1}^{q} \quad ||\hat{\Pi}(\omega_k) - \Pi(\omega_k)||^2 \tag{3.78}$$

$\hat{\Pi}(\omega_k)$ is the model harmonic output spectra from (3.76) and (3.77) and $\Pi(\omega_k)$ is the measured harmonic output spectra at each frequency ω_k. Then, the linear least squares problem for each model structure is solved analytically [41]. Finally, the experimental GFRFs for the Wiener- and the Hammerstein models are computed using (3.50) and (3.51). It is noted that the experimental GFRFs do not have explicit connection with the physical parameters.

3.4.3 Spectral Analysis with Experimental Model

The prototype electrohydraulic actuator for camless engine valve actuation is used for experimental GFRFs identification, the detail of real time system settings are given in Table. 3.2.

Table 3.2: Experimental set up

component	specification
rapid control prototype	Matlab xPC target real time system
I/O interface	PCI-DAS1602-16 DAQ
position sensor	Microstrain NC-DVRT 1.0
voice coil motor	BEI Kimco Magnetics LA13-12-00A
power amplifier	Advanced Motion Controls 12A8

Experimental GFRFs

The estimated GFRFs of the Wiener- and Hammerstein models are shown in Figs. 3.10 and 3.11, respectively. As can be seen, their magnitude show quite different aspects due to the distinct nonlinear static blocks though both models share the common linear

dynamic block. From Fig. 3.10(b) and 3.10(c), $H_2(\mathrm{j}\omega_1, \mathrm{j}\omega_2)$ and $H_3(\mathrm{j}\omega_1, \mathrm{j}\omega_2, \mathrm{j}\omega_3)$ of the Wiener model shows quite similar patterns including the peaks and the ridges. For the Hammerstein model, $H_2(\mathrm{j}\omega_1, \mathrm{j}\omega_2)$ and $H_3(\mathrm{j}\omega_1, \mathrm{j}\omega_2, \mathrm{j}\omega_3)$ have the similar ridges without the peaks, but the ridge of $H_3(\mathrm{j}\omega_1, \mathrm{j}\omega_2, \mathrm{j}\omega_3)$ is shifted. $H_2(\mathrm{j}\omega_1, \mathrm{j}\omega_2)$ turns out to have the uniform impact on the zero frequency output spectrum.

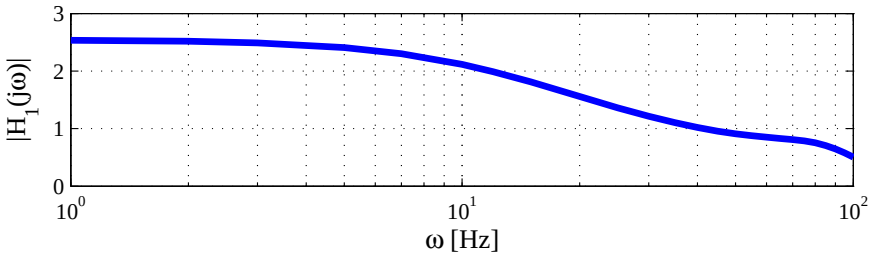

(a)

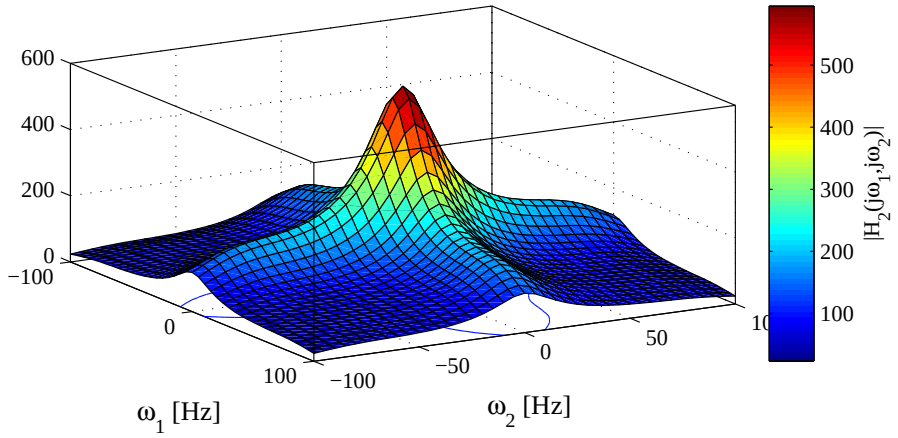

(b)

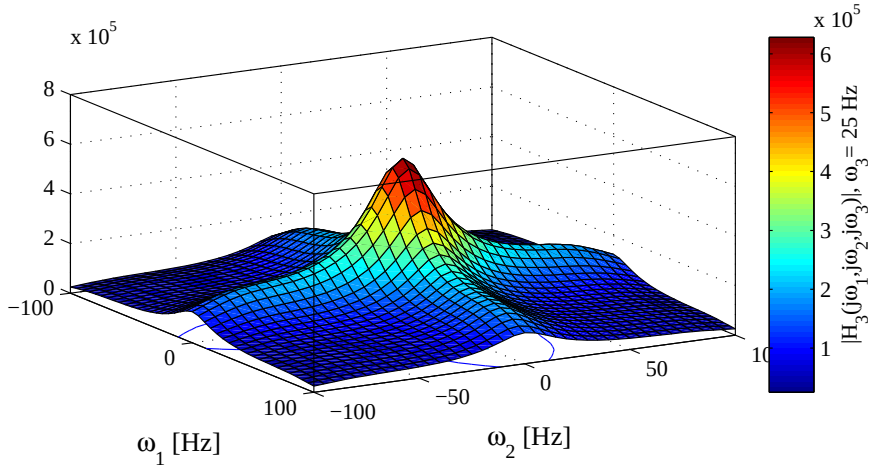

(c)

Figure 3.10: FRFs estimation with the Wiener model structure: (a)first order $H_1(\mathrm{j}\omega)$, (b)second order $H_2(\mathrm{j}\omega_1, \mathrm{j}\omega_2)$, (c)third order $H_3(\mathrm{j}\omega_1, \mathrm{j}\omega_2, \mathrm{j}\omega_3)$

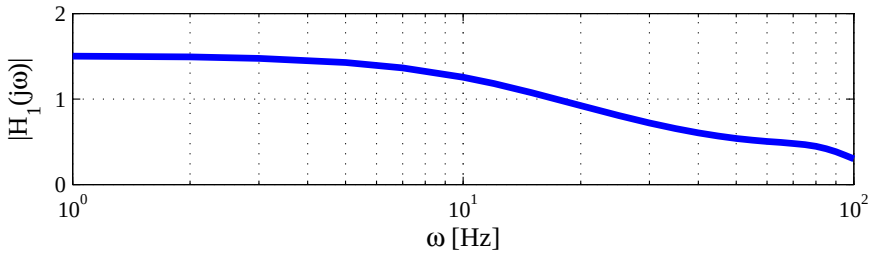

(a)

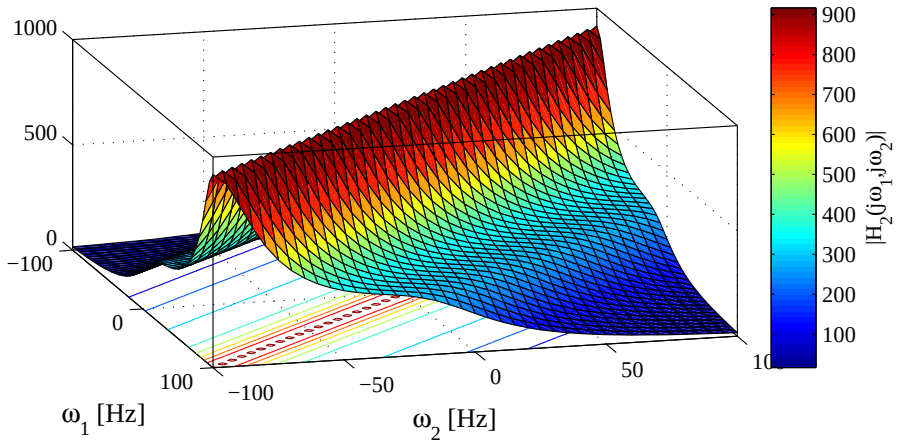

(b)

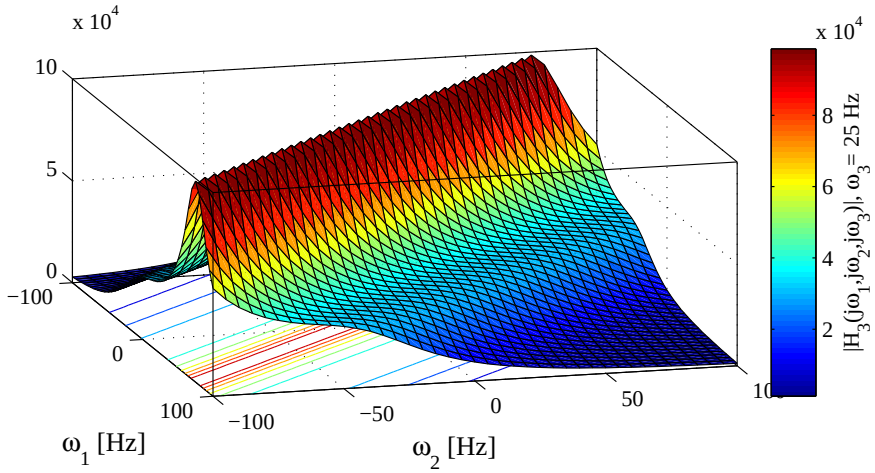

(c)

Figure 3.11: Experimental GFRFs with the Hammerstein model structure: (a)first order $H_1(\mathrm{j}\omega)$, (b)second order $H_2(\mathrm{j}\omega_1, \mathrm{j}\omega_2)$, (c)third order $H_3(\mathrm{j}\omega_1, \mathrm{j}\omega_2, \mathrm{j}\omega_3)$

Output Spectrum

The harmonic output spectra are computed using the identified GFRFs and they are compared with the measurements (i.e. DFT of the measured output) as shown in Fig.3.12. From the comparison, the Wiener model is found to show better performance in estimating the output spectra except at the three times of the input frequency. Compared to the analytic GFRFs, the experimental GFRFs outperform the analytic ones. However, physical interpretation is not available since the explicit connection with the physical parameters are absent.

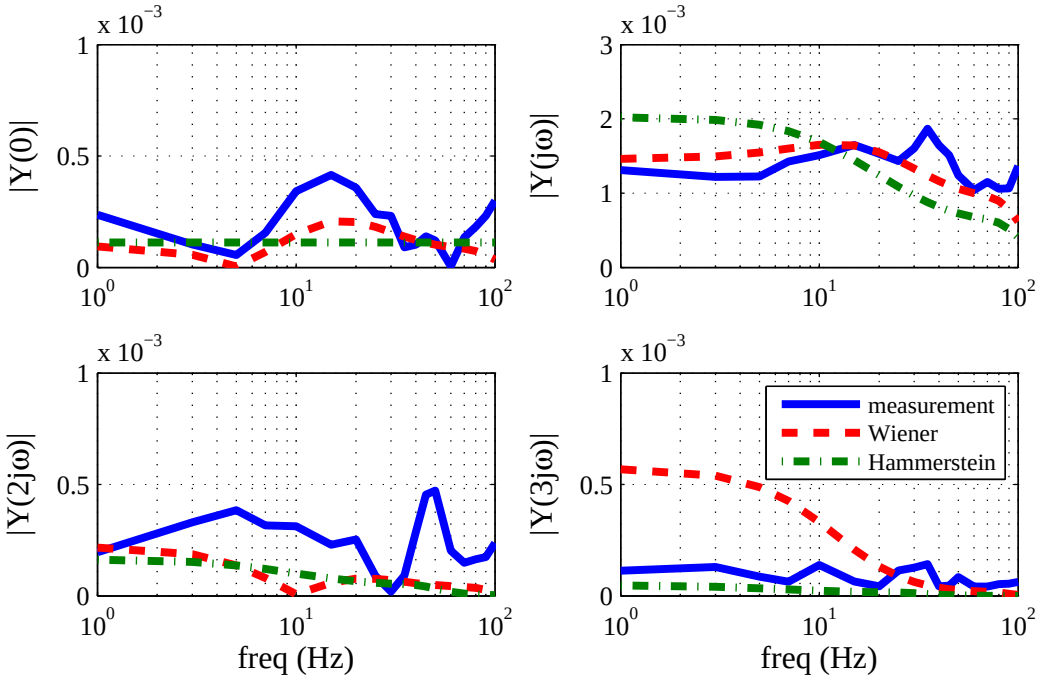

Figure 3.12: Analytic output spectrum: measurement(solid blue), Wiener model(dashed red), Hammerstein model(dashed-and-dotted green).

3.5 Conclusion

In this chapter, spectral analysis of the nonlinear electrohydraulic system is addressed to investigate its nonlinear dynamic features in frequency domain. The GFRFs

are derived in two different approaches based on Volterra series representation of the electrohydraulic system. In the first approach, the analytic method is proposed for GFRFs derivation from the physical dynamics of the electrohydraulic system. In the second approach, the experimental GFRFs are identified from the frequency response tests with the assumption of the block-oriented nonlinear systems: Wiener and Hammerstein models.

From analysis with the analytic GFRFs, it turns out that the considerable nonlinear dynamic features are found near the resonance frequency. Therefore, regarding the operating frequency range, different control strategies can be determined. Such nonlinear behavior near the resonance is further analyzed with respect to the input amplitude. As the input amplitude grows, the normalized fundamental output spectrum decreases due to the nonlinear hydraulic damping. And the given analytic GFRFs can capture such nonlinear behavior of the electrohydraulic system in a wide working range.

Although the analytic GFRFs offer great insight into system dynamics, its utility may be limited if the accurate physical dynamics is not available. In this case, the experimental GFRFs can be used with the appropriate choice of the model structure. Though the direct link to physical parameters is deficient, they enable to predict the output spectrum with acceptable accuracy.

Chapter 4

Robust Tracking Control of An Electrohydraulic Valve Actuator

In this chapter, robust motion control of a nonlinear electrohydraulic valve actuator for tracking nonstationary reference signals is presented. Two challenging issues encountered in many engineering applications, especially reciprocating machines, are addressed: 1) nonlinear system dynamics, 2) nonstationary reference signals. To achieve the control objective, internal model principle is adopted for tracking control design. To improve robust tracking performance, the high-order time varying internal model is proposed regarding nonlinear system dynamics and nonstationary reference signals. Its effectiveness is illustrated with the electrohydraulic camless engine valve actuator. The results of this chapter are reported in [100, 101].

4.1 Introduction

4.1.1 Background

A traditional internal combustion engine is configured with a camshaft, which transforms rotary motion into linear motion, to actuate intake and exhaust valves [62]. Since a camshaft is mechanically linked to a crankshaft by a timing belt or chain, valve motion depends on rotation of the crankshaft. Consequently, air flow management is limited over the range of engine speed and load.

On the contrary, the use of independent valve actuators enables fully flexible air management by active valve motion control [19]. Such a variable valve actuation system facilitates other control functions such as throttleless load control to reduce pumping loss, thereby to improve volumetric efficiency [16], and internal exhaust gas recirculation to decrease combustion temperature, and ultimately to reduce nitrogen oxide emissions [17]. An internal combustion engine of such capability is referred to as *a camless engine*. Depending on power source for valve actuation, an electromechanical, electrohydraulic, and electropneumatic valve actuators have been developed [18, 19, 20], and their mechanisms were introduced in Chap. 1 briefly. In this chapter, robust motion control of an electrohydraulic actuator for camless engine valves is addressed.

To make the electrohydraulic valve actuator feasible for the widespread application to the engine, it should satisfy the requirements addressed in [93]. Among them, robust and precise motion control is one of the most important aspects. However, to achieve such stringent control performance is challenging mainly because of two reasons: the nonlinear dynamic features of the electrohydraulic actuator; the nonstationary reference valve motion depending on the time varying engine speed.

The electrohydraulic actuator includes the nontrivial nonlinear dynamic features as presented in Chap. 3. To take account of the nonlinearities involved, nonlinear control methods have been actively studied such as feedback linearization, adaptive robust control, Lyapunov-based control, and backstepping [32, 33, 34, 35]. However, precise nonlinear physical models are expensive in general, and frequently they are not available due to the limited access for measurement. For the camless engine valve actuator used, the number of available sensors is limited due to the tight packaging.

Instead, linear frequency domain models, i.e. a transfer function in the frequency domain, are experimentally identified and used for linear control design such as a linear compensator, H-infinite control, feedforward + feedback control, and model predictive control with repetitive compensation [77, 76, 78, 79]. However, if the nonlinear dynamic features are critical, control performance with linear controls could be degraded. And the effectiveness of linear robust analysis is depreciated because uncertainties are nonlinear.

In this chapter, the nonlinear frequency domain model identified in Chap.3 will be used for control design. The block-oriented nonlinear systems including the Wiener-

and Hammerstein models have been broadly used to model unknown nonlinear systems when prior information is not available, because of their simplicity, and effective approximation of a wide class of nonlinear systems [102, 103, 104]. Tracking control of a nonlinear system is designed based on spectral analysis of a nonlinear feedback system. As shown in Chap. 3, system uncertainties were found, and they have to be taken into account for robust control design.

As in many reciprocating machines, the reference valve motion of an internal combustion engine is defined as a periodic signal in the rotational angle domain of the engine. However, it is aperiodic in time domain, because an engine speed varies in real time. Such a reference signal is referred to as *a nonstationary signal* of which frequency contents vary with time. This paper presents the robust motion control for tracking nonstationary reference signals of the nonlinear electrohydraulic actuator. To achieve the objective, internal model principle is employed for tracking control design in this chapter.

The internal model principle (IMP) was established by [105] for output regulation (reference tracking and/or disturbance rejection) of linear time invariant (LTI) systems when the reference (disturbance) is modeled by a LTI system referred to as *an exosystem*. The IMP states that the exosystem dynamics should be embedded into the control for asymptotic output regulation. The frequency domain interpretation is that the control has infinite gains at the reference frequencies due to inclusion of the exosystem poles on the imaginary axis [106]. As a specific application of the IMP, the repetitive control (RC) was studied for periodic reference tracking (and/or disturbance rejection) [107]. The principle was extended to nonlinear time invariant (NTI) systems [108], and its frequency domain interpretation was made using the Volterra series representation [40]. However, all these control methods deal with stationary reference signals whose frequency contents are fixed in time.

The IMP-based nonstationary reference tracking (and/or disturbance rejection) of LTI systems with the time varying internal model was studied in [42, 43] with input/output and state-space representation, respectively. They proposed the time varying internal model for nonstationary reference tracking. As a specific case, [109] presented time varying RC by converting system dynamics into the rotational angle domain and using angle-based sampling method. Robust stability issue which arises from the

time varying internal model was addressed in [44], and it was successfully illustrated through implementation on the electrohydraulic actuator [45]. However, the robust performance issue was not treated, and it is the focus of this chapter.

Motivated by successful applications of stationary reference tracking of NTI systems [41] and nonstationary reference tracking of LTI systems [45], the high-order time varying internal model is designed for nonstationary reference of NTI systems. The effectiveness in robust tracking performance is demonstrated. The preliminary results were reported in [100]. More detailed frequency domain analysis of the nonlinear system dynamics and the time-frequency analysis of the control system will be given in this chapter.

4.1.2 Problem Formulation

System Description

The input/output relationship of the electrohydraulic actuator is represented by Volterra series of the finite truncation order N to retain the nonlinear dynamic features such as

$$y(t) = \sum_{n=1}^{N} y_n(t) \tag{4.1}$$

$$y_n(t) = \int_{-\infty}^{\infty} \cdots \int_{-\infty}^{\infty} h_n(\tau_1, \cdots, \tau_n) \prod_{i=1}^{n} u(t-\tau_i) d\tau_i \tag{4.2}$$

The physical meanings of the variables are given in Chap. 3.

Reference Description

The engine position in the rotational angle domain is defined as presented in Chap. 2, and given by

$$\theta(t) = \theta_0 + \int_0^t \omega(t) dt, \tag{4.3}$$

where θ_0 and $\omega(t)$ are the initial position and the engine speed, respectively. Without loss of generality, zero initial position is assumed. The present engine speed is measured in real time precisely, but future information is not available. The reference $r(t) \in \mathbb{R}$

to be tracked is a periodic signal in the rotational angle domain. Therefore, it can be approximated by a finite sum of cosine functions with acceptable accuracy such as

$$r(t) = \sum_{k=0}^{p} \gamma_k \cos(\Omega_k \theta(t) + \psi_k), \tag{4.4}$$

where γ_k, Ω_k, and ψ_k are the amplitude, the frequency, and the phase of the kth element in the rotational angle domain, respectively. Ω_k is $k\Omega$, and Ω is referred to as the fundamental frequency of the reference in the rotational angle domain. The reference signal given by (4.4) is a nonstationary signal of which frequency contents depend on the engine speed.

Liner Time Varying Exosystem

The reference signal given by (4.4) can be modeled by an linear time varying (LTV) exosystem such as

$$\dot{x}_r(t) = A_r(t) x_r(t) \tag{4.5}$$

$$r(t) = C_r x_r(t), \tag{4.6}$$

where $x_r(t) \in \mathbb{R}^{n_{x_r} \times 1}$ is the state of the exosystem. The system matrices $A_r(t) \in \mathbb{R}^{n_{x_r} \times n_{x_r}}$ and $C_r \in \mathbb{R}^{1 \times n_{x_r}}$ are given by

$$A_r(t) = diag\left(\begin{bmatrix} 0 & A_{r_1}(t) & \cdots & A_{r_p}(t) \end{bmatrix}\right) \tag{4.7}$$

$$C_r = \begin{bmatrix} 1 & C_{r_1} & \cdots & C_{r_p} \end{bmatrix} \tag{4.8}$$

The submatrices A_{r_k} and C_{r_k} are given by

$$A_{r_k}(t) = \begin{bmatrix} 0 & \omega_k(t) \\ -\omega_k(t) & 0 \end{bmatrix} \tag{4.9}$$

$$C_{r_k} = \begin{bmatrix} 1 & 0 \end{bmatrix}, \tag{4.10}$$

where $\omega_k(t) = k\Omega\omega(t)$, and $\Omega\omega(t)$ is referred to as the time varying fundamental frequency of the reference in time domain.

Control Objective

The control objective is to design the robust output feedback control as shown in Fig. 4.1 for the nonlinear electrohydraulic valve actuator represented by (4.1) and (4.2) to track the nonstationary reference signal (4.4) modeled by the exosystem of (4.5) and (4.6).

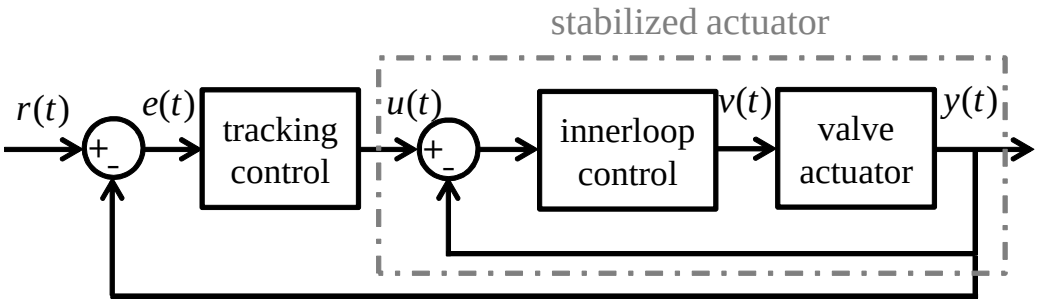

Figure 4.1: Dual feedback loop of the control system: innerloop control for stabilization, tracking control for reference tracking performance.

4.1.3 Outline

The rest of the chapter is organized as follows: Sec. 4.2 introduces mathematical preliminaries to interpret a nonstationary signal in time-frequency domain. Sec. 4.3 presents the robust stationary reference tracking control of a nonlinear system based on the internal model principle. In Sec. 4.4 the control design is extended to the robust nonstationary reference tracing control. In Sec. 4.5, the conclusion is drawn.

4.2 Mathematical Preliminaries

4.2.1 Time-frequency Analysis of Nonstationary Signal

In order to capture temporal information of nonstationary valve motion, the short time Fourier transform (STFT) will be used with assuming that the windowed signal is

stationary [110]. The STFT and the inverse STFT of the signal $y(t)$ are given by

$$Y(t,\omega) = \int_{-\infty}^{\infty} y(\tau)a(t-\tau)e^{-\mathrm{j}\omega\tau}d\tau \tag{4.11}$$

$$y(t) = \frac{1}{2\pi}\int_{\infty}^{\infty} Y(t,\omega)e^{\mathrm{j}\omega t}d\omega, \tag{4.12}$$

where $a(t)$ is the window function satisfying $a(0) = 1$. As shown in Fig. 4.2, the signal out of the window is significantly diluted, and the temporal signal remains with minimal corruption. Therefore, the temporal frequency contents can be read from the windowed signal.

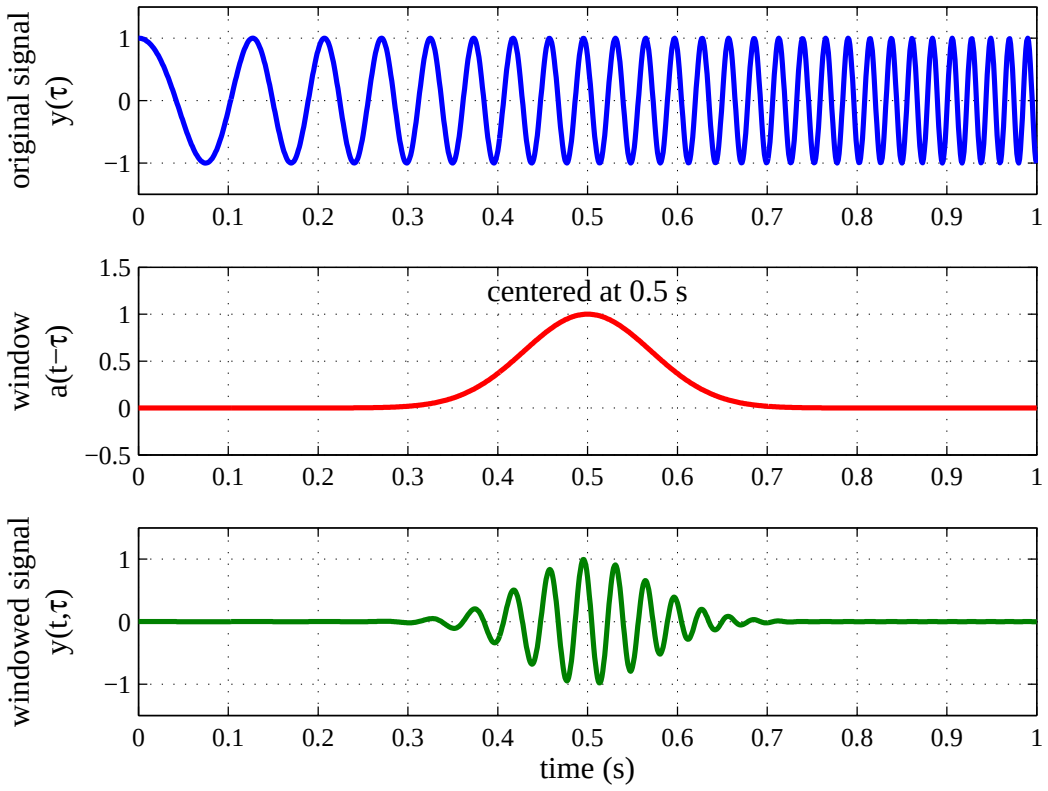

Figure 4.2: Short time Fourier transform: original nonstationary signal (first row), Gaussian window (second row), windoed signal (third row).

4.3 Stationary Reference Tracking

Prior to the nonstationary reference control of NTI systems, the stationary case is investigated to emphasize the effect of the high-order time invariant internal model. Then, the control method is extended to the nonstationary motion control by exploiting the high-order time varying internal model.

4.3.1 Control Design

The internal model design for stationary motion control of NTI systems was developed by [40] based on frequency domain analysis of a nonlinear feedback system. The brief summary will be given here.

If the engine speed is constant, the frequency contents of the reference signal are fixed in time, i.e. stationary motion. The reference (4.4) is rewritten with the exponential function accordingly

$$r(t) = \frac{1}{2}\sum_{k=-p}^{p} A_k e^{\mathrm{j}\omega_k t}, \tag{4.13}$$

where A_{-k} is the conjugate of the A_k (complex number), and $\omega_{-k} = -\omega_k$. Then, the reference can be modeled by an LTI exosystem in the form of (4.5) and (4.6), but with a constant system matrix, i.e. $A_r(t) = A_r$. The set of the exosystem eigenvalues is $\{0, \pm\mathrm{j}\omega_1, \cdots, \pm\mathrm{j}\omega_p\}$.

From the output feedback structure, Volterra series representing the relationship between the reference and the tracking error is given by

$$e_n(t) = \int_{-\infty}^{\infty} \cdots \int_{-\infty}^{\infty} f_n(\tau_1, \cdots, \tau_n) \prod_{i=1}^{n} r(t-\tau_i) d\tau_i \tag{4.14}$$

$$e(t) = \sum_{n=1}^{N} e_n(t), \tag{4.15}$$

where $f_n(\tau_1, \cdots, \tau_n)$ is the corresponding nth order Volterra kernel. The tracking error

Fourier transform is given by

$$\begin{aligned} E_n(\mathrm{j}\omega) &= \frac{1}{2^{n-1}} \sum_{\omega_{k_1}+\cdots+\omega_{k_n}=\omega} F_n(\mathrm{j}\omega_{k_1}, \cdots, \mathrm{j}\omega_{k_n}) \\ &\times A_{k_1} \cdots A_{k_n} \qquad (4.16) \\ E(\mathrm{j}\omega) &= \sum_{n=1}^{N} E_n(\mathrm{j}\omega), \qquad (4.17) \end{aligned}$$

where $k_i \in \{0, \pm 1, \cdots, \pm p\}$ for $i \in \{1, \cdots, n\}$ such that $\omega = \omega_{k_1} + \cdots + \omega_{k_n}$. $F_n(\mathrm{j}\omega_1, \cdots, \mathrm{j}\omega_n)$ is the nth order GFRF from the reference to the tracking error which corresponds to the sensitivity function of a linear system. From (4.16) and (4.17), the sufficient and necessary condition of the asymptotic tracking control is

$$F_n(\mathrm{j}\omega_{k_1}, \cdots, \mathrm{j}\omega_{k_n}) = 0, \quad \forall n. \qquad (4.18)$$

The control in the form of

$$C(\mathrm{j}\omega) = \frac{N_c(\mathrm{j}\omega)}{D_c(\mathrm{j}\omega)\phi(\mathrm{j}\omega)} \qquad (4.19)$$

is considered. Based on the cascade of the control and the valve actuator, the nth order GFRF from the tracking error to the output, i.e. open-loop, is

$$P_n(\mathrm{j}\omega_1, \cdots, \mathrm{j}\omega_n) = \prod_{i=1}^{n} C(\mathrm{j}\omega_i) H_n(\mathrm{j}\omega_1, \cdots, \mathrm{j}\omega_n) \qquad (4.20)$$

Then, applying GFRF algebra into the feedback loop yields the nth order GFRF from the reference to the tracking error given by

$$\begin{aligned} F_1(\mathrm{j}\omega) &= \frac{1}{1 + P_1(\mathrm{j}\omega)} \qquad (4.21) \\ &\vdots \\ F_n(\mathrm{j}\omega_1, \cdots, \mathrm{j}\omega_n) &= -F_1(\mathrm{j}\omega_1 + \cdots + \mathrm{j}\omega_n) Q_n(\mathrm{j}\omega_1, \cdots, \mathrm{j}\omega_n), \qquad (4.22) \end{aligned}$$

where $Q_n(\mathrm{j}\omega_1, \cdots, \mathrm{j}\omega_n)$ is shown below.

$$
\begin{aligned}
Q_2(\mathrm{j}\omega_1, \mathrm{j}\omega_2) &= F_1(\mathrm{j}\omega_1)F_1(\mathrm{j}\omega_2)P_2(\mathrm{j}\omega_1, \mathrm{j}\omega_2) && (4.23)\\
Q_3(\mathrm{j}\omega_1, \mathrm{j}\omega_2, \mathrm{j}\omega_3) &= F_1(\mathrm{j}\omega_1)F_1(\mathrm{j}\omega_2)F_1(\mathrm{j}\omega_3)\cdot P_3(\mathrm{j}\omega_1, \mathrm{j}\omega_2, \mathrm{j}\omega_3) && (4.24)\\
&+ \frac{2}{3}\big(F_1(\mathrm{j}\omega_1)F_2(\mathrm{j}\omega_2, \mathrm{j}\omega_3)P_2(\mathrm{j}\omega_1, \mathrm{j}\omega_2 + \mathrm{j}\omega_3)\\
&\quad + F_1(\mathrm{j}\omega_2)F_2(\mathrm{j}\omega_1, \mathrm{j}\omega_3)P_2(\mathrm{j}\omega_2, \mathrm{j}\omega_1 + \mathrm{j}\omega_3)\\
&\quad + F_1(\mathrm{j}\omega_3)F_2(\mathrm{j}\omega_1, \mathrm{j}\omega_2)P_2(\mathrm{j}\omega_3, \mathrm{j}\omega_1 + \mathrm{j}\omega_2)\big)\\
&\vdots
\end{aligned}
$$

If $N_c(\mathrm{j}\omega)/D_c(\mathrm{j}\omega)$ and $1/\phi(\mathrm{j}\omega)$ are designed such that

$$
\begin{aligned}
F_1(\mathrm{j}\omega) &: \text{ robustly stable} && (4.25)\\
\phi(\mathrm{j}\omega) = 0 &\qquad \forall \omega = \omega_{k_1} + \cdots + \omega_{k_n}, && (4.26)
\end{aligned}
$$

the sufficient and necessary condition for asymptotic reference tracking of (4.18) is satisfied. The former and the latter are referred to as *the stabilizer* and *the internal model*, respectively. In other words, if the linearized closed-loop is robustly stable, and the control possesses infinite gains at the positive n summation of the plus and minus reference frequencies for all $n \in \{1, \cdots, N\}$, then steady state tracking error converges to zero. Therefore, the internal model depends not only on the reference frequency, but also on the order of Volterra series. It is noted that the order of the internal model for NTI systems is higher than that for LTI systems, thus the internal model satisfying (4.26) is referred to as *the high-order time invariant internal model*. It is because NTI systems generates more frequency contents, i.e. harmonics of the input frequencies, than LTI systems do.

4.3.2 Revaluation of Repetitive Control

The interesting property of the repetitive control (RC) is observed in the view of the internal model. Although RC is developed based on the linear system theory, it has been successfully used even for nonlinear systems [111]. Such unexpected tracking performance can be explained by the high-order internal model. The robust discrete time RC is given by [107]:

$$
C(z^{-1}) = K_r M(z^{-1}) \frac{Q(z^{-1})z^{\delta}z^{-L}}{1 - Q(z^{-1})z^{-L}}, \qquad (4.27)
$$

where z^{-1} is the one step delay operator. L is the period of the reference such that the reference satisfies $(1 - z^{-L})r(k) = 0$ with the discrete time description at time k. K_r is the constant gain, $M(z^{-1})$ is the stable filter. z^{δ} is for causality, and $Q(z^{-1})$ is the low pass filter for robust stability of the feedback system. If $Q(z^{-1})$ is 1, the control possesses the infinite gains at all harmonic frequencies of the reference. But, if it is a low pass filter, the control gains are suppressed as illustrated in Fig. 4.3. The cosine function of 10 Hz plus the positive offset is regarded as the reference. The solid blue is the Bode plot of the linear IMP-based control, and the dashed red is the Bode plot of the robust RC. As can be seen, the linear IMP-based control has the peaks at 0 and 10 Hz exactly like the reference does. However, RC has more peaks at harmonics, i.e. 0, 10, 20, 30, 40, $\cdots$ Hz. Thus, RC can suppress the tracking error at these harmonic frequencies efficiently. Decreasing peak gains as frequency increases are due to the low pass filter, $Q(z^{-1})$, limiting the control gain for robust stability of the closed-loop. In summary, since RC possesses the intrinsic high-order internal model, it works very well even for stationary motion control of NTI systems.

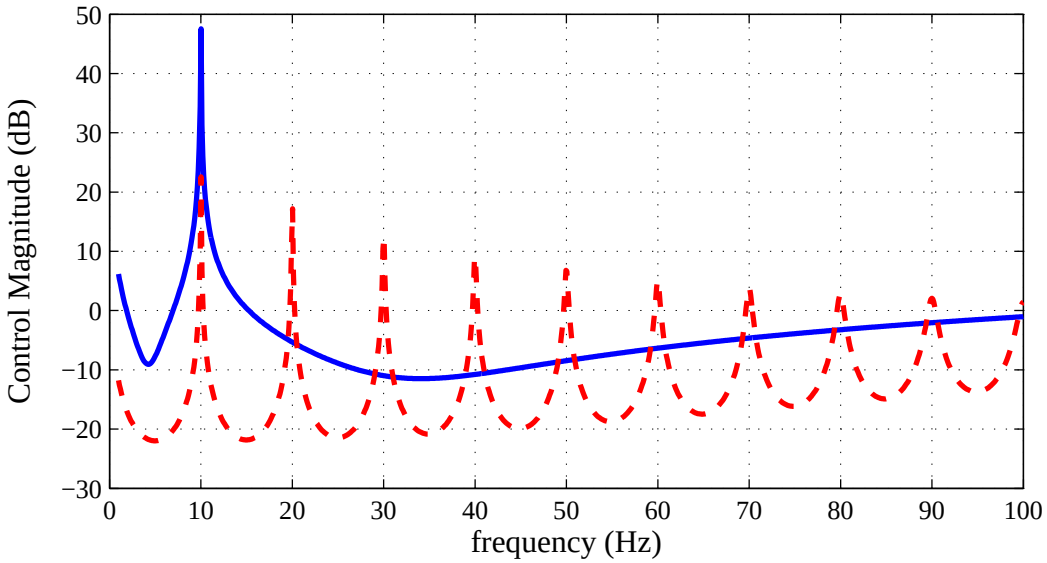

Figure 4.3: Control Bode plot: linear IMP-based control having the low-order internal model (soild blue), robust RC having the intrinsic high-order internal model (dashed red).

4.3.3 Simulations & Experiments

The reference signal is given by

$$r(t) \quad = \quad \gamma_0 + \gamma_1 \cos\left(\int_0^t \omega_1(t)dt + \psi_1\right) \tag{4.28}$$

For comparison, the tracking control with the low-order internal model is designed with the assumption of a linear actuator model. The low-order internal model is exactly same with the exosystem dynamics [106]

First, the robust stationary motion control is demonstrated with the high-order time invariant internal model. In (4.28), $\omega_1(t)$ is fixed as 10 Hz. For the linear approach using the low-order time invariant internal model, the pole placement method is used for stabilizing the closed-loop system. As addressed, the robust RC is regarded as the high-order internal model approach because it includes the intrinsic high-order time invariant internal model.

The results of simulation and experiment are shown in Figs. 4.4 and 4.5. In each figure, the first- and second columns show the time traces and discrete Fourier transforms (DFTs), respectively. Three rows indicate the stationary reference motion, control input, and tracking error in order. The solid blue and dashed red indicate the results with the low-order and high-order internal models, respectively. Superior tracking performance of the high-order time invariant internal model to the low-order one is observed: 87 % and 14 % reductions in the maximum magnitude of the tracking error for simulation and experiment, respectively.

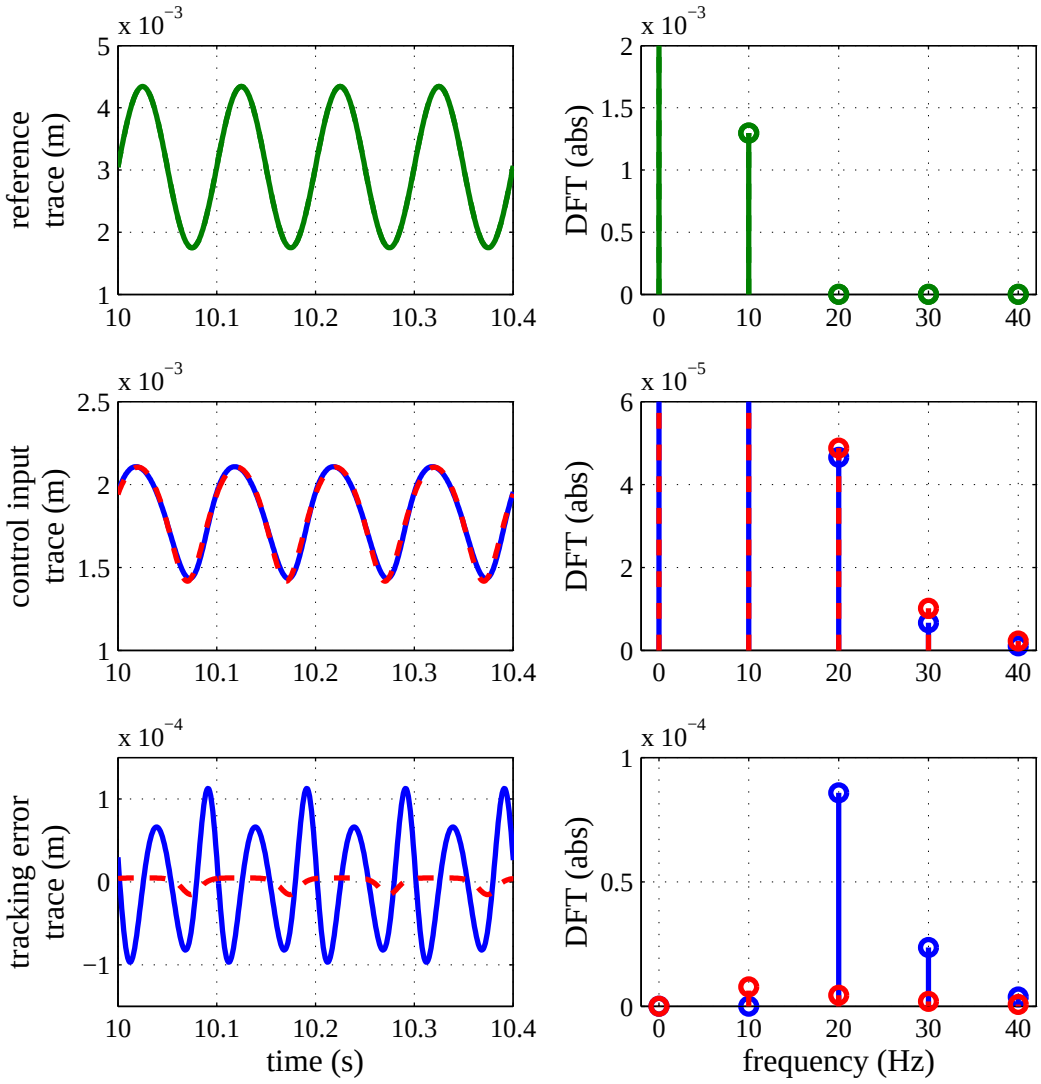

Figure 4.4: Simulation results of the stationary motion control: time traces (first column), and DFTs (second column), low-order time invariant internal model (solid blue), high-order time invariant internal model (dashed red) in the second and third rows.

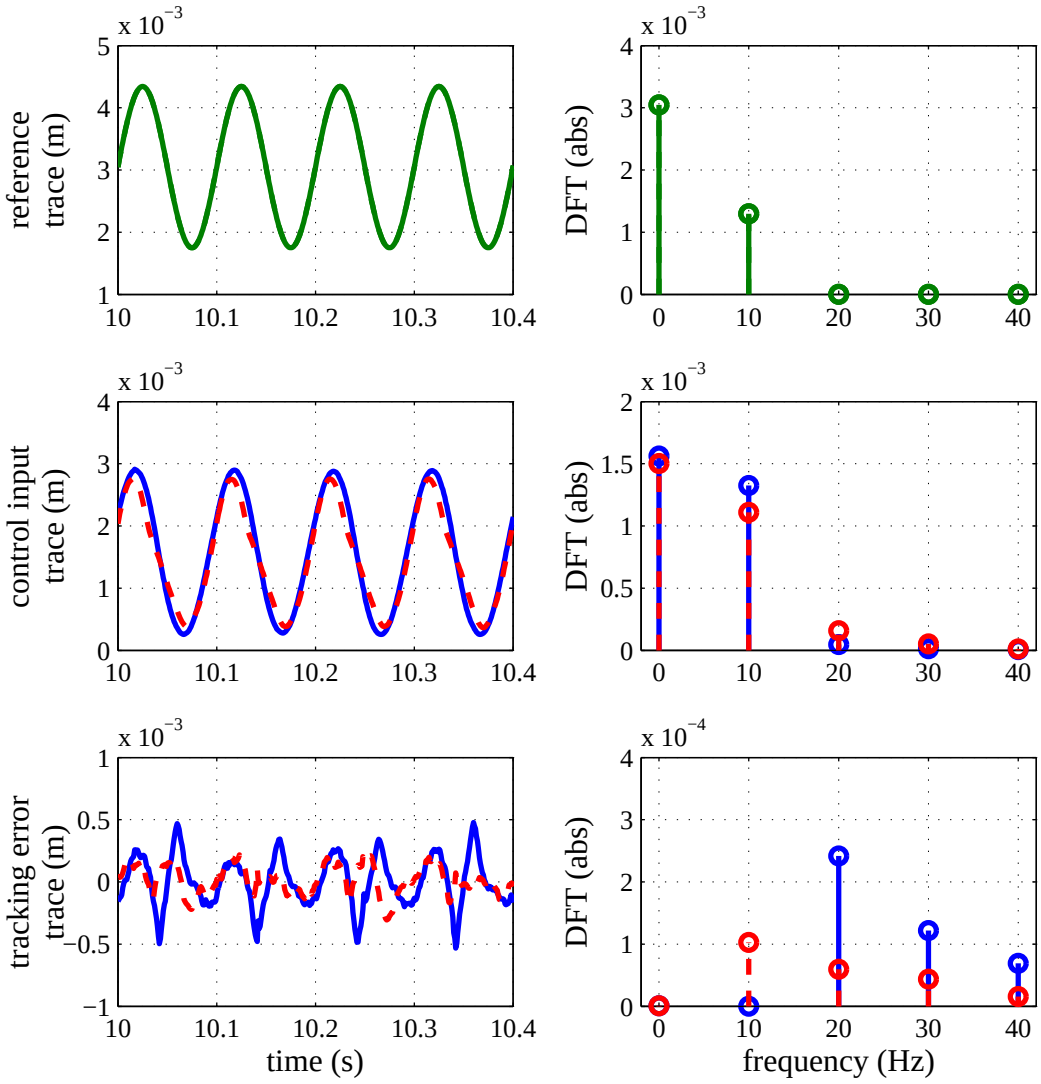

Figure 4.5: Experiment results of the stationary motion control: time traces (first column), and DFTs (second column), low-order time invariant internal model (solid blue), high-order time invariant internal model (dashed red) in the second and third rows.

4.4 Nonstationary Reference Tracking

4.4.1 Control Design

If the engine speed varies with time, the frequency contents of the reference vary with time, i.e. nonstationary motion. The reference (4.4) is rewritten by

$$r(t) = \frac{1}{2}\sum_{k=-p}^{p} A_k e^{\int_0^t \mathrm{j}\omega_k(\tau)d\tau}. \tag{4.29}$$

The reference can be modeled by an LTV exosystem in the form of (4.5) and (4.6) with a time varying system matrix $A_r(t)$.

For the nonstationary motion control, the IMP with the frequency domain interpretation is extended to time-frequency domain interpretation. If the window function $a(t)$ is highly concentrated at the origin, the reference/tracking error relationship of a nonlinear time varying feedback system in the STFT domain is approximated by

$$\begin{aligned} E_n(t,\mathrm{j}\omega) &\approx \frac{1}{(2\pi)^{n-1}}\int_{-\infty}^{\infty}\cdots\int_{-\infty}^{\infty} F_n(t,\mathrm{j}\omega_1,\cdots,\mathrm{j}\omega_n) \\ &\quad R(t,\mathrm{j}\omega_1)\cdots R(t,\mathrm{j}\omega_n)d\omega_1\cdots d\omega_{n-1} \end{aligned} \tag{4.30}$$

$$E(t,\mathrm{j}\omega) \approx \sum_{n=1}^{N} E_n(t,\mathrm{j}\omega) \tag{4.31}$$

Motivated by the stationary case, the nonstationary reference tracking control of NTI systems which consists of the scheduled static gains and time varying internal model [44, 45] is designed so that the followings are satisfied.

$$F_1(t,\mathrm{j}\omega) : \text{robustly stable} \tag{4.32}$$

$$\phi(t,\mathrm{j}\omega) = 0 \qquad \forall\omega = \omega_{k_1} + \cdots + \omega_{k_n}. \tag{4.33}$$

where the variable definitions are similar with the stationary case except the time notation for indicating time varying properties.

Gain-scheduling based on linear matrix inequalities (LMI) is employed to stabilize the linearized closed-loop of (4.32). The gains are calculated offline with several engine speeds, then the interpolation is implemented with measuring the present engine speed. The high-order time varying internal model given by (4.33) is realized in a matrix form such as (4.5) and (4.6). Similarly with the stationary case, the time varying

internal model satisfying (4.33) possesses a high order than the time varying exosystem dynamics. The details of gain scheduling and realization of a time varying internal model can be found from [44, 45].

4.4.2 Simulations & Experiments

The robust nonstationary motion control is demonstrated with the high-order time varying internal model. In (4.28), $\omega_1(t)$ is assumed to increase linearly from 5 to 20 Hz with the rate of 1 Hz/s.

Figs. 4.6 and 4.8 show the comparison of the time traces and the DFTs between the low-order and high-order time varying internal model approaches. Superior tracking performance of the high-order time varying internal model to the low-order one is observed: 79 % and 70 % reductions in the maximum magnitude of the tracking error for simulation and experiment, respectively. Figs. 4.7 and 4.8 show the STFTs of the control input and tracking error at the several times. As can be seen in Fig. 4.7, the aggressive control input at the harmonic frequencies mitigates the tracking errors at the harmonic frequencies efficiently, though their magnitude is relatively small.

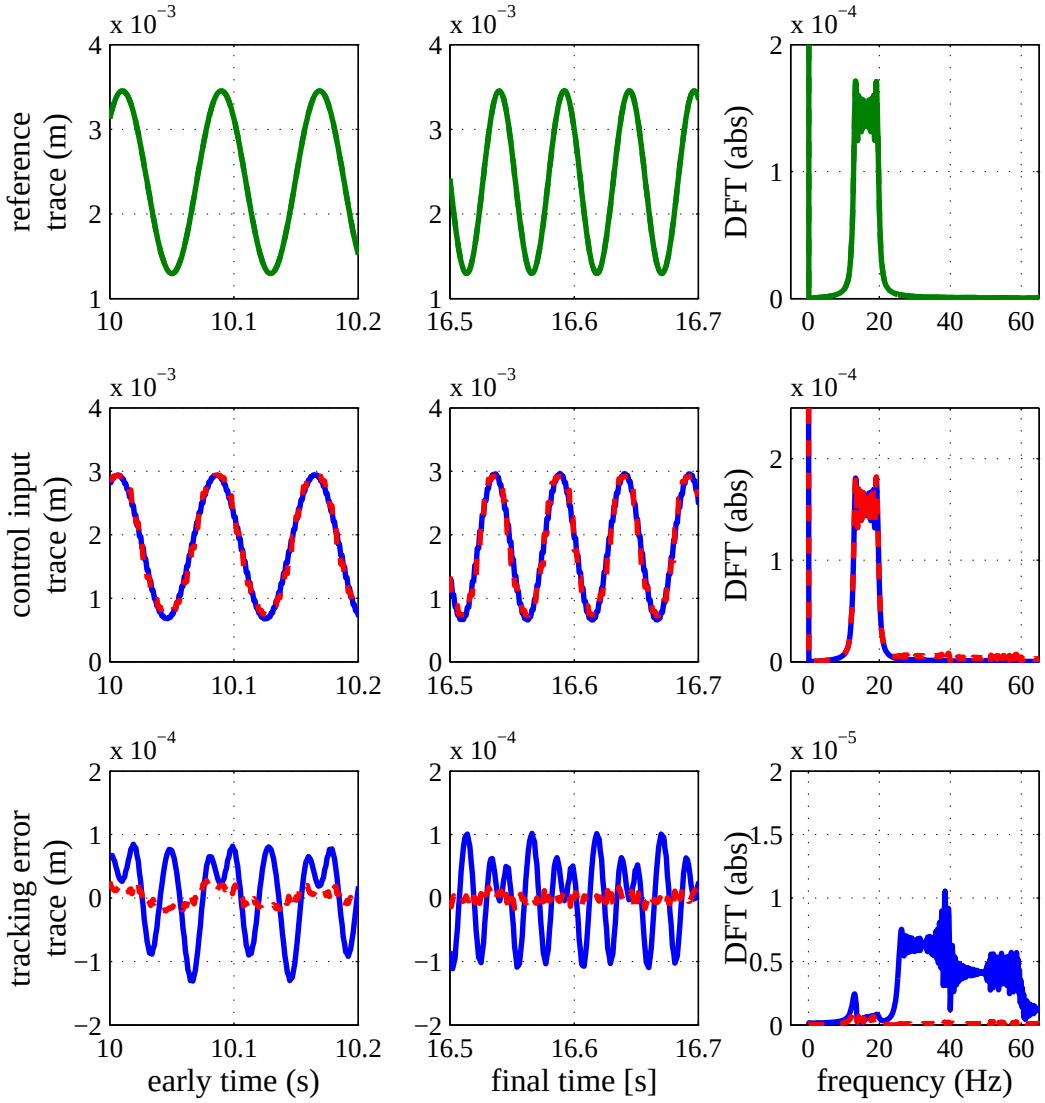

Figure 4.6: Simulation results of the nonstationary motion control: time traces (first and second columns) and DFTs (third column); low-order (solid blue) and high-order (dashed red) time varying internal models in the second and third rows.

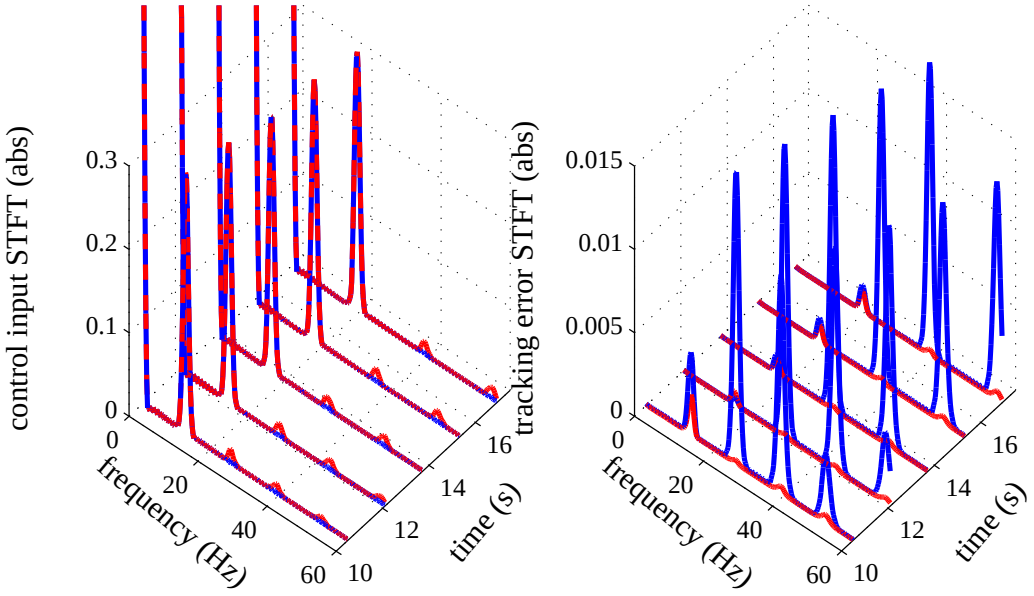

Figure 4.7: STFTs of simulation results: control input (left), and tracking error (right); low-order (solid blue) and high-order (dashed red) time varying internal models.

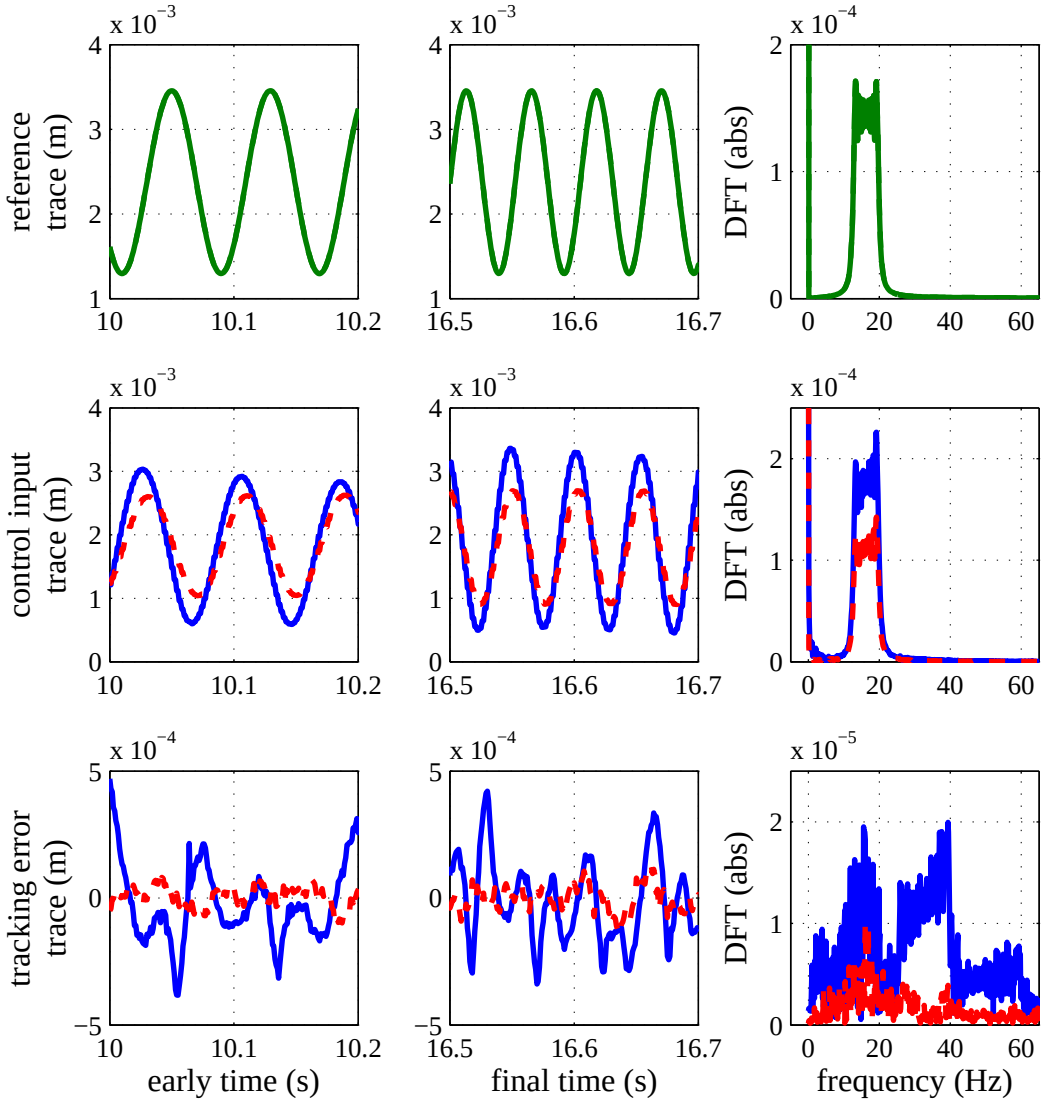

Figure 4.8: Experiment results of the nonstationary motion control: time traces (first and second column) and DFTs (third column); low-order (solid blue) and high-order (dashed red) time varying internal models in the second and third rows.

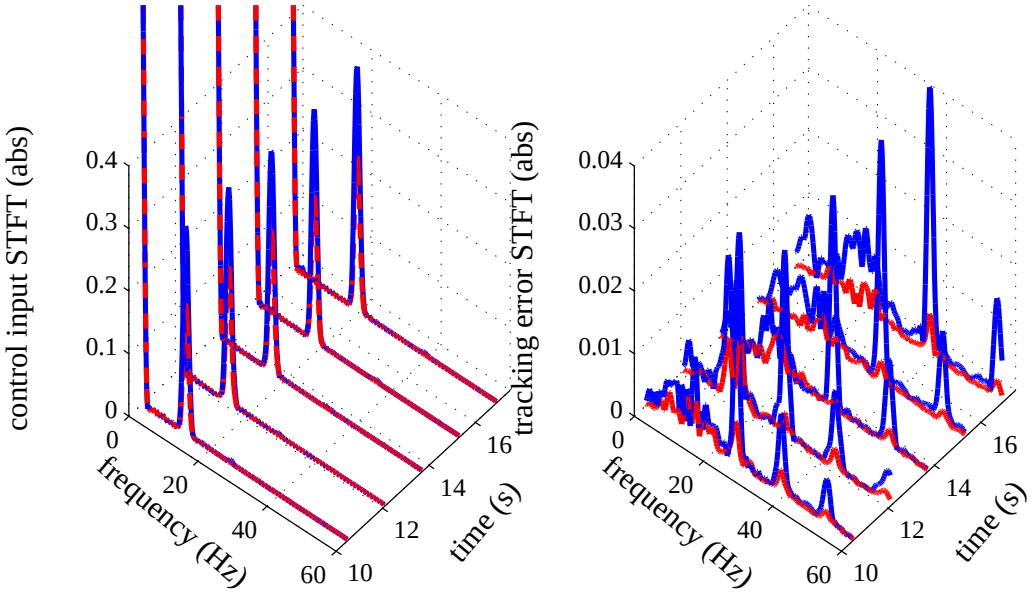

Figure 4.9: STFTs of experiment results: control input (left) and tracking error (right); low-order (solid blue) and high-order (dashed red) time varying internal models.

4.5 Conclusion

In this chapter, robust tracking control of a nonlinear electrohydraulic valve actuator for camless engine is presented to follow nonstationary reference signals on the basis of frequency domain interpretation of internal model principle. Special attention is given to internal model design regarding the nonstationary reference signals and nonlinear dynamics of the actuator. Prior to the nonstationary reference tracking, the stationary case is first investigated. Based on frequency domain analysis of a nonlinear feedback system represented by generalized frequency response functions, the high-order time invariant internal model is designed to improve robust tracking performance. Motivated by the stationary case, the high-order time varying internal model is designed for tracking the nonstationary reference signal that can be modeled by a time varying exosystem. The effectiveness of the proposed design is demonstrated by implementation on the electrohydraulic camless engine valve actuator. From simulation and experimental results, significant improvements of robust tracking performance were observed.

References

[1] U.S. Environment Protection Agency, "Inventory of U.S. greenhouse gas emissions and sinks: 1990-2013," 2011.

[2] U.S. Department of Transportation NHTSA, "Summary of fuel economy performance," 2011.

[3] ——, "NHTSA MY2017-2025 Factsheet," 2011.

[4] International Council on Clear Transportation, "U.S. Tier 3 motor vehicle emission and fuel standards (final rule)," 2014.

[5] M. B. Barron and W. F. Powers, "The role of electronic controls for future automotive mechatronic systems," *IEEE/ASME Transactions on Mechatronics*, vol. 1, no. 1, pp. 80–88, 1996.

[6] L. Guzzella and C. Onder, *Introduction to modeling and control of internal combustion engine systems.* Berlin, Germany: Springer, 2009.

[7] Z. Sun and G. G. Zhu, *Design and control of automotive propulsion systems.* Boca Raton, FL: CRC Press, 2014.

[8] J. Rivard, "Closed-loop electronic fuel injection control of the internal combustion engine," *SAE Technical Paper*, no. 730005, 1973.

[9] T. Kume, Y. Iwamoto, K. Iida, M. Murakami, K. Akishino, and H. Ando, "Combustion control technologies for direct injection si engine," *SAE Technical Paper*, no. 960600, 1996.

[10] K. Tanabe, S. Kohketsu, and S. Nakayama, "Effect of fuel injection rate control on reduction of emissions and fuel consumption in a heavy duty DI diesel engine," *SAE Technical Paper*, no. 2005-01-0907, 2005.

[11] N. Guerrassi and P. Dupraz, "A common rail injection system for high speed direct injection diesel engines," *SAE Technical Paper*, no. 980803, 1998.

[12] H.-M. Streib and H. Bischof, "Electronic throttle control (ETC): a cost effective system for improved emissions, fuel economy, and driveability," *SAE Technical Paper*, no. 960338, 1996.

[13] H. Winner, S. Witte, W. Uhler, and B. Lichtenberg, "Adaptive cruise control system aspects and development trends," *SAE Technical Paper*, 1996.

[14] J.-B. Song and K.-S. Byun, "Throttle actuator control system for vehicle traction control," *Mechatronics*, vol. 9, no. 5, pp. 477–495, 1999.

[15] T. Ahmad and M. Theobald, "A survey of variable-valve-actuation technology," *SAE Technical Paper*, no. 891674, 1989.

[16] R. Flierl and M. Klüting, "The third generation of valvetrains-new fully variable valvetrains for throttle-free load control," *SAE Technical Paper*, no. 2000-01-1227, 2000.

[17] D. Law, D. Kemp, J. Allen, G. Kirkpatrick, and T. Copland, "Controlled combustion in an IC-engine with a fully variable valve train," *SAE Technical Paper*, 2001.

[18] K. S. Peterson and A. G. Stefanopoulou, "Extremum seeking control for soft landing of an electromechanical valve actuator," *Automatica*, vol. 40, no. 6, pp. 1063–1069, 2004.

[19] Z. Sun and T.-W. Kuo, "Transient control of electro-hydraulic fully flexible engine valve actuation system," *IEEE Transactions on Control Systems Technology*, vol. 18, no. 3, pp. 613–621, 2010.

[20] J. Ma, G. G. Zhu, and H. Schock, "Adaptive control of a pneumatic valve actuator for an internal combustion engine," *IEEE Transactions on Control Systems Technology*, vol. 19, no. 4, pp. 730–743, 2011.

[21] S.-C. Kong, C. D. Marriott, R. D. Reitz, and M. Christensen, "Modeling and experiments of HCCI engine combustion using detailed chemical kinetics with multidimensional CFD," *SAE Technical Paper*, no. 2001-01-1026, 2001.

[22] A. Babajimopoulos, G. A. Lavoie, and D. N. Assanis, "Modeling HCCI combustion with high levels of residual gas fraction - a comparison of two VVA strategies," *SAE technical paper*, no. 2003-01-3220, 2003.

[23] N. Milovanovic, R. Chen, and J. Turner, "Influence of the variable valve timing strategy on the control of a homogeneous charge compression (hcci) engine," *SAE Technical Paper*, no. 2004-01-1899, 2004.

[24] A. M. Mahrous, A. Potrzebowski, M. Wyszynski, H. Xu, A. Tsolakis, and P. Luszcz, "A modelling study into the effects of variable valve timing on the gas exchange process and performance of a 4-valve DI homogeneous charge compression ignition (HCCI) engine," *Energy Conversion and Management*, vol. 50, no. 2, pp. 393–398, 2009.

[25] T. L. Bergman, F. P. Incropera, and A. S. Lavine, *Fundamentals of heat and mass transfer*. Hoboken, NJ: John Wiley & Sons, 2011.

[26] M. Vollmer, S. Henke, D. Karstädt, K. Möllmann, and F. Pinno, "Challenges in infrared imaging: low emissivities of hot gases, metals, and metallic cavities," in *Infrared Camera Calibration Conference*, 2004.

[27] R. Schießl, A. Dreizler, and U. Maas, "Comparison of different ways for image post-processing: detection of flame fronts," Tech. Rep. 1999-01-3651, 1999.

[28] C. Espey and J. E. Dec, "Diesel engine combustion studies in a newly designed optical-access engine using high-speed visualization and 2-d laser imaging," *SAE Technical Paper*, no. 930971, 1993.

[29] C. Arcoumanis, C. Bae, and Z. Hu, "Flow and combustion in a four-valve, spark-ignition optical engine," *SAE Technical Paper*, no. 940475, 1994.

[30] Z. Lang and S. Billings, "Energy transfer properties of non-linear systems in the frequency domain," *International Journal of Control*, vol. 78, no. 5, pp. 345–362, 2005.

[31] S. Billings and K. Tsang, "Spectral analysis for nonlinear systems, part ii: Interpretation of nonlinear frequency response functions," *Mechanical Systems and Signal Processing*, vol. 3, no. 4, pp. 341–359, 1989.

[32] G. Vossoughi and M. Donath, "Dynamic feedback linearization for electrohydraulically actuated control systems," *Journal of Dynamic Systems, Measurement, and Control*, vol. 117, no. 4, pp. 468–477, 1995.

[33] B. Yao, F. Bu, J. Reedy, and G. T. Chiu, "Adaptive robust motion control of single-rod hydraulic actuators: theory and experiments," *IEEE/ASME Transactions on Mechatronics*, vol. 5, no. 1, pp. 79–91, 2000.

[34] A. Alleyne and R. Liu, "A simplified approach to force control for electro-hydraulic systems," *Control Engineering Practice*, vol. 8, no. 12, pp. 1347–1356, 2000.

[35] C. Kaddissi, J.-P. Kenné, and M. Saad, "Identification and real-time control of an electrohydraulic servo system based on nonlinear backstepping," *IEEE/ASME Transactions on Mechatronics*, vol. 12, no. 1, pp. 12–22, 2007.

[36] E.-W. Bai, "Frequency domain identification of Hammerstein models," *IEEE Transactions on Automatic Control*, vol. 48, no. 4, pp. 530–542, 2003.

[37] ——, "Frequency domain identification of Wiener models," *Automatica*, vol. 39, no. 9, pp. 1521–1530, 2003.

[38] X. Jing, "Frequency domain analysis and identification of block-oriented nonlinear systems," *Journal of Sound and Vibration*, vol. 330, no. 22, pp. 5427–5442, 2011.

[39] S. Skogestad and I. Postlethwaite, *Multivariable feedback control: analysis and design*. New York: Wiley, 2007.

[40] J. Huang, "Asymptotic tracking in uncertain Volterra systems," *Systems & Control Letters*, vol. 31, no. 4, pp. 215–223, 1997.

[41] Y. Yoon and Z. Sun, "Nonlinear identification and robust tracking control of a camless engine valve actuator based on a Volterra series representation," in *the proceedings of American Control Conference*, 2014, pp. 1535–1540, portland, OR, USA.

[42] Z. Sun, Z. Zhang, and T.-C. Tsao, "Trajectory tracking and disturbance rejection for linear time-varying systems: Input/output representation," *Systems & Control Letters*, vol. 58, no. 6, pp. 452–460, 2009.

[43] Z. Zhang and Z. Sun, "A novel internal model-based tracking control for a class of linear time-varying systems," *Journal of Dynamic Systems, Measurement, and Control*, vol. 132, no. 1, p. 011004, 2010.

[44] X. Song, Y. Wang, and Z. Sun, "Robust stabilizer design for linear time-varying internal model based output regulation and its application to an electrohydraulic system," *Automatica*, vol. 50, no. 4, pp. 1128–1134, 2014.

[45] P. K. Gillella, X. Song, and Z. Sun, "Time-varying internal model-based control of a camless engine valve actuation system," *Control Systems Technology, IEEE Transactions on*, vol. 22, no. 4, pp. 1498–1510, 2014.

[46] S. Zhang, G. G. Zhu, Y. Yoon, and Z. Sun, "A control oriented charge mixing and HCCI combustion model for internal combustion engines," in *proceedings of Dynamic Systems and Control Conference*. ASME, 2012, pp. 321–327, Washington DC, USA.

[47] Y. Yoon, Z. Sun, S. Zhang, and G. G. Zhu, "Development of control-oriented charge mixing model and experimental validation using graphical analysis," in *the proceedings of American Control Conference*. IEEE, 2013, pp. 4441–4446, washington DC, USA.

[48] ——, "A control-oriented two-zone charge mixing model for hcci engines with experimental validation using an optical engine," *Journal of Dynamic Systems, Measurement, and Control*, vol. 136, no. 4, p. 041015, 2014.

[49] M. Yao, Z. Zheng, and H. Liu, "Progress and recent trends in homogeneous charge compression ignition (HCCI) engines," *Progress in Energy and Combustion Science*, vol. 35, no. 5, pp. 398–437, 2009.

[50] X. Lu, D. Han, and Z. Huang, "Fuel design and management for the control of advanced compression-ignition combustion modes," *Progress in Energy and Combustion Science*, vol. 37, no. 6, pp. 741–783, 2011.

[51] R. H. Stanglmaier and C. E. Roberts, "Homogeneous charge compression ignition (HCCI): benefits, compromises, and future engine applications," *SAE Technical Paper*, no. 1999-01-3682, 1999.

[52] G. Haraldsson, P. Tunestål, B. Johansson, and J. Hyvönen, "HCCI combustion phasing with closed-loop combustion control using variable compression ratio in a multi-cylinder engine," *SAE Transactions, Journal of Engines*, vol. 112, no. 4, pp. 1233–1245, 2003.

[53] F. Agrell, H.-E. Ångström, B. Eriksson, J. Wikander, and J. Linderyd, "Integrated simulation and engine test of closed loop HCCI control by aid of variable valve timings," *SAE Technical Paper*, no. 2003-01-0748, 2003.

[54] T. Urushihara, K. Hiraya, A. Kakuhou, and T. Itoh, "Expansion of HCCI operating region by the combination of direct fuel injection, negative valve overlap and internal fuel reformation," no. 2003-01-0749, 2003.

[55] D. Rausen, A. Stefanopoulou, J.-M. Kang, J. Eng, and T.-W. Kuo, "A mean-value model for control of homogeneous charge compression ignition (HCCI) engines," *Journal of Dynamic Systems, Measurement, and Control*, vol. 127, no. 3, pp. 355–362, 2005.

[56] N. J. Killingsworth, S. M. Aceves, D. L. Flowers, and M. Krstić, "A simple HCCI engine model for control," in *proceedings of International Conference on Control Applications*, 2006, pp. 2424–2429, Munich, Germany.

[57] G. M. Shaver, J. C. Gerdes, M. J. Roelle, P. A. Caton, and C. F. Edwards, "Dynamic modeling of residual-affected homogeneous charge compression ignition engines with variable valve actuation," *Journal of Dynamic Systems, Measurement, and Control*, vol. 127, no. 3, pp. 374–381, 2005.

[58] V. Tandra and N. Srivastava, "A two zone model of a single cylinder HCCI engine for control applications," in *proceedings of Dynamic Systems and Control Conference*. ASME, 2008, pp. 63–70, ann Arbor, MI, USA.

[59] M. J. McCuen, Z. Sun, and G. Zhu, "Control-oriented mixing model for homogeneous charge compression ignition engines," in *proceedings of American Control Conference*. IEEE, 2010, pp. 3809–3816, baltimore, MD, USA.

[60] T. S. Wilson, H. Xu, S. Richardson, M. L. Wyszynski, and T. Megaritis, "Optical study of flow and combustion in an HCCI engine with negative valve overlap," in *Journal of Physics: Conference Series*, vol. 45, no. 1. IOP Publishing, 2006, p. 94.

[61] C. W. Squibb, H. Schock, T. Stuecken, M. Poort, K. Crayne, C. Gray, and F. Hamady, "A demonstration of simultaneous infrared and visible imaging techniques with pressure data in an optically accessible diesel engine operating at part load with high egr," *SAE Technical Paper*, no. 2011-01-1395, 2011.

[62] J. B. Heywood, *Internal combustion engine fundamentals*. McGraw-Hill, 1988, New York.

[63] G. Woschni, "A universally applicable equation for the instantaneous heat transfer coefficient in the internal combustion engine," *SAE paper*, vol. 670931, no. 1, p. 2, 1967.

[64] J. Smits, "Modeling of a fluid flow in an internal combustion engine," MS Thesis, Eindhoven University of Technology, Eindhoven, 2006.

[65] Y. Song, J. Hong, and J. Lee, "The turbulence measurement during the intake and compression process for high-turbulence generation around spark timing," *Proceedings of the Institution of Mechanical Engineers, Part D: Journal of Automobile Engineering*, vol. 215, no. 4, pp. 493–501, 2001.

[66] A. K. Jain, M. N. Murty, and P. J. Flynn, "Data clustering: a review," *ACM computing surveys (CSUR)*, vol. 31, no. 3, pp. 264–323, 1999.

[67] M. Ochs, T. Horbach, A. Schulz, R. Koch, and H. Bauer, "A novel calibration method for an infrared thermography system applied to heat transfer experiments," *Measurement Science and Technology*, vol. 20, no. 7, p. 075103, 2009.

[68] Y. Yoon and Z. Sun, "Spectral analysis of electrohydraulic system," *Journal of Dynamic Systems, Measurement, and Control*, submitted.

[69] ——, "Block-oriented nonlinear system identification based on frequency domain analysis," 2015, in preparation.

[70] T. Lin, Q. Wang, B. Hu, and W. Gong, "Development of hybrid powered hydraulic construction machinery," *Automation in Construction*, vol. 19, no. 1, pp. 11–19, 2010.

[71] M. O'Connor, T. Bell, G. Elkaim, and B. Parkinson, "Automatic steering of farm vehicles using GPS," *Precision Agriculture*, pp. 767–777, 1996.

[72] T.-C. Tsao and M. Tomizuka, "Adaptive and repetitive digital control algorithms for noncircular machining," in *the proceedings of American Control Conference*, 1988, pp. 115–120, atlanta, GA, USA.

[73] A. Bonchis, P. I. Corke, D. C. Rye, and Q. P. Ha, "Variable structure methods in hydraulic servo systems control," *Automatica*, vol. 37, no. 4, pp. 589–595, 2001.

[74] J. S. Brinker and K. A. Wise, "Flight testing of reconfigurable control law on the x-36 tailless aircraft," *Journal of Guidance, Control, and Dynamics*, vol. 24, no. 5, pp. 903–909, 2001.

[75] A. Alleyne and J. K. Hedrick, "Nonlinear adaptive control of active suspensions," *IEEE Transactions on Control Systems Technology*, vol. 3, no. 1, pp. 94–101, 1995.

[76] D. H. Kim and T.-C. Tsao, "A linearized electrohydraulic servovalve model for valve dynamics sensitivity analysis and control system design," *Journal of Dynamic Systems, Measurement, and Control*, vol. 122, no. 1, pp. 179–187, 2000.

[77] H. E. Merritt, *Hydraulic control systems*. New York, USA: John Wiley & Sons, 1967.

[78] M. Jelali and A. Kroll, *Hydraulic servo-systems: modelling, identification and control*. London, England: Springer, 2003.

[79] H.-H. Liao, M. J. Roelle, J.-S. Chen, S. Park, and J. C. Gerdes, "Implementation and analysis of a repetitive controller for an electro-hydraulic engine valve system," *IEEE Transactions on Control Systems Technology*, vol. 19, no. 5, pp. 1102–1113, 2011.

[80] J. Zaborszky and H. J. Harrington, "A describing function for multiple nonlinearities present in electrohydraulic control valves," *Transactions of AIEE, Part I: Communication and Electronics*, vol. 76, no. 2, pp. 183–190, 1957.

[81] H. K. Khalil, *Nonlinear systems*. Upper Saddle River, NJ: Prentice Hal, 1996.

[82] R. H. Flake, "Volterra series representation of nonlinear systems," *Transactions of AIEE, Part II: Applications and Industry*, vol. 81, no. 6, pp. 330–335, 1963.

[83] L. O. Chua and C. Ng, "Frequency-domain analysis of nonlinear systems: formulation of transfer functions," *IEE Journal on Electronic Circuits and Systems*, vol. 3, no. 6, pp. 257–269, 1979.

[84] W. J. Rugh, *Nonlinear system theory: the Volterra/Wiener approach*. Baltimore, USA: Johns Hopkins University Press, 1981.

[85] S. Boyd, L. O. Chua, and C. A. Desoer, "Analytical foundations of volterra series," *Journal of Mathematical Control and Information*, vol. 1, no. 3, pp. 243–282, 1984.

[86] S. Boyd and L. Chua, "Fading memory and the problem of approximating nonlinear operators with volterra series," *IEEE Transactions on Circuits and Systems*, vol. 32, no. 11, pp. 1150–1161, 1985.

[87] S. Billings and J. Peyton Jones, "Mapping non-linear integro-differential equations into the frequency domain," *International Journal of Control*, vol. 52, no. 4, pp. 863–879, 1990.

[88] Z. Q. Lang, S. A. Billings, R. Yue, and J. Li, "Output frequency response function of nonlinear volterra systems," *Automatica*, vol. 43, no. 5, pp. 805–816, 2007.

[89] Z. Lang, X. Jing, S. Billings, G. Tomlinson, and Z. K. Peng, "Theoretical study of the effects of nonlinear viscous damping on vibration isolation of sdof systems," *Journal of Sound and Vibration*, vol. 323, no. 1, pp. 352–365, 2009.

[90] H. Z. Tan and N. Sepehri, "Parametric fault diagnosis for electrohydraulic cylinder drive units," *IEEE Transactions on Industrial Electronics*, vol. 49, no. 1, pp. 96–106, 2002.

[91] J. Yan, B. Li, H. F. Ling, H. S. Chen, and M. J. Zhang, "Nonlinear state space modeling and system identification for electrohydraulic control," *Mathematical Problems in Engineering*, vol. 2013, no. 973903, 2013.

[92] L. Li and S. Billings, "Analysis of nonlinear oscillators using volterra series in the frequency domain," *Journal of Sound and Vibration*, vol. 330, no. 2, pp. 337–355, 2011.

[93] Z. Sun, "Electrohydraulic fully flexible valve actuation system with internal feedback," *Journal of Dynamic Systems, Measurement, and Control*, vol. 131, no. 2, p. 024502, 2009.

[94] P. Garimella and B. Yao, "Fault detection of an electro-hydraulic cylinder using adaptive robust observers," in *the proceedings of International Mechanical Engineering Congress and Exposition*, 2004, pp. 119–128, Anaheim, CA, USA.

[95] L. An and N. Sepehri, "Hydraulic actuator leakage fault detection using extended kalman filter," *International Journal of Fluid Power*, vol. 6, no. 1, pp. 41–51, 2005.

[96] P. Nakkarat and S. Kuntanapreeda, "Observer-based backstepping force control of an electrohydraulic actuator," *Control Engineering Practice*, vol. 17, no. 8, pp. 895–902, 2009.

[97] W. Kim, D. Won, and C. C. Chung, "High gain observer based nonlinear position control for electro-hydraulic servo systems," in *the proceedings of American Control Conference*, 2010, pp. 1440–1446, Baltimore, MD, USA.

[98] R. Pintelon, P. Guillaume, Y. Rolain, J. Schoukens, and H. Van Hamme, "Parametric identification of transfer functions in the frequency domain - a survey," *IEEE Transactions on Automatic Control*, vol. 39, no. 11, pp. 2245–2260, 1994.

[99] L. De Tommasi, D. Deschrijver, and T. Dhaene, "Transfer function identification from phase response data," *International Journal of Electronics and Communications*, vol. 64, no. 3, pp. 218–223, 2010.

[100] Y. Yoon, M. Yang, and Z. Sun, "Robust position tracking control of a camless engine valve actuator with time-varying reference frequency," in *the proceedings of Conference on Decision and Control*, 2014, pp. 3292–3297, Los Angeles, CA, USA.

[101] Y. Yoon and Z. Sun, "Robust motion control for tracking nonstationary signalas and its application," *IEEE Transactions on Industrial Electronics*, submitted.

[102] A. Kalafatis, N. Arifin, L. Wang, and W. Cluett, "A new approach to the identification of pH processes based on the Wiener model," *Chemical Engineering Science*, vol. 50, no. 23, pp. 3693–3701, 1995.

[103] I. Hunter and M. Korenberg, "The identification of nonlinear biological systems: Wiener and Hammerstein cascade models," *Biological Cybernetics*, vol. 55, no. 2-3, pp. 135–144, 1986.

[104] F. Xiang and J. Wikander, "Block-oriented approximate feedback linearization for control of pneumatic actuator system," *Control Engineering Practice*, vol. 12, no. 4, pp. 387–399, 2004.

[105] B. A. Francis and W. M. Wonham, "The internal model principle of control theory," *Automatica*, vol. 12, no. 5, pp. 457–465, 1976.

[106] G. Bengtsson, "Output regulation and internal models a frequency domain approach," *Automatica*, vol. 13, no. 4, pp. 333–345, 1977.

[107] M. Tomizuka, T.-C. Tsao, and K.-K. Chew, "Analysis and synthesis of discrete-time repetitive controllers," *Journal of Dynamic Systems, Measurement, and Control*, vol. 111, no. 3, pp. 353–358, 1989.

[108] A. Isidori, C. Byrnes *et al.*, "Output regulation of nonlinear systems," *IEEE Transactions on Automatic Control*, vol. 35, no. 2, pp. 131–140, 1990.

[109] Z. Sun, "Tracking or rejecting rotational-angle dependent signals using time varying repetitive control," in *the proceedings of American Control Conference*, vol. 1. IEEE, 2004, pp. 144–149.

[110] M. R. Portnoff, "Time-frequency representation of digital signals and systems based on short-time Fourier analysis," *IEEE Transactions on Acoustics, Speech and Signal Processing*, vol. 28, no. 1, pp. 55–69, 1980.

[111] T.-C. Tsao and M. Tomizuka, "Robust adaptive and repetitive digital tracking control and application to a hydraulic servo for noncircular machining," *Journal of Dynamic Systems, Measurement, and Control*, vol. 116, no. 1, pp. 24–32, 1994.